TECHNISCHE UNIVERSITÄT WIEN
Vienna | Austria

Diplomarbeit

Cation nonstoichiometry in $SrTiO_3$ based solid oxide solar cells

Ausgeführt am

Institut für Chemische Technologien und Analytik
Technische Universität Wien

unter Anleitung von

Univ.Prof. Dipl.-Phys. Dr.rer.nat. Jürgen **Fleig**
Projektass. Dipl.-Ing. Maximilian **Morgenbesser**

durch

Niklas **Bodenmüller**
Matrikelnummer: 01326325

Abstract

Despite increasing problems, fossil fuels are still the main sources of the world's growing energy demand. However, a widespread adoption of many new technologies based on alternative energy sources still requires suitable materials that combine the desired material properties. Perovskite-type oxides prove to be a promising group of materials for this purpose, being used in solid oxide fuel cells (SOFC) and being a promising candidate for solid oxide photoelectrochemical cells (SOPEC). Strontium titanate (STO) is one of the best understood perovskites and often serves as a model material for other perovskites. However, effects caused by cation nonstoichiometry in this material are still not fully understood yet. Therefore, in the course of this work the influence of the cation nonstoichiometry on the defect chemistry as well as the behavior of STO when irradiated with UV light is investigated. For this purpose, different strontium titanate samples were prepared and characterized by electrochemical impedance spectroscopy (EIS) and time-resolved voltage measurements with and without UV irradiation.

In the first part of this work, doped and nominally undoped STO polycrystals and thin films, each with variable Sr/Ti ratios, were studied via EIS. The obtained conductivities serve as an indicator for the defect state of the respective sample. Undoped and Fe-doped STO polycrystals were prepared by solid state reactions in different sintering atmospheres, affecting the Sr/Ti ratios via the partial Schottky defect reaction. After equilibration of the oxidizingly sintered pellets at 700 °C, EIS measurements in the temperature range from about 180 °C to 360 °C demonstrated the positive effect of Sr vacancies on the conductivity of the material. In contrast, for Fe-doped STO a decrease in conductivity could be measured for samples with a nominally higher amount of Sr vacancies. The possibility that this is due to Fe ions partially occupying the energetically less favorable A-site in the perovskite structure is discussed. EIS measurements on single crystals showed a clear deviation in the defect chemistry compared to the polycrystals. Thus, significantly lower conductivities, but also a stronger dependency on the Fe-doping were found. Additionally, Al-, Nb-, and Fe-doped STO thin films with different cation nonstoichiometries were prepared via pulsed laser deposition (PLD) and also analyzed via EIS. Most of them showed pseudointrinsic behavior, only the Sr-richer thin films demonstrated higher conductivities.

In the second part of the work, the influence of a cation nonstoichiometry in the substrate on the voltage of STO based high-temperature solar cells is investigated. In time-resolved voltage measurements, two types of voltages could be identified, which emerge due to different processes in the samples under UV irradiation. These voltages are a photovoltage (U_{PV}) and a battery-type voltage (U_{Batt}) due to oxygen transport, leading to oxygen stoichiometry changes. Both types of voltages showed a strong dependency on the substrate (single crystal vs. polycrystal). For the photovoltage a dependency on the cation nonstoichiometry could also be demonstrated.

Kurzfassung

Trotz zunehmender Problematik stellen fossile Brennstoffe noch immer die Hauptquellen des weltweit steigenden Energiebedarfs dar. Einer weitreichenden Verbreitung vieler neuer Technologien, die auf alternativen Energiequellen basieren, bedarf es jedoch noch geeigneter Materialien, die die jeweils gewünschten Materialeigenschaften vereinen. Oxidische Perowskite erweisen sich hierbei als eine vielversprechende Materialgruppe, die z.B. bereits in Festoxid-Brennstoffzellen (solid oxide fuel cells, SOFC) verwendet wird und deren Verwendung in Festoxid-photoelektrochemischen Zellen (solid oxide photoelectrochemical cells, SOPEC) vielversprechend ist. Strontiumtitanat (STO) stellt dabei eines der am besten verstandenen perowskitische Oxide dar und dient oft als Modellmaterial für andere Perowskite. Effekte wie Kationen-Nichtstöchiometrien sind jedoch auch bei diesem Material noch nicht zur Gänze verstanden. Im Zuge dieser Arbeit wurde daher der Einfluss der Kationen-Nichtstöchiometrie auf die Defektchemie, sowie das Verhalten von STO bei Bestrahlung mit Licht untersucht. Hierzu wurden verschiedene Strontiumtitanat-Proben hergestellt und mittels Elektrochemischer Impedanzspektroskopie (EIS) sowie zeitaufgelösten Spannungsmessungen mit und ohne UV-Bestrahlung untersucht.

Im ersten Teil dieser Arbeit wurden dotierte und nominell undotierte STO-Polykristalle und -Dünnschichten, je mit variablen Sr/Ti-Verhältnissen, mittels EIS charakterisiert. Die dabei ermittelten Leitfähigkeiten dienen als Indikator für den defektchemischen Zustand der jeweiligen Probe. Undotierte und Fe-dotierte STO-Polykristalle wurden mittels Festkörperreaktionen in verschiedenen Sinteratmosphären hergestellt, welche durch die partielle Schottky-Defektreaktion auch das Sr/Ti-Verhältnis beeinflussen. Nach einer Equilibrierung der oxidierend gesinterten Pellets bei 700 °C konnte mittels EIS-Messungen der positive Einfluss von Sr-Leerstellen auf die Leitfähigkeit des Materials im Temperaturintervall von etwa 180 °C bis 360 °C nachgewiesen werden. Bei Fe-dotiertem STO konnte im Gegenteil eine Verminderung der Leitfähigkeit bei den Proben mit nominell höheren Sr-Leerstellen-Konzentrationen ermittelt werden. Die Möglichkeit, dass dies aufgrund der teilweisen Lokalisation von Fe-Ionen auf den energetisch ungünstigeren A-Platz der Perowskitstruktur zurückzuführen ist, wird diskutiert. Bei EIS-Messungen an Einkristallen konnte ein deutlicher Unterschied in der Defektchemie verglichen zu den Polykristallen ermittelt werden. So wurden deutlich niedrigere Leitfähigkeiten, aber auch eine stärkere Abhängigkeit von der Fe-Dotierung festgestellt. Mittels “Pulsed Laser Deposition” (PLD) wurden auch Al-, Nb- und Fe-dotierte STO-Dünnschichten mit verschiedenen Kationen-Nichtstöchiometrien hergestellt. In nachfolgenden EIS-Messungen zeigten die meisten dieser Dünnschichten pseudointrinsisches Verhalten. Lediglich Sr-reichere Proben zeichneten sich durch erhöhte Leitfähigkeiten aus.

Im zweiten Teil der Arbeit wurde der Einfluss der Kationen-Nichtstöchiometrie des Substrats auf die Spannung von STO-basierten Hochtemperatursolarzellen untersucht. Bei den zeitaufgelösten Spannungsmessungen konnten zwei Arten von Spannungen identifiziert werden, die aufgrund unterschiedlicher, von der UV-Bestrahlung ausgelöster Prozesse in den Proben entstehen. Dabei handelt es sich um eine Photospannung (photovoltage, U_{PV}) und eine batterieartige Spannung (battery-type voltage, U_{Batt}) aufgrund von Sauerstofftransport und daraus resultierenden Stöchiometrieänderungen. Beide Spannungsarten zeigten eine starke Abhängigkeit von der Art des Substrats (Einkristall oder Polykristall). Für die Photospannung konnte auch eine Abhängigkeit von der Kationen-Nichtstöchiometrie gezeigt werden.

Acknowledgements

An erster Stelle gilt mein Dank Prof. Jürgen Fleig, der mir die Möglichkeit gegeben hat in seiner Forschungsgruppe an diesem interessanten Thema mitzuwirken und sich stets für meine Fragen Zeit genommen hat. Ein besonderer Dank gebührt auch meinem Betreuer Maximilian Morgenbesser, der mir durch den Verlauf der gesamten Arbeit von den ersten Probenpräparationen bis zu den finalen Diskussionen mit seiner optimistischen Art immer zur Seite gestanden ist.

Im Weiteren möchte ich mich bei der ganzen Arbeitsgruppe Elektrochemie für die angenehme Arbeitsatmosphäre, die Unterstützung bei der Durchführung von Experimenten und die lustige Zeit abseits des Labors bedanken. Speziellen Dank ergeht dabei an Alexander Viernstein für die Durchführung der *reciprocal space mappings* sowie an Harald Summerer für die *ICP-MS*-Messungen. Ich danke zudem meinen Bürokollegen Emil Ellmeyer, Gerhard Leitner und Georg Holzer, die neben den fachlichen Diskussionen mit stets interessanten Gesprächsthemen für die nötige Abwechslung sorgten.

Da nun ein Lebensabschnitt zu Ende geht, möchte ich abschließend auch meinen Freunden und meiner Familie danken. Vor allem danke ich meinen Eltern Susanne und Hubert, die mich in den Höhen wie auch in den Tiefen all dieser Jahre stets unterstützt haben. Weiters danke ich meiner Schwester Katja und ihrem Ehemann Simon, auf die ich mich immer verlassen konnte. Vielen Dank auch meinen Studienkollegen Emi, Martina, Paul, Jakob, Felix und Livia, die mich seit dem ersten Semester durch dieses Studium begleitet haben, sowie all meinen Mitbewohnern der letzten Jahre, mit denen ich abseits des Studiums einen großen Teil meiner Studentenzeit verbracht habe.

Contents

1 Introduction

Since the start of the industrial revolution, the yearly amount of consumed energy has steadily increased, reaching about 584 EJ (Exajoule) in 2019 [1]. Fossil fuels account for about 84.3 % of this energy [1], even though coal, natural gas, and petroleum are all limited resources and exhibit several disadvantages in their usage. In addition to environmental and political issues regarding their production, the combustion of fossil fuels gives rise to large amounts of carbon dioxide, often accompanied by different air pollutants. While the air pollutants are dangerous to the environment and pose a health threat for the human population, carbon dioxide acts as one of the main greenhouse-gases, and thus, contributes to the ongoing man-made climate change. For these reasons, a large share of research work worldwide is dedicated to the goal of reducing both the amount of fossil fuels consumed and the total amount of carbon dioxide in the atmosphere. While several carbon capture and storage technologies are investigated to artificially reduce the amount of carbon dioxide in the atmosphere, a more efficient use of fossil fuels and the use of alternative energy sources remain the main approaches to reduce the amount of carbon dioxide emitted.

A very promising alternative energy source is solar energy, as it does not produce any by-products with negative effects, it is sufficiently available in many parts of the world, and there is no danger of running out of it. However, since solar energy can only be used to generate energy during daytime, suitable energy storage systems are additionally required. While the already widely used solar cells convert solar energy directly to electrical energy, the direct conversion of solar energy to chemical energy seems to be an attractive alternative due to easier storage. A solid oxide photoelectrochemical cell (SOPEC) would be able to do this by using solar energy for a chemical conversion. Such a cell mostly consists of a high temperature solar cell coupled to a solid oxide electrolyzer cell (SOEC) operating at high temperatures. In this case, the solar cell provides the voltage needed for, e.g., the electrolysis of water, yielding oxygen and hydrogen as products (Figure 1.1). The latter of which can be used as fuel in a fuel cell, which converts chemical energy directly to electrical energy. One type of fuel cell is the solid oxide fuel cell (SOFC), an all-solid-state device operating at high temperatures of 500 to 1000 °C. The main advantages of a SOFC are high efficiency, fuel flexibility, low environmental pollution, and high power density [2, 3]. Despite these technologies appearing very appealing, still a lot of research has to be carried out, until they can be used in the quantities required to cause a perceivable decrease in used fossil fuels. Thus, a lot of effort is made in the search for new materials or material composites.

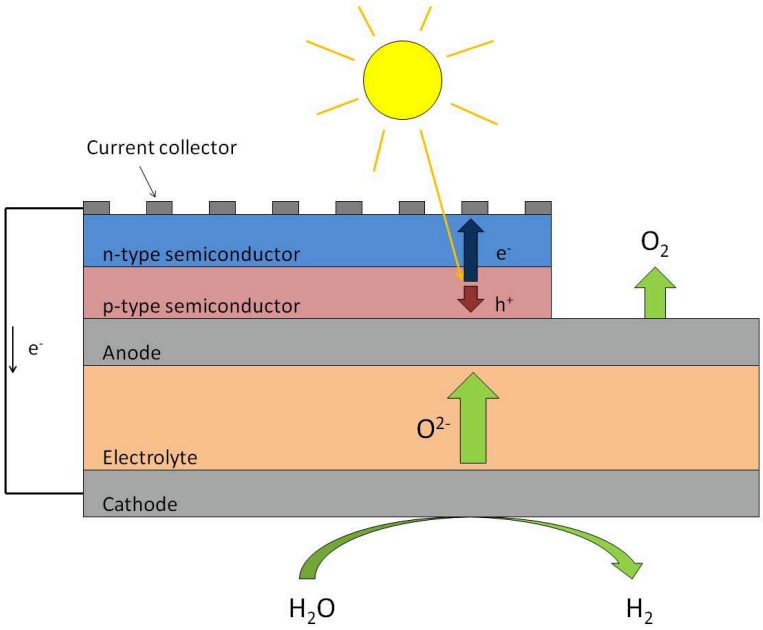

Figure 1.1: Simplified scheme of a solid oxide photoelectrochemical cell (SOPEC) electrolyzing water into oxygen and hydrogen via solar energy. The smaller top part acts as a solar cell and the broader bottom part acts as a solid oxide electrolyzer cell (SOEC)

Next to the name-giving electrolyte in SOPECs and SOFCs, solid oxide materials play an important role for many applications in future technologies. Thus, these materials are also often used as cathode, anode, and interconnect material in SOFCs [2] and are investigated for the usage as electrodes and semiconductor parts in SOPECs [4, 5]. One of the most promising group of solid oxides are the perovskites, since these materials combine interesting properties, such as ferroelectricity, high dielectricity, tailored (mixed) conductivity, and superconductivity [6, 7]. For this class of materials, strontium titanate ($SrTiO_3$, STO) often serves as a model material due to its well understood defect chemistry. New findings in STO are often transferable to other similar perovskite-type oxides such as $BaTiO_3$ and $Pb(Zr,Ti)O_3$, highlighting the relevance of this material. In addition, STO is already used as an oxygen sensor, a photoelectrode, a varistor, and a substrate for high temperature superconductors [8]. STO shows a high chemical and thermal stability and different conductive properties are accessible via the addition of dopants and individual preparation routes. Hence, the general mixed conducting STO can be tailored to serve as an isolator, a hole conductor, an ionic conductor or an electron conductor [8, 9]. Furthermore, its behavior under light illumination would be suitable for the application in SOPECs. In addition to the electron-hole generation, illumination with light at elevated temperatures can cause changes in the ionic defect composition, which is reflected by the incorporation or excorporation of oxygen in the material [10–12]. Hence, functional UV-light driven SOPECs were previously reported, in which STO acted as the light absorbing component [4, 5].

For many future applications, thin films or coatings on top of another material are desirable because of the limited space in many devices, lower weight, higher power density due to lower resistance (e.g. electrolyte in SOFCs), and material price (e.g. of noble metals) [13]. However, the preparation of thin films of solid oxide materials is often challenging. A suitable method for the preparation of such thin films is called pulsed laser deposition (PLD) [14]. While many different materials can be ablated and high quality films can be made, experience is needed to fully utilize the potential of this technique. It is, for instance, possible that the Sr/Ti ratio of a STO thin film deviates from the composition of the target [15]. Such a cation nonstoichiometry can change the defect chemical characteristics of the material, and thus, possibly its behavior when exposed to light illumination. While the effect of cation nonstoichiometries on the electrochemical properties of strontium titanate is an ongoing research topic [16–21], to the best of the authors knowledge no research on its impact on the behavior upon light illumination was published yet.

To investigate this effect, it is reasonable not to start with the more complicated case of STO thin films, but rather with a better understood system, namely polycrystalline STO. Several preparation routes for polycrystalline STO pellets are described in literature, with the simplest being solid state reactions at high sintering temperatures [18, 19, 21–23]. These sintering steps are typically conducted in an oxidizing atmosphere with only few exceptions [18]. To extend the knowledge of the STO system, sample were either prepared with sintering steps in oxidizing or reducing atmospheres. Additionally, not only pure strontium titante was investigated, but also Fe-doped STO, which is often used in literature [24–27]. For Fe-doped STO, it was previously suggested that the Fe ions could also occupy the normally unfavorable A-site of the perovskite structure [28, 29]. Still, practical results underpinning this hypothesis are yet to be published. Thus, samples with specific Sr/(Ti+Fe) ratios were prepared, for which Fe redistribution to the A-site could occur. In this regard, also doped STO thin films were prepared via PLD and electrochemically analyzed to demonstrate how specific target compositions can change the cation nonstoichimetry in the thin films.

The polycrystalline samples were analyzed with regard to their defect chemical composition as well as their behavior upon light illumination. Electrochemical impedance spectroscopy (EIS) experiments were conducted to gain further information on the conductivity, and thus, on the defect structure of the material. The behavior upon UV light illumination was investigated with time-resolved voltage measurements with and without UV light irradiation. Since material interfaces are expected to show a measurable effect for this type of experiment, different top and bottom layers were prepared and investigated. For both methods, additional experiments with single crystalline STO were conducted and compared to the polycrystalline STO specimen.

2 Theoretical Background

2.1 Defects in ionic solids

Solid matter is commonly categorized by its structural build-up into crystalline and amorphous materials. While in amorphous materials a low distance order is given, no long-range periodicity is present. Furthermore, these materials are thermodynamically metastable and possess a lower packing density than crystalline materials, leading to relatively lower densities. On the contrary, crystalline materials obtain a long-range order additionally to their short-range order. Due to their three-dimensional translation symmetry, they can be described by a unit cells and a lattice. The unit cell is the smallest repeating unit with the full point symmetry of the crystal structure. The lattice reflects the corresponding translation symmetry and is most commonly classified by the 14 Bravais lattices. When taking all possible symmetry operations into account, a crystal can structurally be classified into one of the 230 different space group types [30, 31]. However, real crystals differ from these idealized structures, since they are not infinitely big and their repeating structure is disrupted by structural imperfections, so-called defects. At temperatures above 0 K, the presence of some defects is even thermodynamically favored. This can be expressed by considering the Gibbs energy G of the crystal. According to Equation 2.1, this energy can be split into the enthalpy H and a term consisting of the entropy S and the absolute temperature T. Even though the introduction of defects causes an increase of the enthalpy by ΔH_d, the overall change in the Gibbs energy ΔG_d can be negative due to an increase of the entropy by ΔS_d (Equation 2.2). The decrease of the Gibbs energy shows a maximum at a specific defect concentration, which is further dependent on the temperature [32].

$$G = H - TS \tag{2.1}$$

$$\Delta G_d = \Delta H_d - T\Delta S_d \tag{2.2}$$

Defects have a strong impact on the properties of a material. They can, for example, change the mechanical characteristics as well as strongly alter the optical appearance or the electrochemical behavior of the material. Defects can be classified by their size into point, line, plane, and volume defects. Regarding their geometry, they are also often called 0-, 1-, 2-, and 3-dimensional defects, which is a convenient way to classify them. It is still important to note that due to the lattice distortion they generate, all these defects have practically a three-dimensional extent [33].

Point defects (0-dim):

Point defects involve only one atomic site inside the crystal. Typical examples are vacancies, atoms at interstitial sites, or doping elements (Figure 2.1). Charge and mass transport can be realized due to the mobility of these defects. Hence, they play a role of immense importance in electrochemistry and therefore are more accurately discussed in subsection 2.1.1.

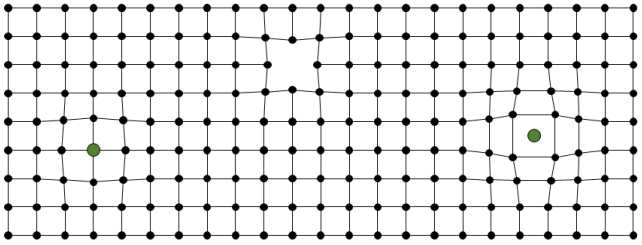

Figure 2.1: Two dimensional sketch of different point defects: Doping element, vacancy and impurity at an interstitial site

Line defects (1-dim):

Line defects are often better known as dislocations. They can be seen as a mismatch in the crystal structure occurring along a line only. The most important line defects are the edge dislocation (Figure 2.2) and the screw dislocation. The number of dislocations and their mobility have a strong effect on the mechanical properties of a material. Furthermore, the strain field created by one of those dislocation can serve as a region with enhanced chemical reactivity [33].

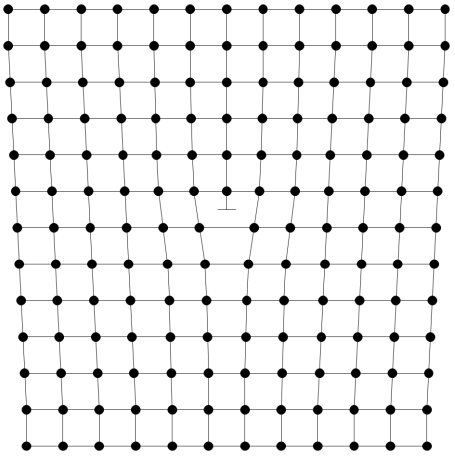

Figure 2.2: Two-dimensional sketch of an edge dislocation

Plane defects (2-dim):

Internal boundaries and surfaces can both be categorized as plane defects (Figure 2.3). While, for example, twin boundaries and anti-phase boundaries often play an important role in X-ray diffraction (XRD) experiments, grain boundaries and surfaces have a much stronger effect on the properties of the material. The surface of a crystal differs chemically strongly from the corresponding bulk phase and often shows a so-called surface reconstruction. Furthermore, different surface sites also show varying properties, like catalytic activity and reactivity [33, 34]. Grain boundaries can disturb the motion of point defects and dislocations and therefore alter the electrochemical and mechanical properties of a material strongly. Point defects like impurities and dopants can also conglomerate at the grain boundaries. Hence, deviating chemical and physical properties shall be expected at the grain boundaries. A conglomeration of charge at the core of the grain boundary leads to an oppositely charged space charge layer surrounding it. Depending on how this space charge layer is realized inside a crystal, the grain boundaries can show a higher or a lower conductivity than the bulk phase in the grains [33, 35].

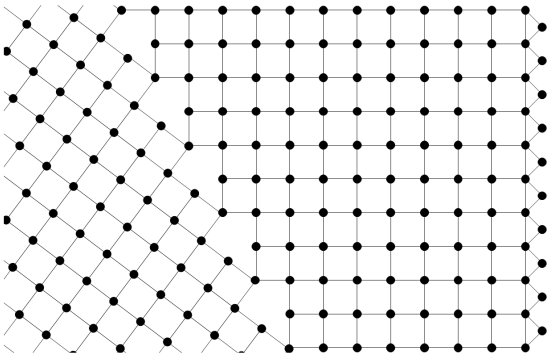

Figure 2.3: Two-dimensional sketch of a grain boundary and a reconstructed surface

Volume defects (3-dim):

Typical examples of volume defects are voids and inclusions inside the material (Figure 2.4). These defects can further be visualized as agglomerates of vacancies or impurities. Volume defects play an important role in the mechanical, electrical, and optical properties of the material. Precipitation hardening is, for instance, a commonly used hardening technique to improve the mechanical strength of aluminum alloys and others. The hardening effect derives from a disturbance in the dislocation movement caused by the inclusions [33].

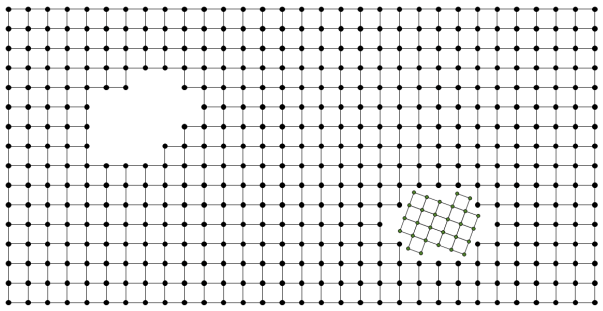

Figure 2.4: Two-dimensional sketch of a void and an inclusion of another crystal

2.1.1 Point defects

Due to the big impact point defects have on the electrochemical materials, their understanding is crucial for the understanding of solid state electrochemistry. In the following a short introduction to intrinsic point defects, extrinsic point defects, and oxygen non-stoichiometry shall be given. For the depiction of zero-dimensional defects in chemical equations the Kröger-Vink notation proved to be a useful and readily understandable notation system. Its overall principle is depicted in Equation 2.3. The notation of a defect consist of a main symbol, a subscript and a superscript. The main symbol describes the considered species. For an atom or an ion the associated element symbol is depicted, while an "e" indicates an electron, an "h" a hole and a "V" a vacancy. The subscript adds the information of the site the defect is located. This can either be the element symbol of the ion, which naturally sits on that site or an "i", if the defect is located on an interstitial site. Lastly, the superscript corresponds to the charge the defect species holds relatively to the charge of the normal occupant of this site. A negative relative charge is denoted by a "/", a neutral relative charge by a "x" and a positive relative charge by a "$\bullet$" [32].

$$\mathrm{M}_{\mathrm{S}}^{\mathrm{C}} \tag{2.3}$$

Intrinsic defects

Since a presence of intrinsic defects is thermodynamically favored (section 2.1), they even occur in perfectly stoichiometric crystals. The emergence of intrinsic defects gets increased via thermal activation, making their concentration heavily dependent on the temperature [35]. A very common intrinsic disorder is the electron-hole generation (Equation 2.4), which plays a major role in the conductivity of semiconductors [36]. The most important ionic intrinsic defects are the Schottky disorder and the Frenkel disorder. A Frenkel disorder can be visualized by a cation, which switches from its normal site to a normally unoccupied site (Equation 2.5), creating a cation vacancy and a cation at an interstitial site [35]. Furthermore, there is also a so-called Anti Frenkel disorder (Equation 2.6), which consists of an anion vacancy and an anion at an interstitial

site. Due to the fact that occupying interstitial sites is energetically very unfavorable for the large anions, the Anti Frenkel disorder is rather rarely occurring and is mostly present in crystals with fluorite structures [36]. In contrast, a Schottky disorder consists of an anion vacancy and a cation vacancy. According to Equation 2.7, the Schottky disorder gets often visualized by two ions relocating to the surface and leaving two vacancies at their former sites behind [35]. Schottky disorder often appear in crystals with too dense crystal structures for the formation of interstitial defects [8]. Additionally, also a so-called partial Schottky disorder is possible in complex oxides (see subsection 2.2.1).

$$\text{nil} \rightleftharpoons \text{e}' + \text{h}^{\bullet} \tag{2.4}$$

$$\text{M}_{\text{M}}^{\times} \rightleftharpoons \text{V}_{\text{M}}'' + \text{M}_{\text{i}}^{\bullet\bullet} \tag{2.5}$$

$$\text{O}_{\text{O}}^{\times} \rightleftharpoons \text{V}_{\text{O}}^{\bullet\bullet} + \text{O}_{\text{i}}'' \tag{2.6}$$

$$\text{M}_{\text{M}}^{\times} + \text{O}_{\text{O}}^{\times} \rightleftharpoons \text{V}_{\text{M}}'' + \text{V}_{\text{O}}^{\bullet\bullet} + \text{M}_{\text{M,surf}}^{\times} + \text{O}_{\text{O,surf}}^{\times} \tag{2.7}$$

Extrinsic defects

Extrinsic defects can either result from doping or impurities. While impurities are normally undesired, dopants are often specifically introduced to alter the electrochemical properties of a material. Hence, it is often possible to completely neglect the intrinsic defects in doped materials [24, 35]. Doping can introduce a lot of different effects, but it is still possible to divide dopants into two classes, donor dopants and acceptor dopants.

In an ionic material donor doping can be achieved by introducing cations with a positive relative charge at the site they inhabit in the material. Due to the fact that charge neutrality has to be preserved, additional defects with negative relative charge have to be present in the material. These can either be electrons, cation vacancies, or anions at interstitial sites. In contrast, acceptor doping is achieved by introducing cations with a negative relative charge at the site they inhabit in the material. The preservation of charge neutrality leads to defects with positive relative charges. These can either be holes, anion vacancies, or cation at interstitial sites [37].

For instance, yttria stabilized zirconia (YSZ) is a widely used electroceramic and serves as a good example for the impact of extrinsic defects. The doping of ZrO_2 with Y_2O_3 shows two distinguishable effects. First, it preserve the cubic modification of the zirconia crystal structure. Additionally to this, the yttria doping serves as an acceptor dopant. The introduction of Y_{Zr}' leads to the formation of $V_O^{\bullet\bullet}$, since neither holes nor interstitial defects are energetically favorable. The abundance of oxygen vacancies leads to an ionic conductivity at elevated temperatures, which is used in many technical applications, like oxygen sensors and electrolytes of solid oxide fuel cells [36, 37].

Oxygen nonstoichiometry

Additionally to the intrinsic and extrinsic defects discussed above, it is always possible for an ionic solid to exhibit deviations from their stoichiometric composition. The most important of these deviations is the oxygen nonstoichiometry, which comes into existence due to a chemical equilibrium of the oxide anions in the material with the oxygen in the surrounding air. At elevated temperatures, either an oxygen incorporation or an oxygen release can occur depending on the oxygen partial pressure. Since the amount of time necessary to reach the equilibrium increases drastically at lower temperatures, the oxygen concentration of a material often remains frozen in, not reaching equilibrium with is surrounding. In Equation 2.8 an example for an oxygen release reaction is depicted. Due to the formation of electrons, the oxygen nonstiochiometry reaction has also a substantial impact on the concentration of electronic defects in the system. Thus, it plays an important role for the conductive properties of a material. The dependency of the concentrations of different defect species on the oxygen partial pressure can be illustrated with the Brouwer diagram (Figure 2.5). Here, the logarithm of the defect concentrations, which are - within a certain scope - proportional to the conductivity, are plotted against the logarithm of the oxygen partial pressure [35].

$$\mathrm{O_O^{\times}} \rightleftharpoons \mathrm{V_O^{\bullet\bullet}} + 2\,\mathrm{e'} + \frac{1}{2}\,\mathrm{O_2} \tag{2.8}$$

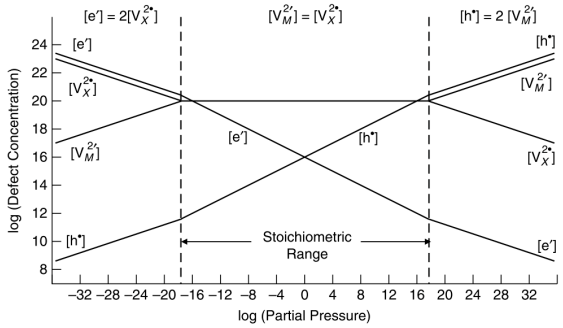

Figure 2.5: Simplified Brouwer diagram for an undoped material with a higher stability of ionic defects than electronic defects [38]

2.1.2 Conductivity

When a thermodynamic equilibrium is present, the electrochemical potential $\tilde{\mu}_i$ of a species i is constant over the whole system. According to Equation 2.9, this electrochemical potential can be split into the chemical potential μ_i of the species and a term dependent on the electrical potential ϕ. Here, z_i depicts the charge number of the species and e_0 the elementary charge. By disrupting this equilibrium state a particle flux emerges, which opposes the gradient of the electrochemical potential. The particle flux density J_i can be expressed by Equation 2.10, with σ_i being the specific conductivity of the species i [35, 39].

$$\tilde{\mu}_i = \mu_i + z_i e_0 \phi \tag{2.9}$$

$$J_i = -\frac{\sigma_i}{z_i^2 e_0^2} \nabla \tilde{\mu}_i \tag{2.10}$$

In general, electrical conductivity in a materials can either be realized by the motion of electronic charge carriers (e' or $h^{\bullet}$) or ionic charge carriers ($V_O^{\bullet\bullet}$ or $OH_O^{\bullet}$). While in many materials one of both mechanism is predominant, some electroceramic materials can also be described as mixed ionic-electronic conductors (MIEC) [40]. By applying an external electrical potential at a material, the equilibrium state of the electrochemical potential gets disrupted for each charge carrier species inside the material. Therefore, a particle flux emerges for each mobile charge carrier relative to the respective conductivity. Hence, the overall electrical conductivity σ_{tot} can be expressed as the sum of the conductivities of each possible charge carrier (Equation 2.11). The conductivity of a single charge carrier species σ_i can be calculated from the charge number z_i, the mobility u_i and the concentration c_i of this charge carrier. This relation is depicted in Equation 2.12, with F being the Faraday constant [35, 39, 41].

$$\sigma_{tot} = \sigma_e + \sigma_h + \sum \sigma_{ion} \tag{2.11}$$

$$\sigma_i = z_i * F * u_i * c_i \tag{2.12}$$

The movement of an ionic charge carrier in a solid can be described through a hopping process. Here, the ion jumps from its current site to a neighboring unoccupied site, whereas an activation energy is needed. Thus, the mobility in Equation 2.12 can be expressed with the Nernst-Einstein-equation given in Equation 2.13. Here, k_B is the Boltzmann constant and D is the diffusion coefficient, which can be further split into a pre-exponential factor D_0 and an exponential term, with E_a being the activation energy necessary for a single hop. This expression can be simplified by summing up all constant pre-exponential factors in one term u_0. Further on, it is also possible to express the electrical conductivity via ionic charge carriers in a similar manner (Equation 2.14). It is important to add that in the case of ionic charge carriers, only the concentration of extrinsic defects can be assumed to be temperature independent. The concentration of either intrinsic defects or oxygen nonstoichiometry are regulated via chemical equilibria, which themselves change with varying temperatures. Therefore, the activation energy E_a gets replaced by an activation energy E_a', which is affected by a mixture of mobility and concentration effects, but still holds valuable information about the conducting mechanism in a material [39, 41].

$$u_i = \frac{z_i e_0}{k_B T} D = \frac{z_i e_0}{k_B T} D_0 * e^{-E_a/k_B T} = \frac{u_0}{T} e^{-E_a/k_B T} \tag{2.13}$$

$$\sigma = \frac{\sigma_0}{T} * e^{-E_a'/k_B T} \tag{2.14}$$

Unlike metallic materials, the conductivity of electronic charge carriers inside an ionic material is often not sufficiently described by a band-like conductivity. Due to self-trapping effects inside the material the charge carriers might occupy a more localized form [42]. Therefore, the electronic conductivity of ionic materials is often either described by a band-like conductivity or a so called polaron conductivity. A polaron is a composite quasi-particle, which can be seen as an electron or hole localized at a specific site causing a polarization and further on a lattice distortion in the surrounding crystal. Depending on the size of this distortion, they are often divided into large (Fröhlich) polarons and small (Holstein) polarons. Small polarons have a radius in the order of magnitude of the lattice constant, while large polarons show a much larger extend [36, 43].

For a band-like conductivity, the mobility of the electronic charge carriers decreases at rising temperatures due to an increase of lattice vibrations, which interfere with the movement of the delocalized electrons or holes. The temperature dependency of acoustic phonon scattering can often be used to represent the temperature dependency of the mobility of these charge carriers (Equation 2.15). In case of a large polaron the effective mass of the quasi particle increases only slightly compared to a free electron, leading to only a relative small decrease of their mobility. Hence, the band-like conductivity often resembles a good approximation for the mobility of a large polaron [39]. On the contrary, the mobility of the far more localized small polarons are better depicted by a hopping process similar to the mobility of an ionic charge carrier. Therefore, Equation 2.13 can also be used to describe the mobility of a small polaron [39, 42, 43]. Since the concentration of these charge carriers is also dependent on the temperature, it is often not straightforward to tell, which conductivity mechanism describes a material the best. Furthermore, it is also possible for small and large polarons to coexist inside a material [42].

$$u \sim T^{-3/2} \tag{2.15}$$

To resolve the predominant conducting mechanism in a material, the activation energy is often used. The activation energy itself can be obtained by plotting conductivity values measured at different temperatures in a so-called Arrhenius plot. Here, the logarithm of the conductivity times the absolute temperature is plotted against the inverse total temperature. When no change in conductivity mechanism appears the conductivities of a material measured at different temperatures should show a linear relationship in this diagram, according to Equation 2.16. Therefore, the activation energy E'_a can be estimated from the slope of the plot [41]. Due to the exponential temperature dependency the 1/T term in Equation 2.14 gets often neglected, leading to an Arrhenius diagram of $log(\sigma)$ versus $1/T$. This diagram and the resulting activation energy are widely used in literature, since both axis plot values with a physical meaning and comparisons can still be made [44–47].

$$log(\sigma T) = log(\sigma_0) - \frac{E'_a}{2.3 * k_B} * \frac{1}{T} \tag{2.16}$$

2.2 Strontium titanate (STO)

Strontium titanate (STO) is a ceramic material with the chemical formula $SrTiO_3$. Above 105 K it exhibits a cubic perovskite crystal structure [8], which is shown in Figure 2.6. In this centrosymmetric structure the larger Sr ions sit in the corners of the cube (orange) and the smaller Ti ions are located in the center of the body (blue). The oxygen ions (light blue) are placed in the center of the cube walls giving the Ti ions a 6-fold and the Sr ions a 12-fold coordination.

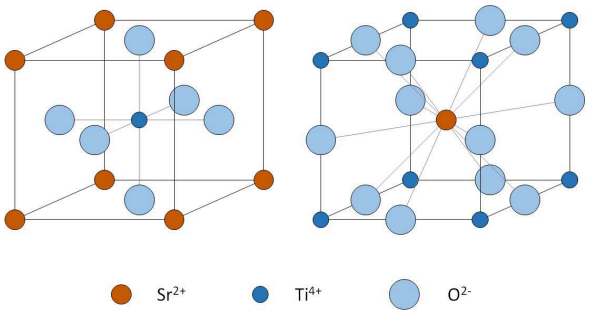

Figure 2.6: Structure of STO depicted with the Ti-site (left) and the Sr-site (right) in the center of the unit cell

Below 105 K the structure of STO changes into a tetragonal modification by a so-called antiferrodistortive phase transition [48]. This phase transition can be imagined by a rotation of the TiO^{6-} octahedrals around the c-axis [49–51]. The tilt angle reaches only about 2 ° and since the rotation alternates along the c-axis [49, 50], the material remains paraelectric in the tetragonal modification like it was in the cubic phase [52, 53]. While STO approaches a ferroelectric state at about 40 K, the paraelectric phase remains stable to at least 0.035 K due to quantum-mechanical stabilization, making it a so-called quantum paraelectric [54, 55]. However, the appearance of ferroelectricity via an external field [53], stress[56], oxygen-isotope exchange [57], and calcium substitution [58] has been reported. At room temperature, STO has a high relative permittivity in the range of 300 [24, 59], which proves to be relatively independent of the frequency of measurement as well as the applied field strength [60]. Furthermore, the dielectric behavior fits the Curie-Weiss law at higher temperatures, while in the range of about 50 K significant deviations arise [61]. Hence, with further cooling the dielectric constant, perpendicular to the c-axis, increases to about 30 000 at 3 K, after which it remains temperature independent due to quantum fluctuations in the quantum paraelectric state [58]. Additionally, at low temperatures a giant piezoelectricity [62], a light-induced persistent magnetism [63], superconductivity [64], and a green luminescence induced via photoluminescence or cathodic luminescence [65, 66] were reported. At higher temperatures, this luminescence peak in the green regime (2.4 - 2.5 eV) disappears and gets replaced by a broad peak in the blue regime (2.8 - 2.9 eV) [65, 66]. Nonetheless, undoped STO itself is a transparent, sometimes slightly yellowish semiconductor. It has a large bandgap of 3.25 eV at room temperature [65] and a high refractive index in the range of 2.4 [24].

2.2.1 Defect chemistry of STO

Like all materials, strontium titante exhibits intrinsic defects at finite temperatures. Nonetheless, the presence of ions at interstitial sites can be excluded in STO due to its close-packed perovskite structure. Hence, the partial Schottky reaction, shown in Equation 2.17, marks the fundamental intrinsic disorder reaction [8]. The SrO transitions in a second phase, which happens, for example, at the surface or the grain boundaries. In literature, so-called Ruddlesden-Popper phases could be detected to function as sinks and sources for strontium ions and vacancies [21, 67–70]. These phases can be seen as shear structures of the $SrTiO_3$ structure [71]. The partial Schottky reaction plays an important role above 1200 °C, while at lower temperatures no sufficient Sr ion mobility is given. Therefore, the thermal history of STO should always be a factor to be considered, since the Sr vacancies concentration often resembles a frozen-in state formed during sample preparation [8]. Furthermore, also deviations in the Sr/Ti ratio from the sample preparation can prevail in the material. According to Liu et al., possible defects for such a cation nonstoichiometry can be Sr vacancies V''_{Sr}, oxygen vacancies $V^{\bullet\bullet}_{O}$, but also Ti antisite defects $Ti^{\bullet\bullet}_{Sr}$ in the case of Sr-deficient materials [72]. For Ti-deficient materials, on the other hand, the expected defects are Ti vacancies V''''_{Ti}, oxygen vacancies $V^{\bullet\bullet}_{O}$, and Sr antisite defects Sr''_{Ti} [72, 73]. Due to their immobility at lower temperatures, these defects can often be seen as native dopants, altering the material properties. Since it is often rather challenging to estimate the impact of the cation nonstoichiometry, STO often gets doped to be able to neglect its effect [8, 24]. Nonetheless, a lot of research aims for a better understanding of the effect deviations in the Sr/Ti ratio have on the properties of the material [15–23, 70, 73–76].

$$Sr^{\times}_{Sr} + O^{\times}_{O} \rightleftharpoons V''_{Sr} + V^{\bullet\bullet}_{O} + SrO \tag{2.17}$$

At lower temperatures, it has to be taken into account that an agglomeration of defects can occur. For instance, a possible trapping of electrons at oxygen vacancies (Equation 2.18) and holes at strontium vacancies (Equation 2.19) could appear [67, 77–79]. Janotti et al. calculated that an oxygen vacancy can also form a single charged agglomerate with a small polaron. Thus, even the aforementioned blue luminescence can be explained due to the recombination of the electron incorporated in this agglomerate and a conduction band hole. Meanwhile, the green luminescence at very low temperature is explained by the recombination of a free electron with a self-trapped hole (i.e. a small hole polaron), since they found that a self-trapped hole is just slightly lower in energy than a free hole and therefore most-likely only exists at very low temperatures [65]. Lastly, a clustering of oxygen vacancies into a linear defect complex has been reported in STO, which decreases the overall free charge carrier content as well as the oxygen vacancy mobility [80–82].

$$V^{\bullet\bullet}_{O} + 2\,e' \rightleftharpoons V^{\bullet}_{O} + e' \rightleftharpoons V^{\times}_{O} \tag{2.18}$$

$$V''_{Sr} + 2\,h^{\bullet} \rightleftharpoons V'_{Sr} + h^{\bullet} \rightleftharpoons V^{\times}_{Sr} \tag{2.19}$$

Like discussed in section 2.1.1, oxygen nonstoichiometry reactions play an important role in complex oxides. Hence, the oxygen release and oxygen incorporation reactions and their dependency on the surrounding oxygen partial pressure and temperature are a key factor for the understanding of the defect chemistry of STO. Depending on the oxygen partial pressure regime as well as on the doping content in the material, this equilibrium reaction can occur in STO through the consumption of electrons (Equation 2.20) or the creation of holes in the material (Equation 2.21) [8, 9, 24, 25, 28, 67, 78]. In general, three different oxygen partial pressure regimes can be distinguished for STO [8, 24, 83]. At very low oxygen partial pressures, a significant oxygen depletion can be implemented, which further on leads to the creation of additional electrons in the material. Hence, STO treated in reducing atmosphere shows a n-type conductivity and can even obtain a black color due to the large number of electrons in the conduction band [24]. At higher oxygen partial pressures, a conductivity minimum with predominant ionic conductivity is reached, realized by the mobile oxygen vacancies. When the oxygen partial pressures gets increased further, oxygen vacancies compensating, for instance, Sr vacancies get filled up, while increasing the number of holes in the valence band, leading to a p-type conductivity [8, 24, 83]. Furthermore, it is important to note that the oxygen exchange reaction starts to freeze in at temperatures below about 400 °C [26, 84].

$$\frac{1}{2}\,O_2 + V_O^{\bullet\bullet} + 2\,e' \rightleftharpoons O_O^{\times} \tag{2.20}$$

$$\frac{1}{2}\,O_2 + V_O^{\bullet\bullet} \rightleftharpoons O_O^{\times} + 2\,h^{\bullet} \tag{2.21}$$

Due to frozen-in cation vacancies and small amounts of, for instance, Al, Fe, or Mn impurities acting as acceptor dopants, nominally undoped STO shows mostly a p-type conductivity behavior [9, 29]. For the introduction of a n-type conductivity, donor dopants can be added, which are typically M^{3+} ions on Sr sites and M^{5+} on Ti sites. Through the addition of donor dopants either strontium vacancies V_{Sr}'' or additional electrons e' have to serve as charge compensation inside the material [8]. Hence, through the addition of, for instance, La^{3+} or Nb^{5+} ions, even at room temperature relative high electrical conductivities can be reached in STO [85, 86]. In contrast, typical acceptor dopants are mostly M^{3+} (or M^{2+}) ions on Ti sites, which results in additional $V_O^{\bullet\bullet}$ and $h^{\bullet}$ [8]. Fe^{3+} is, for instance, an often used acceptor dopant, which increases the total number of positive charged defects and therefore increases the conductivity via the introduction of additional holes in the valence band. However, since iron is a multivalent dopant, additional trapping events have to be considered (Equation 2.22) [87]. The ratio between Fe^{3+} (Fe_{Ti}') and Fe^{4+} ($Fe_{Ti}^{\times}$) ions is dependent on the temperature, the total iron concentration, and the oxygen partial pressure of the surrounding atmosphere [24].

$$Fe_{Ti}' + h^{\bullet} \rightleftharpoons Fe_{Ti}^{\times} \tag{2.22}$$

Since M^{3+} ions can function as donors on the A-site as well as acceptors on the B-site, an amphoteric behavior is possible for ions with radii intermediate of the typical radii of the A and B-sites. Hence, rare-earth ions often occupy both sites, self-compensating their charge and lowering the total number of oxygen vacancies. However, tuning the site distribution of these ions is still challenging [28, 29, 88]. Akhtar et al. calculated that also Fe^{3+} and Mn^{3+} would show such an amphoteric behavior in STO [28]. While Mn^{4+} ions normally occupy the Ti-site, Maier et al. found that Mn^{2+} ions can be forced to both sites. A reducing annealing of, with Mn^{4+} ions doped, Sr-rich STO results in Mn^{2+} ions on the B-site and an oxidizing sintering of Sr-depleted Mn-doped STO results in Mn^{2+} ions occupying Sr sites [29]. While Maier et al. also suggested a similar behavior of Fe ions [29], to the best of the authors knowledge, experimental studies with amphoteric behavior of Fe ions have not been reported so far. Lastly, also for doped STO an agglomeration of defects at lower temperatures has to be expected. Hence, in the case of Fe-doped STO, Fe'_{Ti}–$V_O^{\bullet\bullet}$ first nearest neighbor complexes can form at temperatures below about 300 °C. Such defect complexes can significantly reduce the conductive properties of the material as well as alter the coloration [8, 89, 90].

2.2.2 Behavior upon UV light illumination

While the defect chemistry of STO is already quite well understood, the interaction of light illumination with the material is a rather new topic, with most research published being about the aforementioned luminescence behavior of STO [65, 66]. Still, in the last couple of years an increasing interest arose on the effect light irradiation has on the material stoichiometry at elevated temperatures. Merkle et al. found that the illumination with UV light induces an increased oxygen incorporation into Fe-doped STO [10]. This is due to an increase of electrons and holes via the light induced electron-hole generation reaction (Equation 2.23). In the hole conducting material, this reaction has relatively seen a much bigger influence on the smaller electron concentration than the bigger hole concentration. Hence, a participation of electrons in the rate limiting step of the oxygen incorporation reaction or in one or more of the elementary steps before the rate limiting step was concluded, with holes being the only electronic species, which might participate in the steps following the rate limiting steps [10].

$$\mathrm{nil} + h\vartheta \rightleftharpoons e' + h^{\bullet} \tag{2.23}$$

Viernstein et al. found that such an UV enhanced oxygen incorporation leads to a reversible blackening of Fe-doped STO single crystals [25]. The dark color emerges from Fe^{4+} due to an increased hole trapping (Equation 2.22) induced by the change in oxygen stoichiometry. Furthermore, the color change is accompanied by an increase in the electrical conductivity of the material. Via a heat treatment, these changes in the material properties could be countermand [25]. In contrast to these results, Hensling et al. found an increased oxygen release reaction occurring in STO substrates during PLD depositions due to the UV radiation of the plasma plume [11].

Horikiri et al. created a high temperature Schottky solar cell with a Nb-doped STO / indium tin oxide heterojunction. The characteristics of this solar cells depended strongly on the oxygen partial pressure, with the highest open-circuit voltage of 123 mV measured at 1 bar and 873 K [12]. In contrast, Brunauer et al. used a $La_{0.8}Sr_{0.2}CrO_3$ / STO junction as a photovoltaic cell and generated up to 920 mV open-circuit voltage via the illumination of UV light at 400 °C. Further on, this photovoltaic cell was connected to an electrochemical cell, forming a functional SOPEC, which could pump oxygen from low oxygen partial pressures to high oxygen partial pressures [4].

Walch et al. used STO as an electrode in a photoelectrochemical cell with YSZ as electrolyte [5]. Via UV irradiation this cell could be charged, during which two different voltages could be detected. The first voltage was a photovoltage U_{PV} emerging at the STO / current collector interface, since this interface can work as a Schottky solar cell (Figure 2.7). At this interface a Schottky contact is present, which results in an electric field as well as an electrostatic potential step. Light illumination leads to the emergence of conduction band (CB) electrons and valence band (VB) holes. Due to the present electric field one of these photo-generated charge carrier species diffuses across the material interface. Hence, a voltage between the current collector and the counter electrode emerges. This voltage appears immediately when turning the UV light on, with a negative potential being expected at the metal, due to the slight p-type conductivity of nominal undoped STO. When short-circuiting the cell, the photovoltage would lead to an oxygen pumping from the counter electrode to the STO electrode.

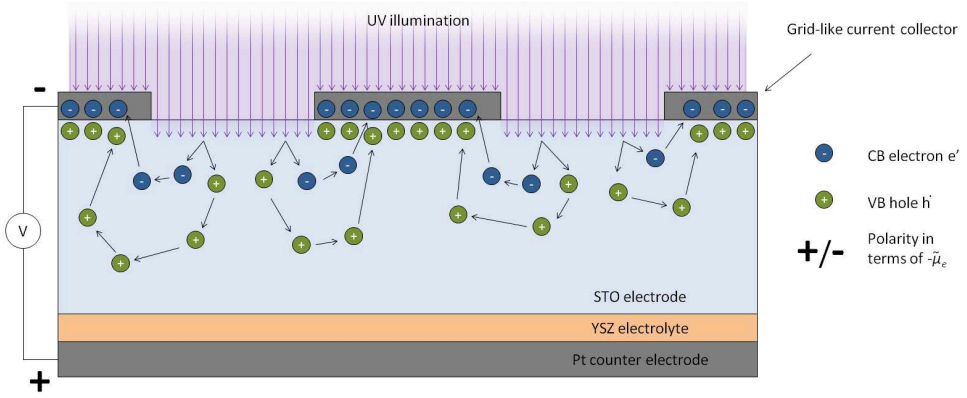

Figure 2.7: A simplified scheme of the process leading to the build-up of the photovoltage

The second voltage detected by Walch et al. is a slowly emerging voltage, which was assigned as battery voltage U_{Batt}. This voltage was traced back to an enhanced oxygen incorporation due to the UV irradiation (Figure 2.8). Since this incorporation leads to the formation of valence band holes, a positive potential in the STO electrode relative to the counter electrode emerges. When short-circuiting the cell, the battery voltage would lead to an oxygen pumping from the STO electrode to the counter electrode. It is important to note that a change in the oxygen vacancy concentration as well as a chemical potential difference of oxygen between bulk material and interface also alters the previously discussed photovoltage [5].

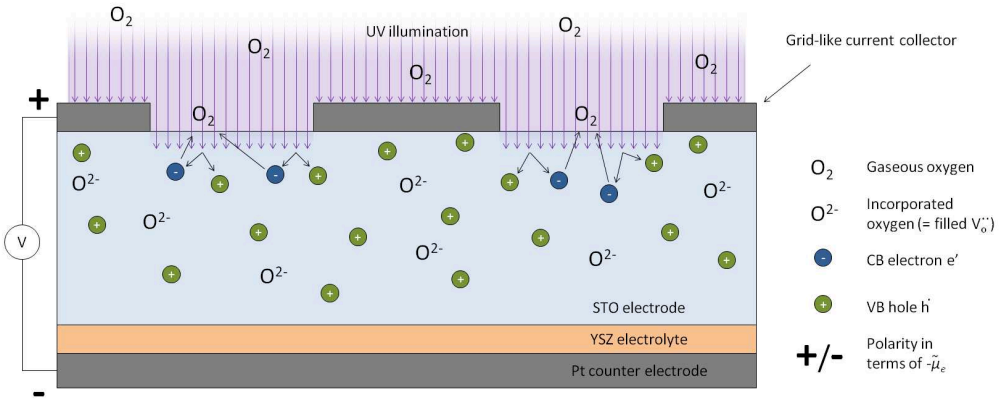

Figure 2.8: A simplified scheme of the process leading to the build-up of the battery voltage

In Figure 2.9 a model by Walch et al. is depicted, which visualizes how the photovoltage, battery voltage and total voltage change over time [5]. Before illumination, for still unknown reasons a comparably constant cell voltage is present, which is called dark voltage U_{Dark}. Turning on the UV light immediately generates a photovoltage, leading to a peak in the total voltage but also to the slower emergence of the battery voltage. During irradiation the total voltage possesses a curved course directed by the build up of the battery voltage and the change of the photovoltage due to the change in the material. When turning the UV light off, the photovoltage disappears and only the battery voltage after this certain amount of time remains. Without UV irradiation the material slowly equilibrates with its surrounding, releasing the previously incorporated oxygen, which results in the total voltage approaching the dark voltage [5]. Since the first measured total voltage upon irradiation is only determined by the photovoltage, which afterwards rather declines, Walch et al. denoted this value as $U_{PV,Max}$. On the contrary, the first total voltage after turning the UV light off is only determined by the battery voltage, which increased up to this point. Hence, this value can be assigned as $U_{Batt,Max}$.

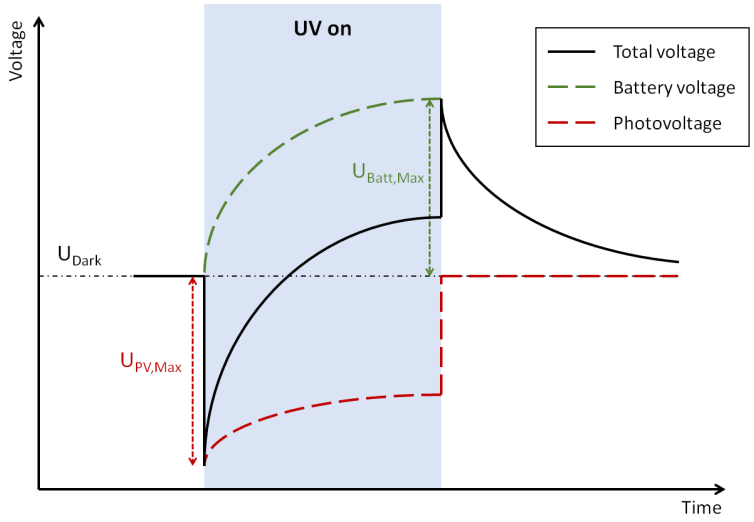

Figure 2.9: Total voltage, battery voltage, and photovoltage curves upon UV light illumination

2.3 Lanthanum chromite (LCr)

Since undoped lanthanum chromite ($LaCrO_3$, LCr) as well as Sr-doped lanthanum chromite ($La_{1-x}Cr_xO_3$, LSCr) were used during this thesis, a short overview over their material properties shall be given. In contrast to STO, LCr possess an orthorhombic derivative of the perovskite structure [91, 92] and features mainly an electronic conductivity due to its low vacancy concentration, at least in air [93]. The p-type electronic conductivity is most prominent in oxidizing conditions and decreases with decreasing oxygen partial pressure. This can be explained through the consumption of electron holes while excorporating oxygen via Equation 2.24 [94].

$$O_O^{\times} + 2\,Cr_{Cr}^{\bullet} \rightleftharpoons \frac{1}{2}\,O_2 + V_O^{\bullet\bullet} + 2\,Cr_{Cr}^{\times} \tag{2.24}$$

Even though donor doping was previously reported within the lanthanum chromite system [91], acceptor doping is more commonly investigated [93, 94]. The acceptor doping increases p-type conductivity via a small polaron mechanism [94]. Therefore, big alkaline-earth elements like Sr and Ca are often used as dopings, which are located on La sites and add electron holes $h^{\bullet}$ to the system [94]. The Ca doping increases the conductivity stronger relatively to Sr-doping, because Ca^{2+} (0.134 nm) has a radius closer to the La^{3+} radius (0.136 nm) than the Sr^{2+} radius (0.144 nm) [94]. This leads to less lattice distortion, which enlarges the mobility of a given defect. An additionally hole trapping effect has to be considered, when doping with metals like Cu or Co, which can posses different oxidation states [94].

2.4 Electrochemical Impedance Spectroscopy (EIS)

Electrochemical impedance spectroscopy (EIS) is a powerful technique for the characterization of electrical and electrochemical systems. In addition to its broad applicability, EIS convinces due to the fact that it is a nondestructive technique which only requires a relatively simple experimental setup. However, the correct interpretation to obtain meaningful physical parameters is often challenging.

2.4.1 Working principle

Ohm's law is a well known equation to calculate the resistance R from an ideal resistor via the voltage U and the current I (Equation 2.25). It describes the motion of free charge carriers in a material. However, in real materials also charge displacement phenomenons appear, leading to a displacement current and further on to a capacitive reactance. Thus, Ohm's law is not sufficient to express the conductivity of real materials. Therefore, the resistance gets replaced by the impedance Z, which is the frequency dependent AC resistance of an electrical system. When an alternating voltage U_t is applied, it can be expressed as a complex number according to Equation 2.26, with U_0 being the amplitude of the voltage, t being the time and ω being the angular frequency. For small voltages the resulting current can be described with Equation 2.27, with I_0 being the amplitude of the current and φ being the phase shift. It is important to note that I_0 and φ are still functions of the angular frequency. The AC frequency itself is connected via Equation 2.28 with the angular frequency.

$$R = \frac{U}{I} \tag{2.25}$$

$$U(t) = U_0 * e^{i\omega t} \tag{2.26}$$

$$I(t) = I_0 * e^{i(\omega t - \varphi)} \tag{2.27}$$

$$f = \frac{\omega}{2\pi} \tag{2.28}$$

Hence, the impedance $Z(\omega)$ can be expressed by Equation 2.29, with Z_0 being the ratio of the amplitude of the voltage and the amplitude of the current. In Equation 2.30 the Euler formula is depicted, which shows the relationship between the trigonometric functions and the complex exponential function. Thus, it is possible to depict the impedance as an expression consisting of a real part and an imaginary part (Equation 2.31).

$$Z(\omega) = \frac{U(t)}{I(t)} = \frac{U_0 * e^{i\omega t}}{I_0 * e^{i(\omega t - \varphi)}} = Z_0 * e^{i\varphi} \tag{2.29}$$

$$e^{i\varphi} = cos(\varphi) + isin(\varphi) \tag{2.30}$$

$$Z(\omega) = Z_0 * e^{i\varphi} = Z_0(cos(\varphi) + isin(\varphi)) \tag{2.31}$$

Equation 2.31 can be simplified for different idealized circuit elements with constant phase shifts. The equations for the impedance of three commonly used circuit elements are depicted in Equation 2.32 to Equation 2.34. The current flowing through an ideal resistor has no phase shift related to the voltage. Therefore, the impedance Z_R of a resistor has further no imaginary part and is equal to the frequency independent resistance R. In electrochemistry an ionic or electronic charge transport or a charge transfer across an interface can be described with this circuit element. In contrast, the impedance Z_L of an ideal inductor has a 90 ° phase shift and can be described solely with an imaginary part. It increases with increasing frequency and increasing inductance L. The current through a capacitor has a phase shift of −90 ° in regards to the voltage. Therefore, the impedance Z_C of capacitor can also be described only with an imaginary part, while it decreases with increasing frequency and increasing capacitance C. In electrochemistry dielectric materials, double layer structures, and chemical capacitances are often described by capacitors.

$$Z_R(\omega) = R \tag{2.32}$$

$$Z_L(\omega) = i * \omega * L \tag{2.33}$$

$$Z_C(\omega) = \frac{1}{i * \omega * C} \tag{2.34}$$

When two circuit elements are connected in series, the overall impedance of them Z_{1-2} can be calculated with Equation 2.35. In contrast, when the individual circuit elements are parallel combined Equation 2.36 describes their overall impedance $Z_{1||2}$. Real materials exhibit ohmic resistances and capacitive reactances. Therefore, the simplest way to describe them is a RC element, which consists of a resistance and a capacitor connected in parallel. The formula for the impedance Z_{RC} of a RC element is shown in Equation 2.37 [95].

$$Z_{1-2} = Z_1 + Z_2 \tag{2.35}$$

$$Z_{1||2} = \left(\frac{1}{Z_1} + \frac{1}{Z_2}\right)^{-1} \tag{2.36}$$

$$Z_{RC}(\omega) = \left(\frac{1}{Z_R} + \frac{1}{Z_C}\right)^{-1} = \frac{R}{1 + i\omega C} \tag{2.37}$$

In many cases it is not enough to describe materials solely with ideal circuit elements, which is the reason why constant phase elements (CPE) are commonly used instead of capacitors. The impedance Z_{CPE} of a CPE is related to the angular frequency and the two parameters n and Q via Equation 2.38. n is a factor between 0 and 1 and Q equals the capacitance C in the case of $n = 1$. The CPE element is often combined with a parallel connected resistance in a RCPE element. In this case it is possible to calculate the capacitance of a corresponding ideal capacitor via Equation 2.39 [96].

$$Z_{CPE}(\omega) = \frac{1}{(i\omega)^n * Q} \tag{2.38}$$

$$C = (R^{(1-n)} * Q)^{\frac{1}{n}} \tag{2.39}$$

2.4.2 Visualization of EIS

There are several ways to visualize impedance spectra, while the two most commonly used are the Nyquist diagram and the Bode diagram. A Bode diagram consist of two graphs plotting the absolute value of the impedance and phase angle against the AC frequency. In the Nyquist diagram the imaginary part of the impedance gets plotted against the real part. Both diagrams contain the same information, but emphasize different aspects. In the Nyquist diagram different equivalent circuit elements demonstrate rather characteristic curves. The impedance measurement of a RC element depicts, for instance, a semicircular structure (Figure 2.10 (a)). When the capacitor gets replaced with a CPE a flattened semicircle results. One big advantage of EIS is the possibility to differentiate between the conductivities of several circuit elements connected together. Thus, the grains of a material can be differentiated from the grain boundaries in between. Such an example is depicted in Figure 2.10 (b) [97].

2.4.3 Analysis of impedance spectra

To analyze impedance spectroscopy data, the measured spectra get commonly fitted with an idealized equivalent circuit model. From the then gained fitting parameters, electrochemical parameters of their physical causes can be calculated. Since the grain

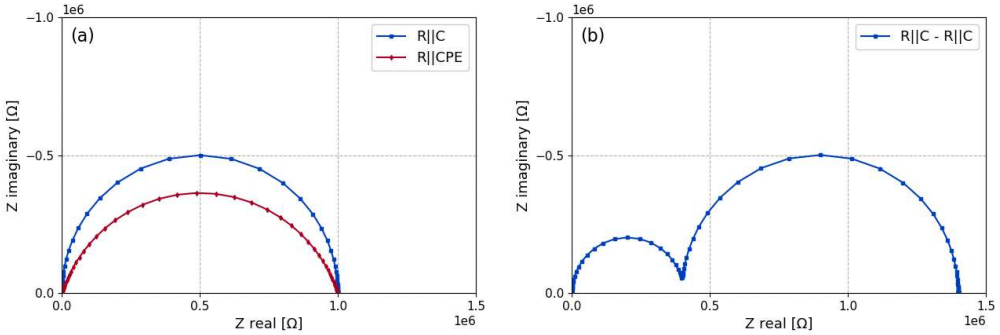

Figure 2.10: Simulated impedance spectra of idealized circuit elements: (a) Nyquist plot of a RC element in blue and a RCPE element with $n = 0.8$ in red; (b) Nyquist plot of two RC elements connected in series with different R and C values

boundaries of a material differ in their electrochemical behavior from the grains, an appropriate model has to be utilized to describe such a system. A very common model for this is the so-called brick layer model, which assumes cubic grains and laterally homogeneous grain boundaries, which all show identical properties (Figure 2.11). Through this simplifications, a polycrystalline material can be described with two RC(PE) elements connected in series. For a good description, the grain size of the material should show narrow Gaussian distribution and the grain shapes should be rather homogeneous. In materials with a bimodular grain size distribution current detours can impair the results. The model also reaches its limit for samples with a spatial distribution of the grain boundary properties and for porous samples, since a good contact between the grains is necessary [98]. The resistance in the grain boundary RC(PE) element can be described with Equation 2.40. Here, the grain boundary resistance R_{GB} correlates with the mean conductivity σ_{GB} of the grain boundaries, the thickness d_{GB} of the grain boundaries, the number of grain boundaries N_{GB} across the sample, and the sample area A. To simplify this expression, the number of grain boundaries across the sample can also be replaced by the ratio of the sample height h and the average grain size d_{Grain} [99]. Since values like d_{GB} and d_{Grain} are often unknown, it is often useful to introduce an effective grain boundary thickness $h_{GB,eff}$. This effective thickness can be seen as the height to which all grain boundaries across the material sum up to.

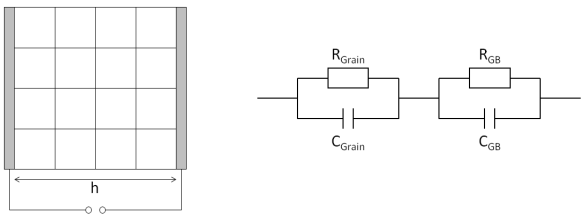

Figure 2.11: Two-dimensional brick layer model and corresponding equivalent circuit

$$R_{GB} = \sigma_{spez,GB} * \frac{d_{GB} * N_{GB}}{A} = \sigma_{spez,GB} * \frac{d_{GB} * h}{d_{Grain} * A} = \sigma_{spez,GB} * \frac{h_{GB,eff}}{A} \tag{2.40}$$

Since measurements at polycrystalline samples were also conducted within the scope of this work, the analysis of this data according to the brick layer model shall be shown. After plotting the measured data in a Nyquist diagram, they were fitted with the use of RCPE elements. The circuit elements used in the fitting can be assigned to their corresponding physical causes based on the respective calculated relative permittivity. By using Equation 2.41 the specific grain conductivity $\sigma_{spez,Grain}$ could be calculated from the grain resistance R_{Grain} and the proportions of the relatively cylindrical samples, namely the sample area A and the sample height h. The area was either calculated from the diameter d with Equation 2.42 or in the case of less roundish samples, a graphical determination of the sample area was done with the program 'ImageJ'.

$$\sigma_{spez,Grain} = \frac{1}{R_{Grain}} * \frac{h}{A} \tag{2.41}$$

$$A = (d/2)^2 * \pi \tag{2.42}$$

By using the Q and n factors of the RCPE elements assigned to the grains, the corresponding capacity C_{Grain} could be calculated with Equation 2.39. Further on, the sample proportions, the vacuum permittivity ϵ_0, and the previously calculated grain capacity were used to receive the relative permittivity $\epsilon_{r,Grain}$ of the grains. Since neither the thickness of the grain boundaries nor their number are known, the grain boundary conductivity could not be calculated directly. Under the assumption that the grain boundaries do have the same relative permittivity as the grains, the height $h_{GB,eff}$ to which all the grain boundaries across the sample sum up can be calculated with Equation 2.44. This height of the grain boundaries can now be used to calculate the specific conductivity $\sigma_{spez,GB}$ of the grain boundaries (Equation 2.45).

$$\epsilon_{r,Grain} = \frac{C_{Grain}}{\epsilon_0 * \frac{A}{h}} \tag{2.43}$$

$$h_{GB,eff} = \frac{C_{GB} * A}{\epsilon_0 * \epsilon_{r,Grain}} \tag{2.44}$$

$$\sigma_{spez,GB} = \frac{1}{R_{GB}} * \frac{h_{GB,eff}}{A} \tag{2.45}$$

In the last step the obtained conductivities can be plotted in an Arrhenius diagram. Here, the logarithm of all previously calculated specific conductivities are plotted against 1 divided by the temperature at which the conductivity was measured. Like discussed in

subsection 2.1.2 a linear behavior should be visible as long as no change in the conductivity mechanism appears. When this data gets fitted with a regression line in the form of $y = a + bx$, the activation energy E'_a can be calculated via Equation 2.46 from the slope b.

$$E'_a = 2.3 * b * k_B \tag{2.46}$$

2.5 Pulsed Laser Deposition (PLD)

Physical vapor deposition (PVD) techniques comprise a wide range of different vacuum deposition methods like pulsed laser deposition (PLD), evaporation, arc vapor deposition, ion platting, and sputtering. All PVD methods are based on the conversion of a material from the condensed phase into the gas phase initiated through a physical process and the subsequent condensation on a substrate, whereas the desired layer forms [100]. During this thesis pulsed laser deposition was used for the growth of doped STO, LSCr and YSZ thin films. PLD is regarded as the most effective technique for the growth of complex crystalline oxides. The condensation of the target material gets initiated by striking the target with a pulsed UV-laser beam, which leads to the absorption of the UV light and subsequently to the vaporization of the material [101]. This principle is depicted in Figure 2.12. At high laser fluences a nonequilibrium state is reached, where the vaporization is not dependent on the vapor pressures of the individual ionic species, which allows a stoichiometric ablation of the target material onto the substrate. Through the absorption of high energy densities by a small volume of material a plasma plume is generated [101]. The substrate is often placed in a heated sample holder, since the temperature has a notable effect on the morphology [102]. For every ablation a defined atmosphere in the PLD chamber has to be established. The gas phase can chemically interact with the ablated species, which is, for example, often used for the ablation of more complex oxides via the oxygen partial pressure. Furthermore, the background pressure can also be used to moderate the kinetic energy of the plasma plume formed [101].

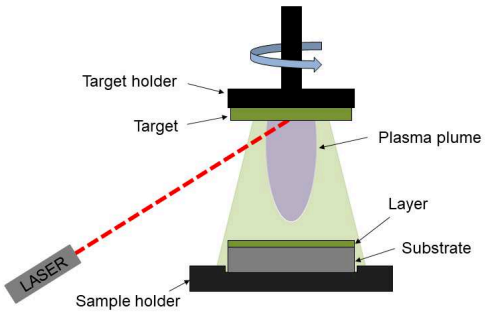

Figure 2.12: Principle of pulsed laser deposition (PLD)

3 Experimental

3.1 Preparation of polycrystalline samples

The polycrystalline samples can be divided into 3.9 % Fe-doped STO pellets (Fe:STO) and pure STO pellets. The individual samples differed from each other by small Sr/Ti and Sr/(Ti+Fe) ratio differences. Furthermore, for each composition there was at least one sample fabricated with oxidizing and one sample fabricated with reducing sintering steps. For the preparation of these pellets $SrCO_3$ (99.994 %, Sigma Aldrich, USA), TiO_2 (99.995 %, Alfa Aesar, USA), and Fe_2O_3 (99.995 %, Sigma Aldrich, USA) were used as starting materials. In the first step, these powders were weight in according to the desired stoichiometry and afterwards milled for 40 min in an agate mortar. After milling, the obtained powder mixtures were filled in flexible silicon rubber molds and put into an isostatic press (Paul Weber Masch. u. Apparatebau, GER). The isostatic pressing was carried out by applying 38 MPa pressure for 10 min, while subsequently releasing the pressure over the course of another 10 min. For the calcination step excess powder mixtures were filled into Al_2O_3 sintering boats and the pressed samples were placed on top of the powder bed. These powder beds should prevent a contamination of the samples with Al. This method was also repeated for all following sintering steps. The samples were heat treated at 980 - 1150 °C for 3 - 4 h in air, while remaining at 400 °C for 1 h during the warm up phase. The exact calcination times and temperatures can be divided into three calcination programs (CP1 - CP3) and are summarized in Table 3.1. All calcinations were carried out in a chamber furnace (Carbolite RHF 1600) with a heating and cooling rate of 5 °C/min.

Table 3.1: Calcination programs used for the preparation of polycristalline samples

	Rate	1. Dwell segment		2. Dwell segment	
CP1	5 K/min	1 h	400 °C	4 h	1100 °C
CP2	5 K/min	1 h	400 °C	3 h	980 °C
CP3	5 K/min	1 h	400 °C	4 h	1150 °C

While no mechanical stability was gained in the calcination step, the samples were milled again for 10 min and pressed again. The newly pressed pellets were now sintered either in the chamber furnace in air to produce oxidizingly sintered samples or in a 2.5 % H_2/Ar mixture in a tube furnace (Carbolite CTF 1800) to produce reducingly sintered samples. Here, a changed heating and cooling rate of 3 °C/min was applied.

After this first sintering step, the samples had still not the density and mechanical stability needed. Therefore, the sintered samples were again milled, pressed and sintered under similar conditions. Both sintering steps are outlined in Table 3.2. After this, the polycrystalline samples had a sufficient mechanical stability and were grinded to achieve a well-defined cylindrical form.

Table 3.2: Sintering times and temperatures used for preparing polycrystalline samples

Material	Atm.	Rate	1. Sinter step		2. Sinter step	
STO	Air	5 K/min	3.5 h	1300 °C	12 h	1500 °C
STO	H_2/Ar	3 K/min	5 h	1500 °C	6 h	1550 °C
Fe:STO	Air	5 K/min	12 h	1500 °C	12 h	1500 °C
Fe:STO	H_2/Ar	3 K/min	8 h	1500 °C	8 h	1500 °C

3.2 Preparation of single crystal samples

The single crystal samples consisted of pure STO ($SrTiO_3$(100)K, 10x10x0.5 mm, Crystec, GER), with 0.016 % Fe-doped and with 0.16 % Fe-doped single crystals (10x10x 0.5 mm, Alinason single crystals, GER). While these samples could be measured without any preparation steps, some of them were heat treated similar to the polycrystalline samples (1500 °C for 12 h in air). This was done to evaluate the effect of the sintering on the defect chemistry of the polycrystalline samples. Here, the samples were put on another single crystal to prevent contaminations.

3.3 Preparation of thin film samples

3.3.1 PLD target preparation

For the preparation of thin films, PLD targets with the adequate composition were needed. The differently doped STO targets had varying Sr/(Ti+doping) ratios of 0.95, 1.00, and 1.05. These targets were B-site doped with either 2 % Fe, 0.3 % Al, or 0.3 % Nb. Additionally, two samples with a Sr/(Ti+doping) ratio of 1.05 and 0.6 % Al- or Nb-doping were used. The stoichiometric Fe-, Al-, and Nb-doped targets and the Fe-doped STO target with Sr-excess already existed from prior works. Further targets were prepared in a simplified version of the preparation route of the polycrystalline samples. Additionally to the previously used $SrCO_3$, TiO_2, and Fe_2O_3 powders also Nb_2O_5 (99.99 %, Sigma Aldrich) and Al_2O_3 (99.998 %, Sigma Aldrich) powders were used for this step. The powders were again weight in, grinded for 40 min, pressed and calcined similar to the polycrystalline samples. However, after another grinding and pressing step the pellets were just sintered once. The exact calcination and sintering conditions differed between the targets and are outlined in Table 3.3 and in Table 3.4.

Table 3.3: Calcination times and temperatures used for the target preparation

	Rate	1. Dwell segment		2. Dwell segment	
0.3 % doping	5 K/min	1 h	400 °C	4 h	1000 °C
0.6 % doping	5 K/min	1 h	400 °C	4 h	1000 °C
Fe-doping	5 K/min	1 h	300 °C	4 h	1250 °C

Table 3.4: Sintering times and temperatures used for the target preparation

	Rate	1. Dwell segment		2. Dwell segment	
0.3 % doping	5 K/min	5 h	1500 °C		
0.6 % doping	5 K/min	2.5 h	1200 °C	2.5 h	1400 °C
Fe-doping	5 K/min	3 h	1500 °C		

3.3.2 Thin film deposition

All thin films were deposited with the "old PLD" setup, which is shown in Figure 3.1. The heated sample holder can be seen through the glass window in the middle, whereby the rotatable target holder is placed straight above it. The laser source was a KrF excimer laser (COMPexPro 205F, Coherent Inc., USA) with a wavelength of 248 nm. The beam path is attached to the left side of the vacuum chamber and a pyrometer (Heitronics KT19.99, GER) is placed on the top right side. The turbo molecular pump can be seen at the back of the apparatus.

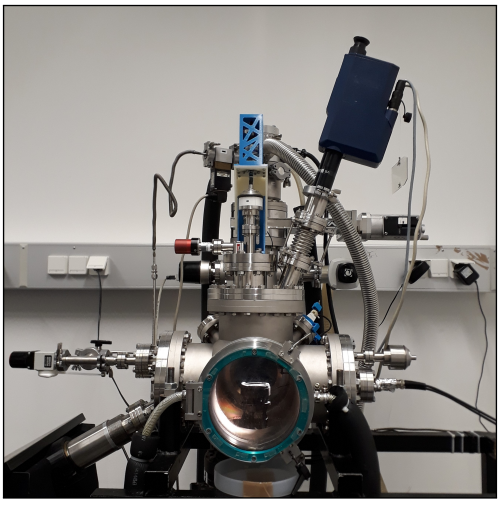

Figure 3.1: PLD setup used for the thin film preparations

Depending on the later use of the sample, STO thin films were ablated onto five different types of substrates. For impedance measurements, thin films of all targets were ablated onto Nb-doped STO single crystals ($SrTiO_3$: Nb 0.5 wt% (100)K, 10x10x0.5 mm, Crystec, GER). Additionally, thin films were ablated onto pure STO single crystals ($SrTiO_3$(100)K, 10x10x0.5 mm, Crystec, GER) for reciprocal space mapping, on MgO (MgO(100)K, 5x5x0.5 mm, Crystec, GER) and on YSZ (YSZ(100)K, 5x5x0.5 mm, Crystec, GER) single crystals for chemical analysis, as well as on sapphire single crystals (Saphir(0001)K, 10x10x0.5 mm, Crystec, GER) for profilometer measurements. All thin film depositions were carried out with the same parameters, which are shown in Table 3.5.

Table 3.5: Standard PLD settings for the ablation of doped STO

PLD parameters for doped STO targets	
Temperature	650 °C
O_2 pressure	1.5×10^{-1} mbar
Target distance	5.5 cm
Laser energy	400 mJ
Laser frequency	5 Hz
Ablation time	15 min
Pulses	4500
Film thickness	280 ± 50 nm

Additionally to the samples discussed above, further thin films were prepared with varying laser energies and deposition times. However, only the stoichiometric Fe-doped STO target was used for this. While the thin films prepared with a laser energy of 400 mJ were ablated for 20 min (6000 pulses), the thin films with 300 mJ were ablated for 30 min (9000 pulses), and the thin films with 270 mJ were ablated for 40 min (12 000 pulses). For this, Nb-doped STO single crystals and sapphire single crystals served as substrates.

3.4 Preparation of samples for UV light illumination

The samples used for voltage measurements under UV irradiation were prepared from polished polycrystalline samples as well as STO single crystals. The polycrystalline samples were either the STO pellets with varying stoichiometry produced in section 3.1 or newly made pellets. To simplify their preparation process STO powder (99 %, Sigma Aldrich, USA) was used as a starting material. During sample preparation, the powders were isostatic pressed and sintered at 1200 °C for 4 h in the chamber furnace. Some samples for UV light illumination also received thin films ablated onto their surfaces. On the top of the samples thin layers of $LaSr_{1-x}Cr_xO_3$ (LSCr) were added, which demonstrated a photoelectrical effect in previous experiments [4]. LSCr targets without Sr-doping (LSCr0), with 10 % Sr-doping (LSCr10), and with 20 % Sr-doping (LSCr20) were used. Additionally, also Y-stabilized ZrO_2 with 8 % Y_2O_3 (YSZ) layers were ablated onto the bottom of the samples, which serves as an electrolyte. The PLD parameters used for the preparation of these thin films are summarized in Table 3.6.

Table 3.6: PLD settings used for preparing the samples for UV light illumination

	LSCr	**YSZ**
Temperature	650 °C	650 °C
O_2 pressure	1.5×10^{-2} mbar	2.0×10^{-2} mbar
Target distance	5.2 cm	6.0 cm
Laser energy	400 mJ	400 mJ
Laser frequency	5 Hz	10 Hz
Ablation time	25 min	45 - 90 min
Pulses	7500	27 000 - 54 000
Film thickness	$\sim$ 200 nm	$\sim$ 300 - 600 nm

3.5 Preparation of current collectors

For later analyses different sorts of current collectors were added to the samples. The polycrystalline samples and the single crystal samples had porous Pt electrodes on both sides, which were added by brushing a platinum paste onto the samples and letting it dry in a drying chamber (BINDER, GER) at 130 °C. For the thin film samples and the specimens for UV light illumination, more sophisticated current collectors were needed. The thin film samples were equipped with micro-electrodes, with a diameter of 300 µm, to examine a more defined area of the thin films (Figure 3.2 (a)). The samples for the UV measurements needed grid-like structures (Figure 3.2 (b)) in order to be able to irradiate them and contacting the illuminated side. These current collectors were fabricated by negative photolithography in combination with Pt sputtering. Only for the specimen for UV light illumination, which were prepared from pure STO powder, a different approach was chosen. To simplify the preparation process of these samples further, the photolithography step was omitted and instead a shadow mask (Figure 3.2 (c)) with 200 µm bridges was placed on top of the samples before sputtering. For these samples Pt and Au grid-like current collectors were prepared. Meanwhile, the current collectors on the bottom side of all samples were still made of porous Pt electrodes.

(a) Micro-electrodes **(b)** Grid-like electrodes **(c)** Shadow mask

Figure 3.2: Microscope images of (a) Micro-electrodes on a Nb:STO single crystal and (b) grid-like electrodes on a STO single crystal; (c) Picture of the shadow mask used to prepare simplified grid-like electrodes

3.5.1 Negative photolithography

Most of the more sophisticated current collectors were manufactured by using negative photolithography in combination with sputtering. This whole process is often called "lift-off"-photolithography and is summarized in Figure 3.3. In the photolithography, a thin layer of a photoresist (ma-N 1420, Micro Resist Technology GmbH, GER) was applied on the sample surface by spin-coating. For drying the resin, the samples were put on a heating plate at 105 °C for at least 8 min. In the next step, a quartz glass mask was placed on top of the samples. This mask features the desired structures made of UV-blocking, low-reflective chromium. The photoresist was then crosslinked by illuminating it for 50 s through the mask with UV light (365 nm, 350 W, USHIO 350DP Hg lamp, Ushio Inc., JAP). Finally, the samples were swirled for 50 s in a developing agent (ma-D 533S, Micro Resist Technology GmbH, GER) and immediately afterwards washed in deionised water. The developing agent removes the non illuminated photoresist, with only a negative of the desired structure remaining. The current collectors themselves were added in the sputtering step. Afterwards, the photoresist negatives were solved in ethanol so that only the metal films remained, revealing the desired structures.

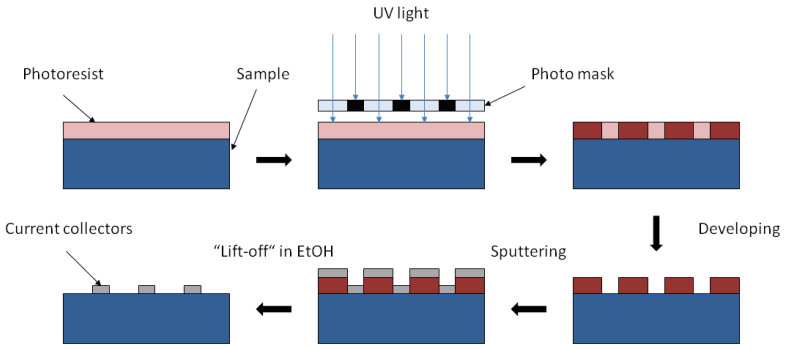

Figure 3.3: Principle of the "lift-off"-photolithography

3.5.2 Sputtering

For adding the final current collector, thin layers of platinum and gold were sputtered onto photolithographically treated sample surfaces or samples with a shadow mask on top of them. For this, a BAL-TEC MED020 sputtering device (BAL-TEC, now Leica Microsystems, AT) was used. The applied sputter parameters differed between both target materials and are summarized in Table 3.7. Before each sputtering the targets were presputtered against the shutter for 60 s to ensure a clean target surface while sputtering onto the samples. In the final step of the sample preparation, the photoresist negatives were solved in ethanol and the endings of the metal strips were connected by Pt or Au pastes brushed onto the outer areas of the sample.

Table 3.7: Sputtering settings used for the preparation of grids and micro-electrodes

	Platinum	**Gold**
Argon pressure	2×10^{-2} mbar	2×10^{-2} mbar
Sputter current	100 mA	100 mA
Sputter velocity	0.62 nm/s	1.05 nm/s
Sputter time	161 - 323 s	143 s
film thickness	100 - 200 nm	150 nm

3.6 Electrochemical Impedance Spectroscopy (EIS)

The impedance spectroscopy measurements were carried out in a tube furnace (GERO SR 70-200/ 12SO, GER), which is outlined in Figure 3.4. For the measurement of impedance spectra two different types of measuring setups were used. A sketch of the first measuring setup is depicted in Figure 3.5, which was used for the measurement of polycrystalline samples and single crystal samples. For contacting a sample, it was clamped between two broad platinum sheets. The temperature can be measured via a type S thermocouple incorporated in the tip of the measurement setup. For contacting micro-electrodes a more defined way of contacting the samples was needed. Therefore, a measuring setup like the one sketched in Figure 3.6 was used, which enables the contacting of single micro-electrodes with its sharp needle-like tip on top. The bottom of the sample was contacted with a broad sheet of platinum below the sample. The temperature measurement in this setup was accomplished by placing an external type K thermocouple alongside the measuring setup in the furnace. The impedance measurement itself was done with a Novocontrol Alpha A High Performance Frequency Analyzer (Novocontrol Technologies, GER) with a ZG-2 interface.

Figure 3.4: Measurement setup for impedance measurements

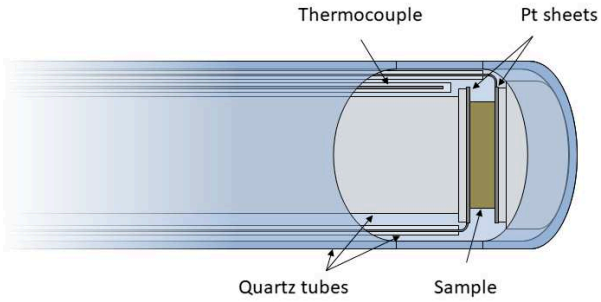

Figure 3.5: First measuring setup for impedance measurements

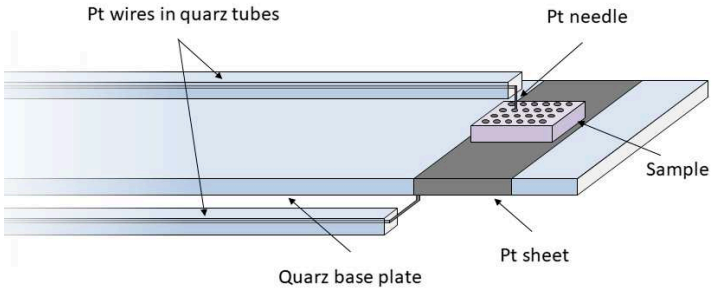

Figure 3.6: Second measuring setup for impedance measurements

3.6.1 Polycrystalline samples and single crystals

While the thermal history of the single crystals prior to the first measurement is not known, the polycrystalline samples were either sintered in oxidzing or reducing atmosphere during preparation. Therefore, it is reasonable to assume that all three types of samples do have oxygen vacancy concentrations frozen in at different equilibrium states. To achieve a better comparability, the samples were exposed to an equilibration process before starting the actual measurements. This was done by heating up the samples in the measurement setup to 700 °C and letting them equilibrate at this temperature for at least 12 h. For single crystal samples partly longer equilibration times were used. Afterwards, impedance measurements according to those in the following measurement cycle were conducted and the samples were quenched to room temperature by quickly pulling the measuring setup out of the furnace. Since the quenching did not occur instantaneously, a small derivation from the oxygen vacancy concentration at the 700 °C equilibrium in air is expected. But by executing the quenching process always in the same manner, all samples should still show comparable equilibrium states. For the main measurement cycle, impedance measurements at increasing temperatures were conducted. Starting at 200 $°C_{set}$ the temperature was increased in 25 °C steps up to 400 $°C_{set}$. The electrochemical analysis only started when the measured temperature did change less than 0.1 °C within 5 min. For better statistics, five impedance measurements with 30 s breaks in between were conducted at each temperature step. For the impedance measurements,

a measuring voltage of 0.1 V was applied with changing frequencies from 9×10^5 Hz to 1 Hz. While 10 points per decade were measured, each point took either 1 s or two periods of the current frequency to measure.

3.6.2 Thin film samples

After contacting their micro-electrodes, the thin film samples were heated up to 500 °C_{set} and left at this temperature for 2 h. Since the samples were all prepared the same way, no big differences in the temperatures at which the oxygen vacancies are frozen in should be present. The measurement cycle for thin film samples consisted of a temperature program with first increasing and then decreasing temperatures. Beginning at 500 °C_{set}, the temperature was at first raised in 25 °C steps up to 850 °C_{set} and then subsequently reduced down to 250 °C_{set} again with 25 °C steps. The impedance measurement started when the measured temperature did change less than 0.1 °C within 10 min. For better statistics, five impedance measurements with 30 s breaks were carried out at each temperature step. For the impedance measurements, a measuring voltage of 20 mV was applied. The AC frequency ranged from 9×10^5 Hz to 1 Hz, while measuring 10 points per decade for either 1 s or two periods of the current frequency.

3.7 Voltage measurements under UV light irradiation

The voltage measurements under UV light irradiation were carried out in a tube furnace (Gero SR 70-200/12, GER), which is depicted in Figure 3.7. The UV lamp (LED Engin, USA) is placed on the left side of the image and is connected with the interior of the furnace by a light guide. This optical light guide was a quartz glass rod with a diameter of 1 cm. The lamp has a wavelength of 365 nm and an intensity of 2.9 to 3.0 W. The measuring setup is located on the right hand side of the furnace, from which a close-up view is depicted in Figure 3.8. The distance between sample and light guide measures about 1 cm. The temperature was measured by a type S thermocouple, which was attached to the tip of the measuring setup next to the sample. A Keithley 2000 Digital Multimeter (Keithley Instruments Inc., USA) was used to measure the voltage difference between both sides of the sample. The voltage was measured every 0.5 s.

Figure 3.7: Measurement setup for voltage measurements under UV light irradiation

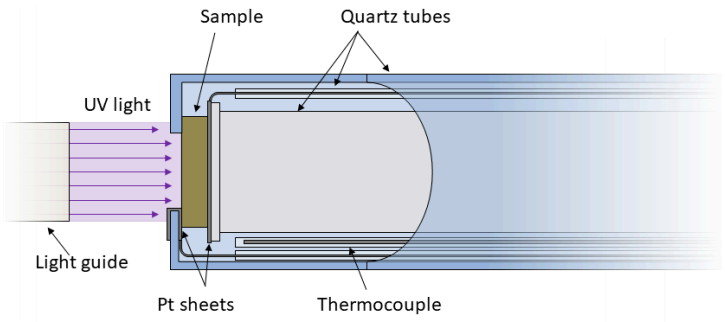

Figure 3.8: Measuring setup for the UV light illumination measurements

The samples were clamped in the measuring setup and placed inside the furnace. Afterwards, the setup was heated up to 345 °C while measuring the voltage between the current collectors on both sides of the sample. Even after several hours equilibrating at this temperature, a voltage offset remained. The samples are therefore denoted as equilibrated when this measured voltage offset stayed constant at a certain value, which was called dark voltage U_{dark}. The actual measurement consisted of three phases. In the first part, the dark voltage U_{dark} was measured for 15 min to determine the background. In the next step, the UV lamp was turned on for 15 min to measure how the UV irradiation affects the total voltage. In the end, the UV light was turned off again to measure the change in the total voltage for at least 15 min. Additionally to this standardized measurement process, a long time experiment was conducted. In the course of this, the voltage was measured, while turning the UV light on and off several times with varying illumination times. The sample chosen for this measurement consisted of a STO pellet with a Sr/Ti ratio of 0.995 and a LSCr10 top decoration layer. The illumination times ranged from 2 s to 8 h.

4 Results and Discussion

4.1 Sample preparation

4.1.1 Polycrystalline samples

For the undoped STO samples, pellets with Sr/Ti ratios of 0.995, 1.000, and 1.005 were prepared. These values were chosen in accordance to literature values [17, 19, 21, 22], since the nonstoichiometries should be big enough to cause a detectable effect but small enough for the samples still being single phased. The iron doped samples had 3.9 % Fe on the B-site and Sr/(Ti+Fe) ratios of 0.937, 0.942, 0.961, 0.980, 0.985, and 1.000 (nominal values). The calcination program CP1 with a maximal temperature of 1100 °C was mostly used to calcine the pressed powder mixtures. While not gaining any mechanical stability the powders visibly changed (e.g. powder mixtures with Fe_2O_3 turned from red to black). No differences in the calcined powders due to a different calcination program (CP2, CP3) were detectable.

The first sintering steps of the STO pellets were according to Table 3.2 the least intense sintering steps, after which no sufficient mechanical stability was achieved. Due to this, a preparation process with two separated sintering steps for all types of polycrystalline samples established during this work. The intensity of the first sintering step was increased for the Fe-doped samples. Although, they showed a relatively good mechanical stability after the first sintering step, still only small densities could be determined. The oxidizingly sintered Fe:STO samples showed an average relative density of 45.7 ± 3.9 %, while the reducingly sintered Fe:STO samples showed values in the range of 53.0 ± 6.9 %. This densities were calculated via the sample proportions and their weight. The theoretical density of undoped stoichiometric STO is 5.12 g/cm^3 [103]. However, also after the second sintering step no sample type reached density values close to the theoretical density (Table 4.1). The highest densities could be measured for the reducingly sintered STO pellets, showing relative densities of 85.3 ± 2.4 %. On the contrary, significantly higher relative densities (90 % and above) were reached in literature with similar sintering temperatures and durations [18, 19, 21–23]. In contrast, the oxidizingly sintered STO pellets showed the lowest relative densities of only 69.0 ± 1.7 %. Even though less pronounced, also for the Fe-doped samples higher densities could be determined for the reducingly sintered pellets, with relative densities of 78.5 ± 4.8 % and 82.0 ± 0.6 % for the oxidizingly and reducingly sintered pellets respectively.

Table 4.1: Calculated geometric densities of all polycrystalline samples for impedance measurements and relative densities compared to theoretical densities [103]

	Density	**Rel. Density [103]**
Ox. sintered STO	$3.53 \pm 0.09\,\mathrm{g/cm^3}$	$69.0 \pm 1.7\,\%$
Red. sintered STO	$4.37 \pm 0.13\,\mathrm{g/cm^3}$	$85.3 \pm 2.4\,\%$
Ox. sintered Fe:STO	$4.09 \pm 0.25\,\mathrm{g/cm^3}$	$78.5 \pm 4.8\,\%$
Red. sintered Fe:STO	$4.20 \pm 0.03\,\mathrm{g/cm^3}$	$82.0 \pm 0.6\,\%$

To investigate the effect of sintering further, the oxidizingly sintered STO samples were sintered a third time. For this, the samples were just sintered in the chamber oven at 1500 °C for 24 h without milling and pressing them again. But even with this additional sintering step the density did not increase, leading to a relative density of $69.2 \pm 2.5\,\%$. Lastly, the oxidizingly sintered Fe-doped samples were the only samples for which a pronounced correlation between the density and the nonstoichiometry was found. An increase in the nonstoichiometry led to a slightly higher density. Effects of the cation nonstoichiometry on the sintering behavior have been reported previously. Bäurer, Kungl, and Hoffmann found a faster densification for Sr-rich materials in the temperature range of 1050 to 1100 °C and a faster densification for Ti-rich materials in the temperature range of 1250 to 1350 °C [22]. Amaral et al. reported smaller grain sizes when a Sr-excess is present in the material and larger grain sizes for Sr-deficient materials [21].

During the sintering steps as well as later during the equilibration process, several color changes of the samples could be detected. A reducing sintering turns the other-wisely white grayish STO pellets pitch black (Figure 4.1 (a)). This color change derives from the abundance of electrons through oxygen depletion, as discussed in section 2.2. Hence, this color disappeared again through the equilibration step in oxidizing atmosphere before the impedance measurements. The oxidizingly sintered Fe:STO samples appeared gray, while the color of the reducingly sintered samples was a darker gray. This color changed to a reddish gray after the equilibration in oxidizing atmosphere, while no change in the color of the oxidizingly sintered samples were detected. Interestingly, two samples got cracks during the equilibration step. The reducingly sintered sample with a Sr/(Ti+Fe) ratio of 0.937 had small cracks on the sample surface and the sample with a Sr/(Ti+Fe) ratio of 0.980 had big cracks going through the whole sample (Figure 4.1 (b)).

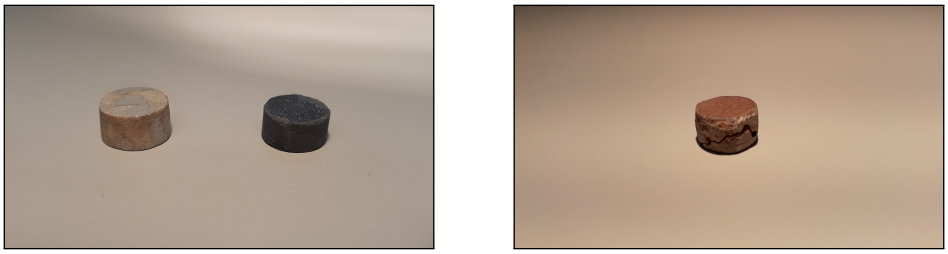

(a) Differently sintered STO pellets **(b)** Fe:STO pellet with cracks

Figure 4.1: Pictures of the samples: (a) Oxidizingly (left) and reducingly (right) sintered STO pellets, the oxidizingly sintered samples still has some Pt-remains on its top; (b) Reducingly sintered Fe:STO sample with a Sr/(Ti+Fe) ratio of 0.980 after equilibration showing big cracks

To confirm the phase purity of the samples, XRD spectra were measured with an angle range of 10 to 100 °. For all oxidizingly and reducingly sintered STO and Fe-doped STO samples a single phased cubic perovskite structure could be detected (Figure 4.2 and Figure 4.3). Only few additional reflections were measured, which had often just slightly higher intensities than the noise. Often, these possible impurities could be traced back to SiC, which most likely comes from the grinding steps before the XRD measurements. However, small amounts of TiO_2 are also indicated in the case of the oxidizingly sintered STO pellets (Figure 4.2). Interestingly, in the reducingly sintered Fe-doped STO samples some reflections could indicate the presence of metallic iron. Since the exsolution of nickel and other metals in strontium titanate under reducing conditions was reported before [104], an exsolution of metallic iron is a plausible explanation for this. This could also explain the color change from darker gray to a more reddish gray of these samples after equilibration, since these iron particle most likely oxidized during this process. Lastly, no peak-shifts were found between samples with different A/B-site ratios or varying sintering conditions.

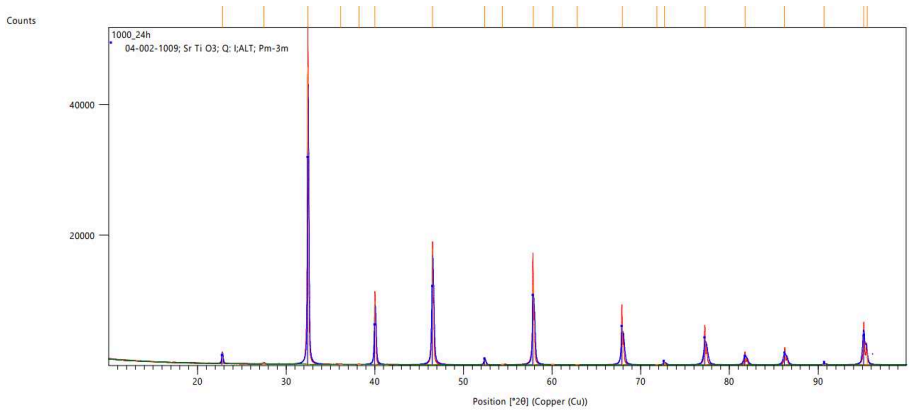

Figure 4.2: XRD diffraction pattern of the oxidizingly sintered stoichiometric STO pellet: The small reflex at about 27.5 ° indicates small amounts of TiO_2 next to the expected cubic perovskite structure of STO

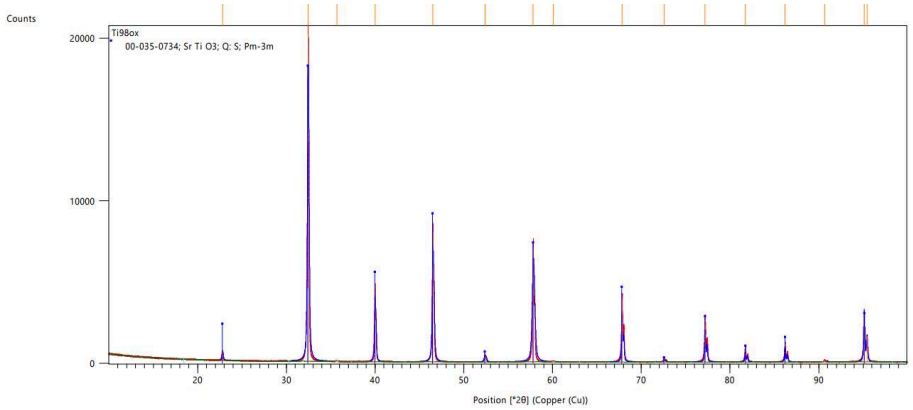

Figure 4.3: XRD diffraction pattern of the oxidizingly sintered Fe-doped STO pellet with a Sr/(Ti+Fe) ratio of 0.980: The pattern shows the expected cubic perovskite structure of STO

4.1.2 Thin film samples

Like discussed in subsection 3.3.2, thin films were ablated onto different substrates for different measurements. Next to the samples prepared for impedance spectroscopy measurements, further samples were prepared for film thickness measurements, chemical analysis, as well as reciprocal space mapping. The measured film thicknesses were, for instance, needed for the calculation of the exact conductivities of the thin films. Hence, they were determined, via the ablation of thin films on sapphire single crystals, which had small, dried-in ZrO_2 slurry droplets on its surface. After the ablation, the ZrO_2 could be removed via ethanol and a clean room cloth, leaving holes in the thin films. Thus, via a profilometer (DektakXT, Bruker Corporation, USA) the film thickness could be measured. Since the film thickness varied over the surface, always five measurements were made and the average was calculated. In Figure 4.4, these results are summarized for the Al-, Nb-, and Fe-doped thin films. Figure 4.4 (a) shows the dependency of the film thickness of the Sr/(Ti+doping) ratio of the target. Here, higher average thicknesses could be determined for the thin films with higher Sr/(Ti+doping) ratio. Only the Fe-doped sample with a Sr/(Ti+Fe) ratio of 1.05 deviates from this trend, which might result from the lower density of the corresponding target. On the other hand, thin films with a higher B-site doping showed also lower average film thicknesses than the respective thin films with only half the doping concentration (Figure 4.4 (b)). This trend could also result from lower densities of the targets with higher doping content due to the less harsh sintering conditions applied to them.

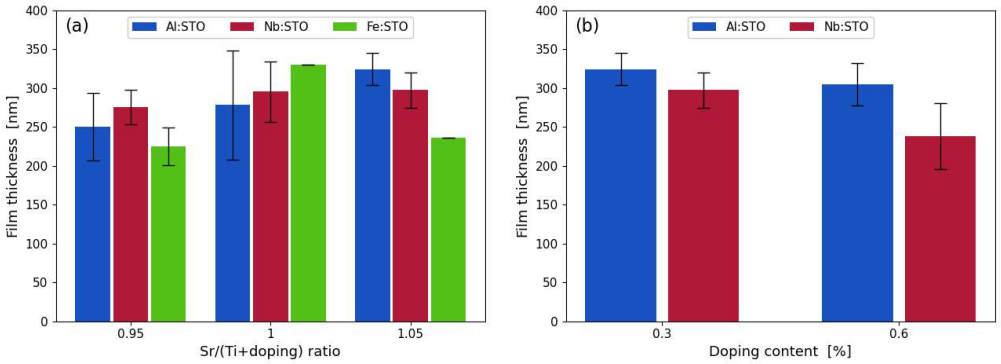

Figure 4.4: Comparison of the film thicknesses of different samples after ablating for 15 min: (a) Results for thin films with either 0.3 % Al- or Nb-doping or 2.0 % Fe-doping and varying Sr/(Ti+doping) ratios. For the Fe-doped samples with Sr/(Ti+Fe) ratios of 1.00 and 1.05 only the average film thickness was noted; (b) Results for thin films with Sr/(Ti+doping) ratios of 1.05 and different B-site doping content

Deviations in the film thicknesses of the samples with Fe-doped thin films ablated with varying laser energies were expected. To counterbalance this effect, longer ablation times were chosen when ablating with lower laser energy. While this effect is clearly visible, when looking at the ablation rates in Figure 4.5 (b), its effect was slightly overestimated, leading to slightly higher average thicknesses of the thin film ablated with 270 mJ laser energy (Figure 4.5 (a)).

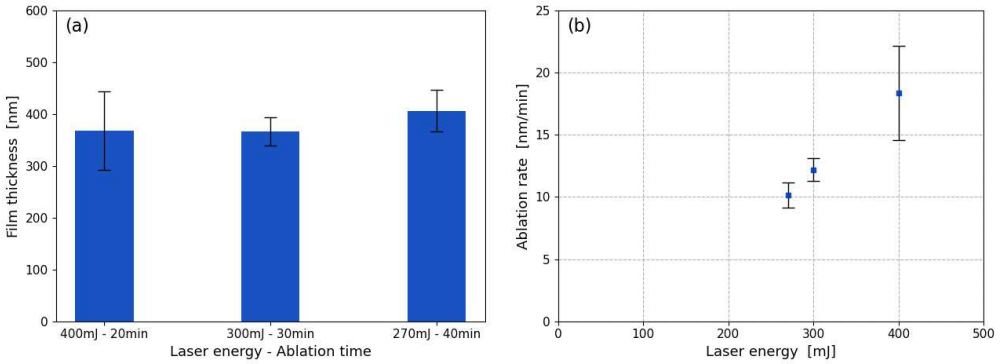

Figure 4.5: Impact of the laser energy on the film thickness of 2.0 % Fe-doped STO thin films with Sr/(Ti+Fe) ratios of 1.00: (a) Comparison of the thicknesses of Fe-doped STO thin films ablated with different laser energies and ablation times; (b) Comparison of the ablation rates of Fe-doped STO thin films ablated with varying laser energies

Due to the fact that thin films can differ in their chemical composition from the targets they were ablated from, a chemical analysis was conducted. Hence, the samples were examined for possible deviations in the B-site doping content from their expected values. For these measurements, Al- and Nb-doped thin films ablated onto either MgO or YSZ single crystals were used as specimen. After dissolving the individual samples, they were analyzed via inductively coupled plasma mass spectrometry (ICP-MS). For this, the Nb-doped thin films were all ablated onto MgO single crystals. The corresponding Nb/(Ti+Nb) ratios are in very good agreement with the nominal values. For the Al-doped STO thin films on MgO, the problem arose that the M(Mg+H) signal interfered with the the M(Al) signal. Thus, no Al-content could be determined for these samples. Due to this, the two later prepared samples with an Al-doped STO thin film were ablated onto YSZ single crystals. However, also for these samples Al proved to be difficult to detect, resulting in the measurement of very low Al concentrations of only about 0.04 %.

To characterize the crystal structure of the thin film samples, reciprocal space mapping measurements were conducted. Here, the thin films ablated onto pure STO single crystals were measured. Thus, for an epitactical film growth the examined reflection peak can be compared to the respective reflection peak of the STO substrate. Since these measurements are rather time consuming, only the Nb-doped thin films with different Sr/(Ti+Nb) ratios were measured and only the (200) reflection was examined. Interestingly, only for the sample with a Sr/(Ti+Nb) ratio of 1.05 in the thin film only one visible reflection peak could be measured (Figure 4.6). The other two samples showed next to the reflection peak of the STO substrate also a peak below it, which indicates a slightly larger lattice constant. This could be explained by a large number of cation vacancies being present in these two samples.

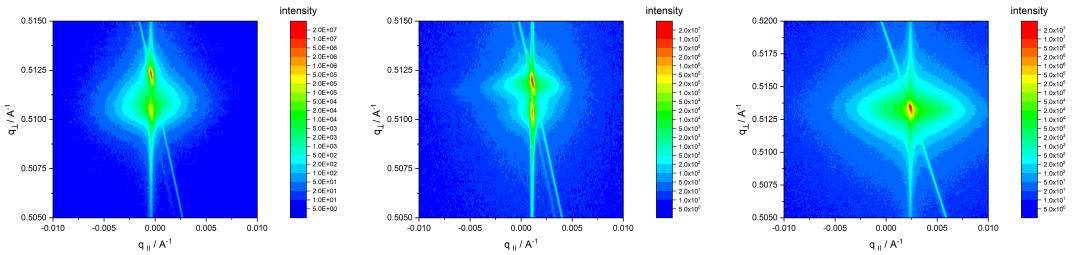

(a) Sr/(Ti+Nb) = 0.95 **(b)** Sr/(Ti+Nb) = 1.00 **(c)** Sr/(Ti+Nb) = 1.05

Figure 4.6: Results of the reciprocal space mapping: Three Nb:STO thin films with 0.3 % Nb-content and different Sr/(Ti+Nb) ratios

4.1.3 Samples for UV light illumination

The STO phases of the light illumination samples were mostly made of single crystals or the same polycrystals already discussed in subsection 4.1.1. Still, some samples had STO phases made of newly prepared STO polycrstals with STO powder as starting material and a simplified preparation route. The shortened preparation route discussed in section 3.4 provided mechanically stable samples with a density comparable to the other polycrystalline pellets. Hence, a density of $3.58 \pm 0.06\,\mathrm{g/cm^3}$ ($69.8 \pm 1.2\,\%$) was achieved, in comparison to the $3.53 \pm 0.09\,\mathrm{g/cm^3}$ of the oxidizingly sintered STO pellets prepared from individual powders.

The lithographic preparation of Pt grids proved to be a long many-step-process, which often did not result in a satisfactory outcome. The main problems were that the grids sometimes partly peeled off or that parts of the Pt negatives remained on the sample surfaces. These problems appeared for the polcrystalline and single crystalline samples, but were the worst for polycrystalline samples prepared from STO powder, with grids peeling of almost completely almost every time. This was also a major reason why a switch to the use of a shadow mask was implemented. This preparation route was much simpler and the resulting grids did not show any peeling effects. On the other hand, the prepared grids showed broader bridges and broader gaps in between, which all also stronger varied in their breadth (Figure 4.7). Another disadvantage was the fact that either brushing Pt or Au on the outer sides of the samples was necessary to connect the single bridges.

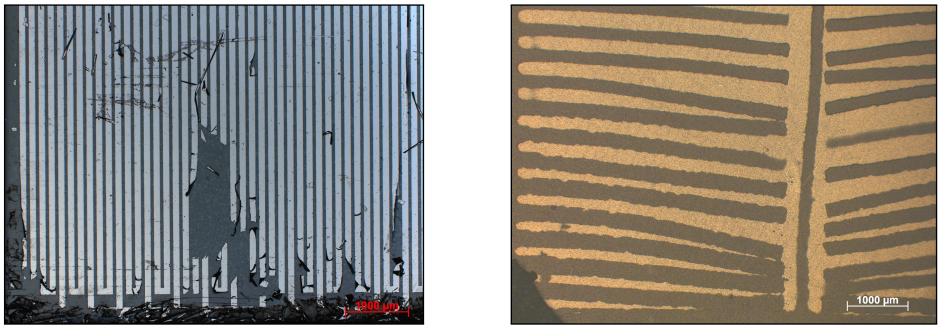

(a) Photolithographic route **(b)** Shadow mask route

Figure 4.7: Microscope images of two kinds of grid-like electrodes: (a) Grid-like electrode prepared via the photolithographic route on a STO single crystal; (b) Grid-like electrode prepared via the shadow mask on a polycrystalline STO pellet (Image taken before the Pt-brushing step)

4.2 Impedance spectroscopy of polycrystalline samples

Figure 4.8 depicts typical Nyquist plots of different polycrystalline samples at different temperatures. The impedance spectra of the oxidizingly sintered samples at 700 °C can be described with a x-axis offset and a semicircle with a shoulder at lower frequencies (Figure 4.8 (a)). The shoulder can be explained by another smaller semicircle, which overlaps with the larger semicircle. Thus, these spectra were fitted with a resistance and two RCPE elements connected in series. As discussed in subsection 2.4.3, these features where assigned according to their relative permittivities, which were calculated via the proportions of the samples and the coresponding capacity. The capacity itself was calculated from the R, Q, and n factors of the RCPE elements via Equation 2.39. Hence, for the oxidizingly sintered samples at 700 °C the resistance was assigned to the grains and the larger semicircle to the grain boundaries, while the last small semicircle might originate from an electrode effect.

Between 200 °C_{set} and 400 °C_{set} the impedance spectra revealed only two semicircular structures (Figure 4.8 (c) and (e)), so it was sufficient to fit them with two RCPE elements connected in series. Here, the smaller one was corresponding to the grain conductivity and the larger one to the grain boundary conductivity. With raising temperatures the size of both semicircles decreased. At lower temperatures only few measurement points of the grain boundary semicircle were measured, which resulted in the fact that only the measurements at the highest temperatures revealed useful grain boundary conductivities. Therefore, this work deals with a stronger focus on the grain conductivities of the polycrystalline samples.

The reducingly sintered pellets showed an elongated semicircular structure at 700 °C (Figure 4.8 (b)). This might derive from the strong overlap occurring at temperatures between 200 °C_{set} and 400 °C_{set} (Figure 4.8 (d) and (f)). In these spectra the individual semicircles are hardly recognizable. This reduced the accuracy of the analysis notably. For better comparability, the fitting still occurred with the same equivalent circuits like used for the oxidizingly sintered samples, even though larger fitting deviations appeared.

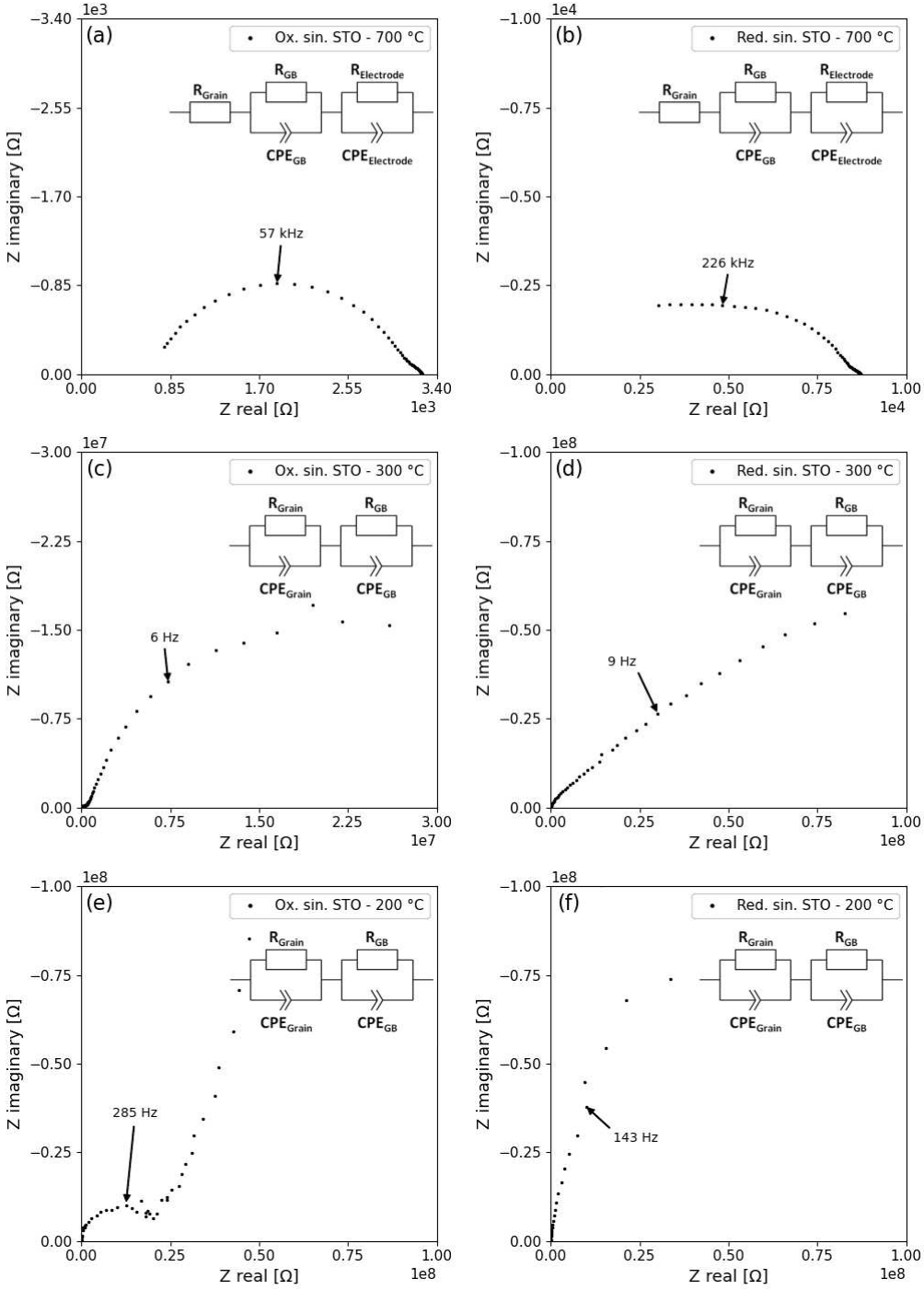

Figure 4.8: Comparison of the impedance spectra of oxidizingly sintered and reducingly sintered STO pellets at different temperatures

4.2.1 Grain conductivity of undoped STO samples

In Figure 4.9, the Arrhenius diagram of the grain conductivity of three oxidizingly sintered STO pellets between 200 °C$_{set}$ and 400 °C$_{set}$ is depicted. In this temperature interval all measured values follow an Arrhenius-like trend. Hence, activation energies in the range of 0.91 to 0.97 eV could be determined. These values are in agreement with activation energy values of undoped and slightly acceptor doped STO from literature [16, 21, 46, 47, 99, 105]. The mobile defects in these samples are oxygen vacancies and electron holes. Supposed the measured conductivity is mainly electronic, then the activation energy reflects the energy for trapping holes in gap states, most probably in Sr vacancies. However, the activation energy might also come from the diffusion of oxygen vacancies, since values in this range are reported in literature [16, 21, 47]. It further appears that an understoichiometric Sr-content increases the conductivity of the STO, while only a very small conductivity increase appears to happen through an overstoichiometric Sr-content. Such an increase in conductivity due to nonstoichiometry, which shows a bigger effect towards Sr-deficiency, was already reported by Amaral et al. [21].

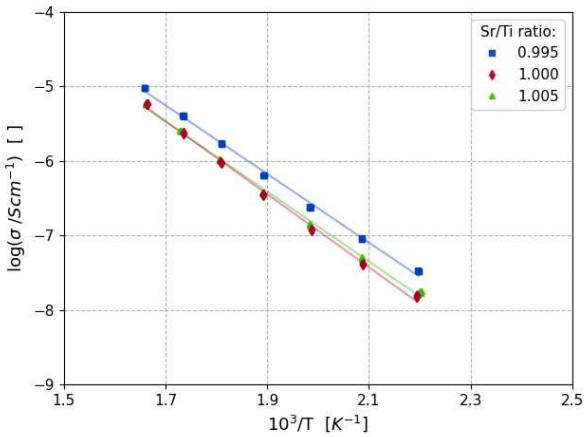

Figure 4.9: Arrhenius plot of oxidizingly sintered STO pellets with varying cation nonstoichiometry after the usual sintering process and an equilibration at 700 °C

Figure 4.10 (a) displays the grain conductivities of the STO samples sintered for an additionally 24 h in an Arrhenius diagram. It is readily apparent that the differences between the grain conductivities of samples with different Sr/Ti ratios decreased heavily due to the additional sintering step. Figure 4.10 (b) to Figure 4.10 (d) compare the conductivities of each sample before and after this sintering step. Here, it is further visible that the conductivity of each sample increased through the third sintering step. A possible explanation for this is an increase in the number of Sr vacancies due to the ongoing partial Schottky reaction during this third sintering step. According to Moos et al., a partial Schottky equilibrium concentration of $[V''_{Sr}]*[V^{\bullet\bullet}_{O}] = 2.4 \times 10^{37}\,cm^{-3}$ is given for 1500 °C [67] and together with thermodynamic data for oxygen exchange in air [106] this leads to a Sr vacancy concentration in the percent range. As discussed in subsection 2.2.1, this can lead to an increased number of holes in the material. While this

would increase the overall conductivity, the impact of the previously installed Sr/Ti ratio could be almost eliminated. Meanwhile, the activation energy of the grain conductivity decreased slightly for each sample composition to values between 0.88 and 0.92 eV.

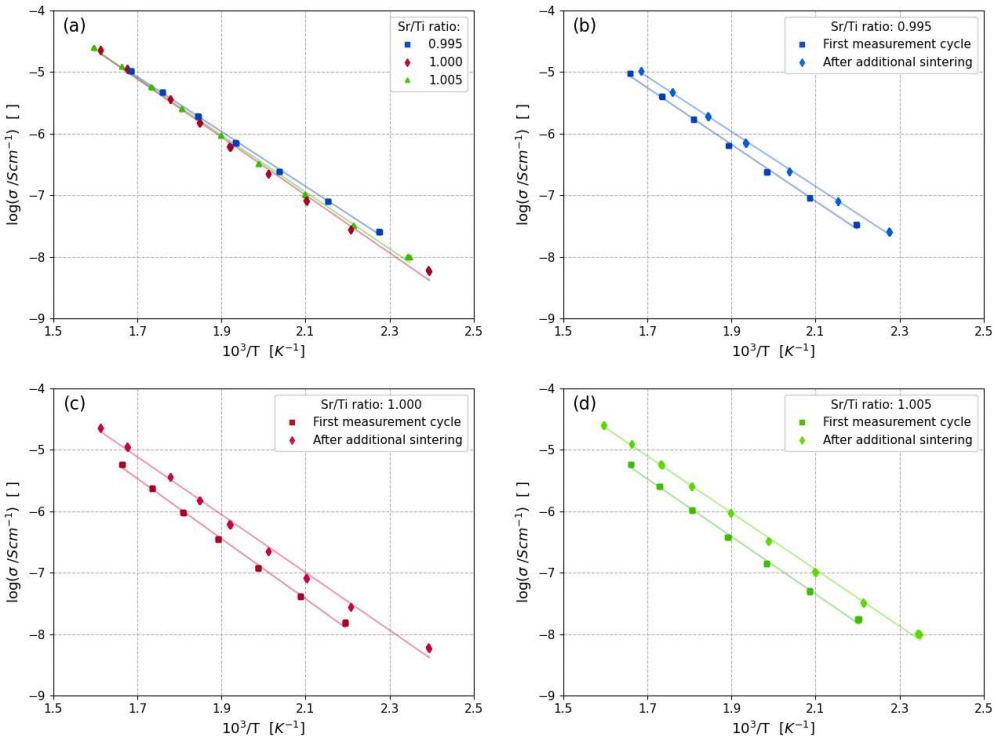

Figure 4.10: Effect of longer sintering times on the conductivity of oxidizingly sintered STO pellets: (a) Arrhenius plot of STO pellets with varying cation non-stoichiometry sintered for an additional 24 h and equilibrated at 700 °C; Arrhenius plot of oxidizingly sintered STO pellets with a Sr/Ti ratio of (b) 0.995, (c) 1.000, (d) 1.005 and different sintering history

In Figure 4.11, the grain conductivities of the reducingly sintered STO pellets are compared to the previously discussed oxidizingly sintered samples. The Arrhenius curves of these samples differ in several ways from the oxidizingly sintered samples. First of all, the overall conductivity of these samples is much smaller than of those sintered in oxidizing atmosphere. Additionally, the measurements do not show a linear behavior in the Arrhenius plot, but rather show a kink in a temperature range of about 246 to 296 °C. Therefore, the determination of the exact activation energies proves to be more difficult. At temperatures below the kink activation energies of about 0.33 to 0.48 eV were determined. However, in this regime are also larger deviations of the individual measuring points present. At higher temperatures activation energies of 0.91 to 0.94 eV could be determined for the understoichiometric and stoichiometric sample respectively. These values fit well to the values of the oxidizingly sintered samples, indicating a similar conduction mechanism. Only the overstoichiometric sample shows a slightly higher activation energy of 1.07 eV.

By comparing the sample conductivities to each other, it can be seen that once again the sample with understoichiometric Sr-content possesses the highest grain conductivity. However, in contrast to the oxidizingly sintered STO samples the sample with a Sr/Ti ratio of 1.005 exhibits only at low temperatures a comparable grain conductivity to the stoichiometric pellet. In the higher temperature regime, this sample displays the smallest conductivity.

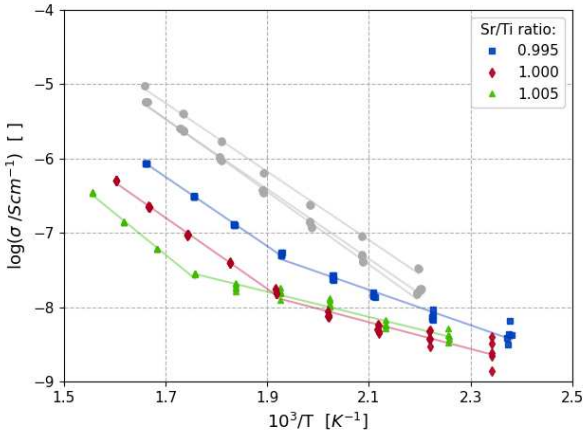

Figure 4.11: Arrhenius plot of reducingly sintered STO pellets with varying cation nonstoichiometry after equilibration at 700 °C; For comparison, the conductivities of the oxidizingly sintered samples are depicted in grayscale

4.2.2 Grain conductivity of Fe-doped STO samples

Next to the samples consisting of pure STO pellets, also impedance measurements on Fe-doped polycrystals were conducted. Figure 4.12 depicts the results of the measurements of the oxidizingly sintered pellets in an Arrhenius plot. While only small conductivity differences between the samples with an understoichiometric Sr-content are visible, the stoichiometric sample differs stronger in its behavior. Hence, much higher conductivity values could be measured, but also a lower activation energy, leading to a smaller difference in conductivity at the highest temperatures. For this sample, an activation energy of 0.50 eV could be determined. Meanwhile, the samples showing a nonstoichiometry had activation energies in the range of 0.80 to 0.85 eV. Nonetheless, for these samples the Sr depletion showed the opposite effect like for the undoped polycrystals, leading to a lower grain conductivity. While this effect could theoretically result from Fe ion being partially forced to the A-site of the perovskite structure, further experiments would be needed to verify this. However, less nonstoichiometric samples might have been able to depict the change of the grain conductivity from the state of the stoichiometric sample to the state found for all nonstoichiometric samples.

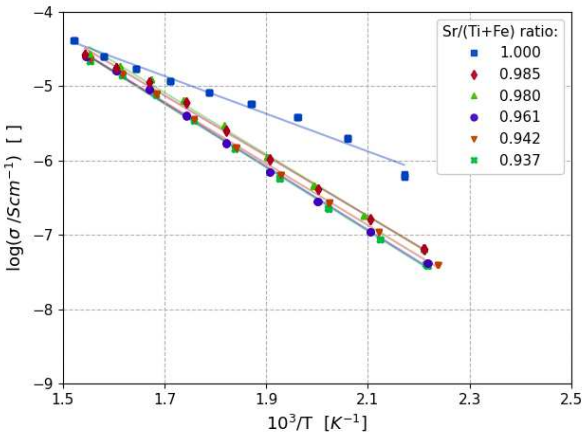

Figure 4.12: Arrhenius plot of oxidizingly sintered Fe-doped STO pellets with varying cation nonstoichiometry after equilibration at 700 °C

Figure 4.13 depicts the conductivities of these samples compared to the oxidizingly sintered STO polycrystals and the same samples with an additional sintering step of 24 h at 1500 °C. In both cases, a small difference in the slope of the conductivity values is visible, which leads to the slightly smaller activation energy of the Fe-doped samples. Interestingly, the doping of 3.9 % Fe seems to only lead to a small increase in the conductivity compared to the regularly sintered undoped samples. Thus, the STO sample with a Sr/Ti ratio of 0.995 shows at higher temperatures already similar conductivies like the understoichiometric Fe:STO samples. Hence, the samples with an additional sintering step even show comparable conductivity values to the Fe-doped samples at similar temperatures. This may again be due to establishing substantial Sr vacancy concentrations by a partial Schottky equilibration at 1500 °C. The Sr vacancies act as acceptors and the additional Fe-doping does not change much of the total acceptor concentration, particularly if also Fe on the A-site comes into play. However, the outlier curve for Sr/(Ti+Fe)=1.00 is still not well understood.

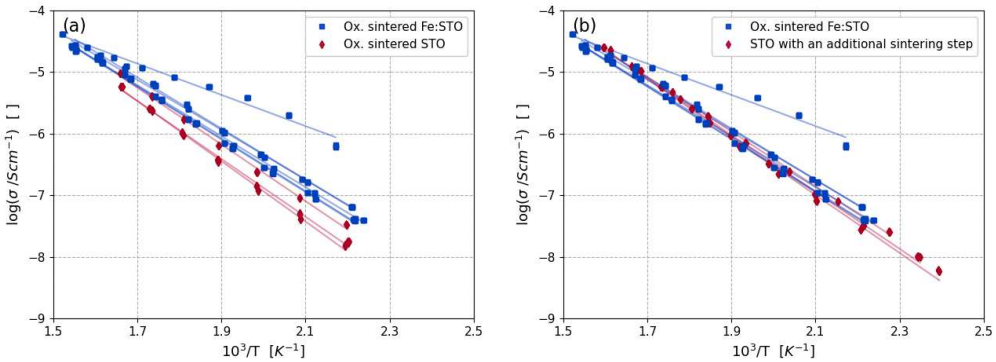

Figure 4.13: Comparison of the conductivities of the oxidizingly sintered Fe-doped samples and undoped samples: (a) Arrhenius plot of the Fe:STO samples and the STO samples after the usual sintering process, equilibrated at 700 °C; (b) Arrhenius plot of the Fe:STO samples and the STO samples, which were sintered for an additional 24 h, both sample types were equilibrated at 700 °C

Similar to the undoped polycrystalline samples, also for the Fe-doped pellets the reducingly sintered samples obtained general smaller conductivities than the oxidizingly sintered samples (Figure 4.14). Furthermore, most reducingly sintered samples also show rather similar conductivities independent of their Sr-deficiency. Only two samples deviate from the general scheme. The sample with a Sr/(Ti+Fe) ratio of 0.980 obtains clearly lower conductivities than all other samples. It is important to note that this is also the sample, which obtained big cracks running through it during the equilibration process. Thus, it is reasonable to denote this sample as an outlier. Furthermore, the stoichiometric samples shows much higher conductivities than the rest of the samples. However, this sample is also the only sample, for which a stable sintering atmosphere can not be completely guaranteed, since a halted gas flow was detected during cooling down. It is not clear how long the gas flow was interrupted, but the possibility of a less reducing sintering atmosphere makes it difficult to compare this sample to others. Still, even the remaining samples show a stronger scatter in their activation energies, with the lowest value for the sample with a Sr/(Ti+Fe) ratio of 0.985 of 0.64 eV and the highest value of 1.06 eV for the sample with a Sr/(Ti+Fe) ratio of 0.961. The samples with Sr/(Ti+Fe) ratios of 0.937 and 0.942 show activation energies of 0.81 eV and 0.98 eV respectively. Lastly, in contrast to the reducingly sintered undoped samples theses samples do not show well pronounced kinks in their slopes.

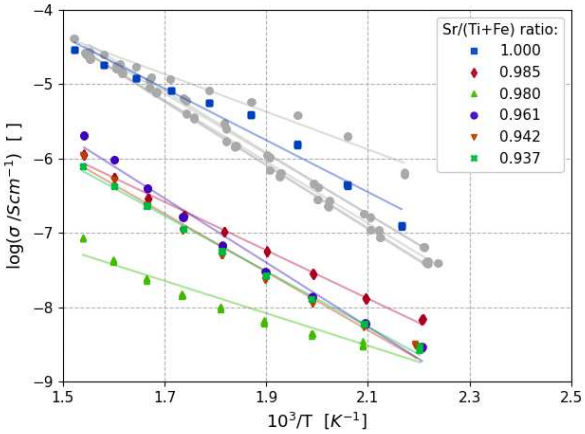

Figure 4.14: Arrhenius plot of reducingly sintered Fe-doped STO pellets with varying cation nonstoichiometry after equilibration at 700 °C; For comparison, the conductivities of the oxidizingly sintered samples are depicted in grayscale

In the Arrhenius plot in Figure 4.15, the conductivities of the reducingly sintered Fe-doped STO pellets are depicted in comparison to the accordingly sintered pure STO pellets. Similar to the oxidizingly sintered samples, no big conductivity increase seems to be caused by the Fe-doping. Hence, the STO pellet with a Sr/Ti ratio of 0.995 even shows higher conductivities than all Fe-doped samples with a Sr-deficiency. Furthermore, the difference in the temperature dependency of their conductivities is readily apparent.

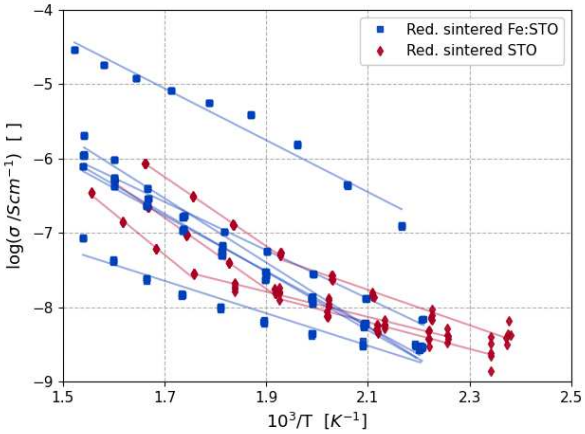

Figure 4.15: Arrhenius plot of all reducingly sintered Fe-doped and undoped STO pellets after equilibration at 700 °C

4.2.3 Grain boundary conductivity of polycrystalline samples

Due to the more problematic fitting of the corresponding semicircles, the grain boundary conductivities proved to be more difficult to evaluate compared to the grain conductivities. Still, a short discussion of these results shall be given. Figure 4.16 depicts the grain boundary conductivities of all undoped STO samples. Even at the highest temperatures only values below 10^{-8} S/cm could be reached, making the grain boundary conductivities significantly smaller than the grain conductivities. In Figure 4.16 (a) a lack of values in the intermediate temperature range is visible for some oxidizingly sintered pellets. Here, nominal conductivity values in the range of 10^{-18} S/cm to 10^{-21} S/cm were measured. While the sample with a Sr/Ti ratio of 0.995 is the only sample not showing this behavior, it is important to note that all three samples showed these low values in this temperature range after the additional sintering step. These extremely low values can most likely be traced back to the problematic fitting of the corresponding impedance spectra. Therefore, only the conductivity values measured at the highest temperatures can be seen as realistic values. The calculated activation energies varied strongly, with values between 1.21 eV for the sample with a Sr/Ti ratio of 0.995 and 1.94 eV for the sample with a Sr-excess. While the examination from very few measurement points has to be taken into account, also Amaral et al. found a strong dependency of the grain boundary activation energy on the cation nonstoichiometry [21]. Additionally, an increase in the grain boundary conductivities with decreasing Sr-content is visible for these samples. Meanwhile, the reducingly sintered STO polycrystals show also at lower temperatures reasonable grain boundary conductivities (Figure 4.16 (b)). Interestingly, only a small conductivity increase with increasing temperatures could be detected, with corresponding activation energies in the range of 0.1 to 0.2 eV. Only at the highest temperatures, the temperature dependency slowly increases, which might indicate a change in the conducting mechanism. For these samples, no dependency of the grain boundary conductivity on the nonstoichiometry was detectable. Compared to the oxidizingly sintered samples, the grain boundary conductivity of the reducingly sintered samples is slightly higher, with only the Sr-deficient oxidizingly sintered sample reaching similar values at the highest temperatures.

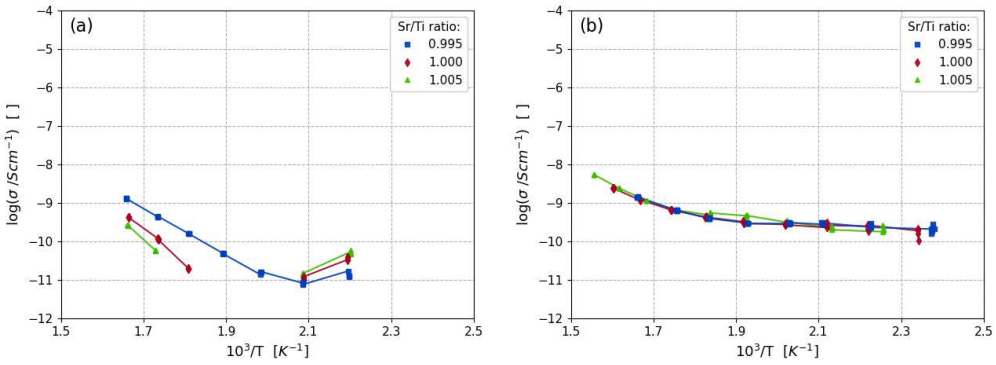

Figure 4.16: Arrhenius plot of the grain boundary conductivity of the (a) oxidizingly and (b) reducingly sintered undoped STO pellets after equilibration at 700 °C

Figure 4.17 depicts the grain boundary conductivities of the Fe-doped STO pellets. For these samples, only the oxidizingly sintered sample with a Sr/(Ti+Fe) ratio of 0.961 showed extremely low conductivity values in a certain temperature range. Still, at higher temperatures the grain boundary conductivity of this sample shows a similar behavior like for the rest of the understoichiometric oxdizing sintered Fe:STO pellets. However, the stoichiometric sample differs once again in its behavior from the understoichiometric samples, showing much higher conductivity values. Furthermore, an activation energy of about 0.78 eV can be determined for this sample. This value was calculated without taking the values at the highest temperatures into account, since a flattening of the slope seems to appear. In comparison, the understoichiometric samples show activation energies of about 1.0 eV to 1.2 eV, with the values measured at lower temperatures differing from this behavior. The reducingly sintered samples show at lower temperatures a higher conductivity but also a flatter slope. At higher temperatures, similar grain boundary conductivities like for the oxidizingly sintered samples could be determined for most of the samples. Here, the change in the slope seems to happen more gradually, without a pronounced kink. Only the stoichiometric sample and the sample with a Sr/(Ti+Fe) ratio of 0.985 deviate from the general scheme, by showing significantly higher grain boundary conductivities. Interestingly, the sample with a Sr/(Ti+Fe) ratio of 0.980 did not really show deviating properties, even though this sample obtained huge cracks and a big difference in grain conductivity was measured due to it.

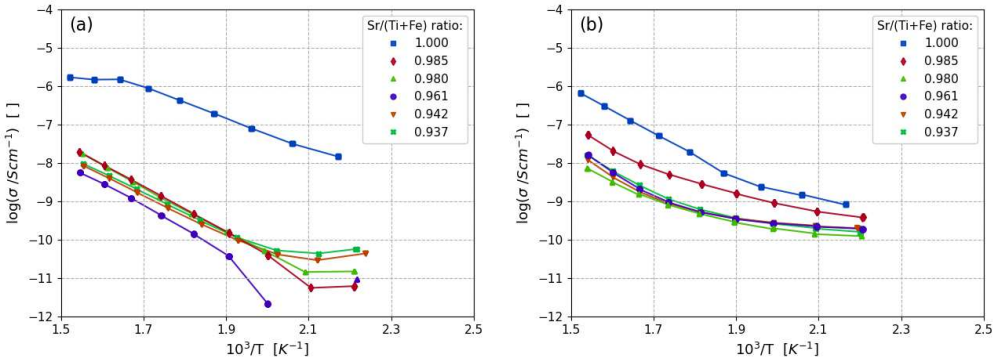

Figure 4.17: Arrhenius plot of the grain boundary conductivity of the (a) oxidizingly and (b) reducingly sintered Fe-doped STO pellets after equilibration at 700 °C

4.2.4 High temperature conductivity of polycrystalline samples

Another interesting value, which is worth discussing, is the conductivity at 700 °C of the individual samples (Figure 4.18). These values do not reflect samples with an oxygen vacancy concentration in a frozen in state, but rather the samples being in equilibrium with their surroundings. Similar to the values measured at lower temperatures, higher grain conductivities can be determined for the oxidizingly sintered STO pellets compared to the reducingly sintered pellets. Furthermore, in both cases the highest measured conductivity belongs to the understoichiometric sample. Meanwhile, the oxidizingly sintered Fe-doped samples show about double as high grain conductivities as the oxidizingly sintered STO pellets at this temperature. Still, no clear dependency of these values on the nonstoichiometry can be detected.

While most of the reducingly sintered Fe:STO pellets obtain grain conductivities in the range of 1.1×10^{-3} S/cm to 1.5×10^{-3} S/cm, significantly higher values could be determined for the sample with a Sr/(Ti+Fe) ratio of 0.985 and the stoichiometric sample. Please note that no evaluable impedance spectra could be measured for the sample with a Sr/(Ti+Fe) ratio of 0.980, which obtained its cracks at some point during this equilibration process. From the defect chemical model of Fe:STO [106], one can calculate that a concentration of 3×10^{-3} S/cm corresponds to a Fe concentration of about 8×10^{18} cm^{-3}, i.e. 0.05 %, which is much less than the nominal concentration of 3.9 %. This is again an indication that Fe might be partly on the A-site of the Fe:STO (please note that this estimate does not include the possible presence of additional Sr vacancies).

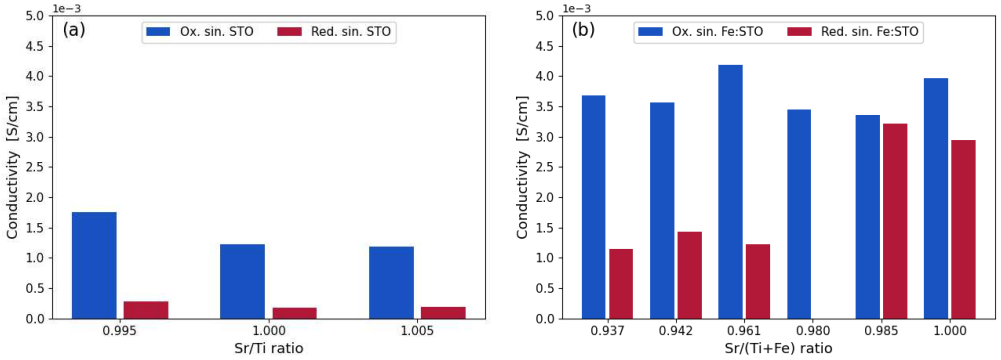

Figure 4.18: Comparison of the grain conductivity of all (a) undoped and (b) Fe-doped STO pellets after the equilibration at 700 °C but before the quenching

4.2.5 Relative permittivity of polycrystalline samples

Next to the conductivity values, also the relative permittivities of the grains were determined. Like discussed in section 2.2, strontium titanate obtains a relative high relative permittivity of about 300 at room temperature. This value was also used to assign the RCPE units of the fit circuit corresponding to the grains. The relative permittivities were received from the Q, n, and R values of the RCPE units of the fit circuits as discussed in subsection 2.4.3. In Figure 4.19, the relative permittivities of all undoped STO pellets are depicted. Here, a difference in the measured values due to different sintering atmosphere is readily apparent. While the oxidizingly sintered polycrystals show relative permittivities in the range of about 200, the reducingly sintered samples show values around 400 and 500. However, the lower fit quality found for reducingly sintered STO has also to be taken into account. At this point, it is also reasonable to compare the n values used to calculate these relative permittivities. As discussed in subsection 2.4.1, this value depicts the non-ideality of the constant phase element, and thus, the deviation from an ideal capacitor. n values in the range of 1.00 to 0.88 were determined, with all samples showing decreasing n values with increasing temperatures and the oxidizingly sintered STO samples showing generally slightly higher n values (n= 1 - 0.89) than the reducingly sintered samples (n = 0.98 - 0.88). In the measured temperature range, the relative permittivity of the oxidizingly sintered pellets seems to slowly increase with increasing temperature. Meanwhile, no clear temperature dependency can be determined for the relative permittivities of the reducingly sintered samples. Lastly, also no dependency of the relative permittivity on the nonstoichiometry can be found.

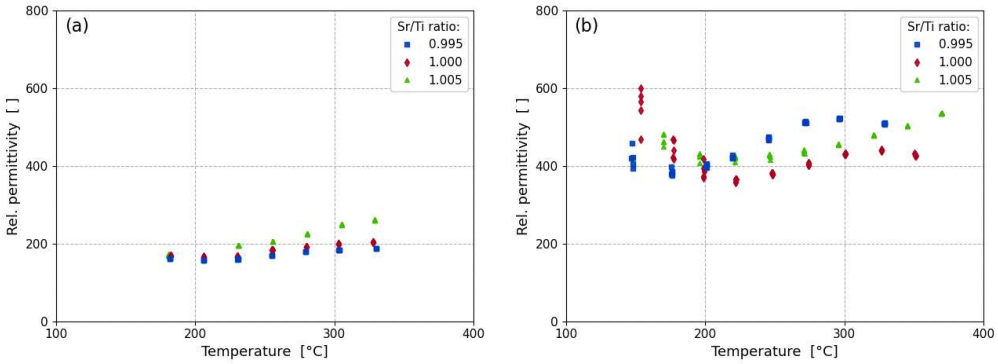

Figure 4.19: Temperature dependency of the relative permittivity of (a) oxidizingly and (b) reducingly sintered undoped STO pellets after equilibration at 700 °C

In Figure 4.20, the relative permittivities of all Fe-doped samples are plotted against the temperature. Similar to the undoped samples, a difference between the oxidizingly and reducingly sintered polycrystals is again visible. Hence, the oxidizingly sintered Fe:STO samples show a decrease of the relative permittivity with raising temperature from values slightly below 300 at lower temperatures to values around 200 at higher temperatures. This trend is shared by all Sr-deficient samples, with only the stoichiometric samples showing lower relative permittivity values and a smaller decline with rising temperatures.

For these oxidizingly sinterd samples, n is in the range of 0.98 to 0.90. However, no decrease with increasing temperatures was observed. The n values of the reducingly sintered samples declined for almost all samples from 0.95 to 0.82 with increasing temperatures. Only the n value of the stoichiometric sample remained at about 0.95, while the n values of the sample with a Sr/(Ti+Fe) ratio of 0.980 (i.e. the sample which got cracks during equilibration) decreased less intense with increasing temperatures.

The individual reducingly sintered Fe:STO samples show the largest differences in their relative permittivities of all sample types. Similar to the conductivity properties, the stoichiometric sample shows relative permittivities strongly deviating from the Sr-deficient samples, with values rather comparable to the stoichiometric oxidizingly sintered sample. Most of the understoichiometric samples show an increase in the relative permittivity with raising temperatures starting from about 250 °C upwards. Only the sample with a Sr/(Ti+Fe) ratio of 0.980 obtains a decreasing relative permittivity with raising temperatures. Hence, while at lower temperatures similar relative permittivity values like the rest of the reducingly sintered samples can be detected, at high temperatures a strongly pronounced difference could be measured. Furthermore, the sample with a Sr/(Ti+Fe) ratio of 0.985 shows significantly higher relative permittivities than the rest of the sample.

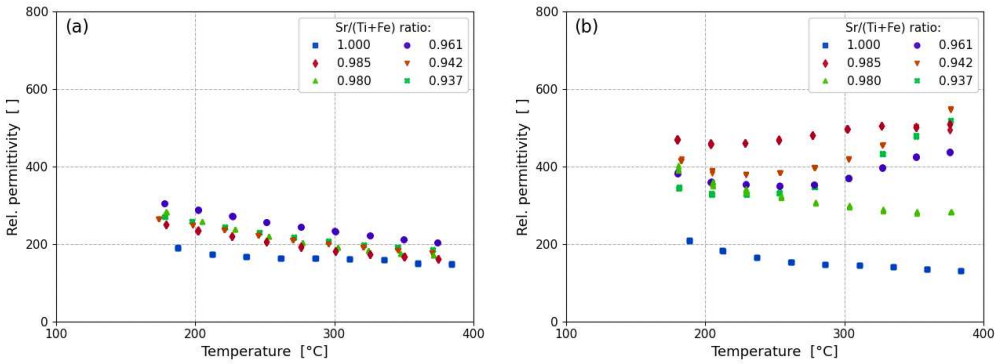

Figure 4.20: Temperature dependency of the relative permittivity of (a) oxidizingly and (b) reducingly sintered Fe:STO pellets after equilibration at 700 °C

4.3 Impedance spectroscopy of single crystal samples

In Figure 4.21, the impedance spectroscopy results of different single crystal samples between 200 °C_{set} and 400 °C_{set} are outlined. By comparing the values of both diagrams to each other, it is clearly visible that the Fe-doping increases the conductivity. Thus, all samples doped with Fe show about an order of magnitude higher conductivities than the undoped samples. Furthermore, the samples doped with 0.16 % Fe also demonstrate a slightly higher conductivity than the samples doped with 0.016 % Fe.

In contrast to polycrystalline STO, the conductivity of all samples hardly increases through the additional sintering steps. The lack of an effect here could be explained by less Sr-vacancy formation via the partial Schottky equilibrium compared to the polycrystalline specimen. An enhanced cation diffusion coefficient at grain boundaries was previously reported for other perovskite materials [107]. Most probably the same is true for STO, which could accelerate the formation of Sr vacancies. However, in a polycrystal SrO may also form at grain boundaries, thus reducing diffusion lengths required for Sr vacancy formation. Therefore, much longer sintering times would have been needed to cause a measurable effect of Schottky defect formation in the single crystals.

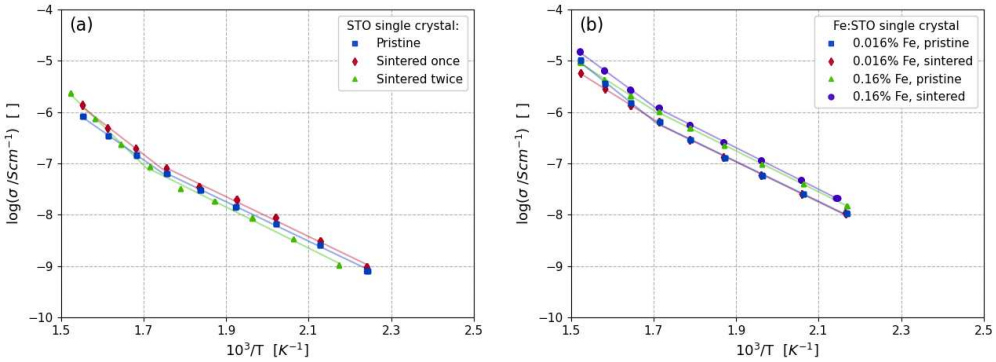

Figure 4.21: Effect of the sintering process at 1500 °C in air on the conductivity of STO and Fe:STO single crystals after equilibration at 700 °C: (a) Arrhenius plot of STO single crystals with different sintering history; (b) Arrhenius plot of Fe:STO single crystals with different sintering history

Figure 4.22 (a) and Figure 4.22 (b) depict the results of the impedance measurements of the STO and Fe:STO single crystals in comparison to the grain conductivities of the respective polycrystalline pellets. In both cases, the single crystals show smaller conductivities than the oxidizingly sintered polycrystalline samples. For undoped STO this is in accordance with the model of strongly enhanced Sr vacancy concentrations in polycrystals due to a partial Schottky disorder established during sintering. At higher temperatures, a similar conductivity of the STO single crystal in comparison to the stoichiometric reducingly sintered samples could be determined. Since these samples showed differences in the temperature dependency of the conductivity, the conductivity values of this sample was at lower temperatures even below the values of the reducingly sintered pellets. Meanwhile, the Fe-doped samples showed conductivities in between of the reducingly and oxidizingly sintered pellets. In the case of Fe-doped samples, it is also important to note that the Fe-content differs drastically between the single crystalline and polycrystalline samples.

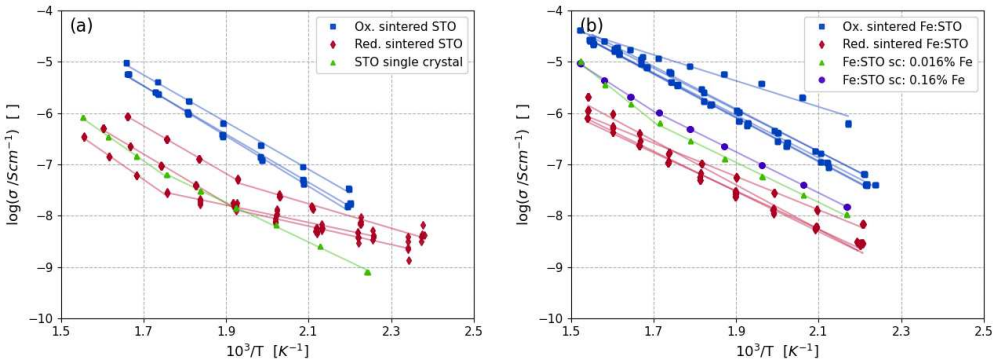

Figure 4.22: Comparison of the single crystalline samples with the polycrystalline samples: (a) Arrhenius plot of a STO single crystals and polycrystalline STO pellets, equilibrated at 700 °C; (b) Arrhenius plot of a Fe:STO single crystals and polycrystalline STO pellets, equilibrated at 700 °C

Since the Arrhenius plots of these samples showed a small kink at about 250 to 300 °C, additional measurements of STO single crystals were conducted to investigate this kink further. One of these measurements is depicted in Figure 4.23 (a). The temperature cycle started normally at 200 °C_{set}, but after reaching 400 °C_{set} the temperature got reduced again in 25 °C steps down to 200 °C_{set}. Afterwards, this whole temperature cycle was repeated. For the first couple measurements until 285 °C (300 °C_{set}) an activation energy of about 0.71 eV can be determined. Afterwards, a drastically change in the slope leads to an activation energy of about 1.62 eV. For all following up- and down-cycles the upper temperature activation energy stays in the range of 1.59 eV to 1.65 eV, while the lower temperature activation energy slowly rises, starting from 0.71 eV over 1.06 eV and 1.11 eV to 1.18 eV. This can be explained by a change in the conductivity mechanism at about 285 °C and a change of the lower activation energy through an equilibration effect.

A similar change in the activation energy (0.8 eV to 1.6 eV) was reported by Kubicek et al. [44]. However, in contrast to the results of this work, this change in the temperature dependency of the conductivity was reported for Fe-doped STO thin films at about 390 °C. 1.6 eV is about half the band gap of STO and for thin films the reason of the high activation energy seems to be related to a pseudointrinsic state [44]. Conductivities measured here are much higher and since the samples were equilibrated at 700 °C and quenched to room temperature prior to the measurements, a slow equilibration with the surrounding oxygen at these increased temperatures is plausible and might explain the measured drift. In an additional measurement the temperature was reduced again already after reaching 285 °C (Figure 4.23 (b)). Here, the activation energy changes only from 0.71 eV to 0.79 eV. The small change indicates that the equilibration process already started at such low temperatures.

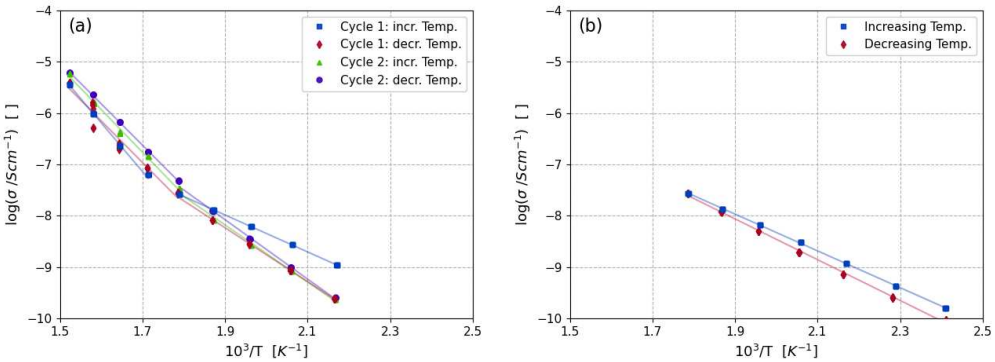

Figure 4.23: Arrhenius plot of STO single crystals equilibrated at 700 °C: (a) Cycling between 200 and 400 °C_{set}; (b) Cycling between 150 and 300 °C_{set}

Lastly, also the relative permittivies of the pristine single crystals can be compared to each other (Figure 4.24). For all these samples, the n values used to calculate the relative permittivities were relative high, in a range of 1.00 to 0.98. Independent of their doping content, all single crystals show relative permittivities of about 200 at low temperatures, as well as a slight decrease with increasing temperatures. Hence, this values are in the range of the relative permittivities of the oxidizingly sintered STO and Fe:STO samples.

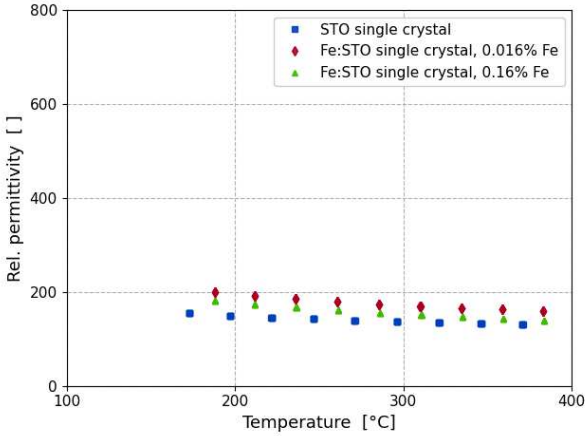

Figure 4.24: Temperature dependency of the relative permittivity of all single crystal samples after equilibration at 700 °C

4.4 Impedance spectroscopy of thin film samples

In comparison to the previously discussed polycrystalline and single crystal samples, the evaluation of the conductivies was found to be more difficult for the thin film samples. Between one and three RCPE elements were needed to fit the semicircular structure in the impedance spectra, which corresponds to the thin film. With varying temperature, it was often necessary to change the equivalent circuit used to fit an individual sample.

When the measurement temperature reached about 750 °C, a drop in the conductivity values could be determined (Figure 4.25 (a)), which prevailed till the end of the whole temperature cycle. After this drop, only conductivity values well below the calculated conductivity of intrinsic STO (gray line in Figure 4.25 (a)) and permittivity values in the single digit range could be determined. Since this effect was also measured on a plain Nb:STO single crystal (Figure 4.25 (b)), a change in the thin film properties can be ruled out as cause for this effect. Most probably the single crystal changes at higher temperatures and its conductivity becomes inhomogeneous. Then it is difficult to define a representative cunductivity. Hence, only the electrical conductance G is plotted in Figure 4.25 (b), which equals the reciprocal resistance of the single crystal. A possible explanation would be a cationic migration in the single crystal at higher temperatures, creating a thin non-conducting layer overshadowing the whole signal of the thin films. Nonetheless, it is unreasonable to analyze the whole temperature cycle, and thus, only the impedance spectroscopy results of the thin films obtained upon 750 °C$_{\text{set}}$ are discussed in this thesis.

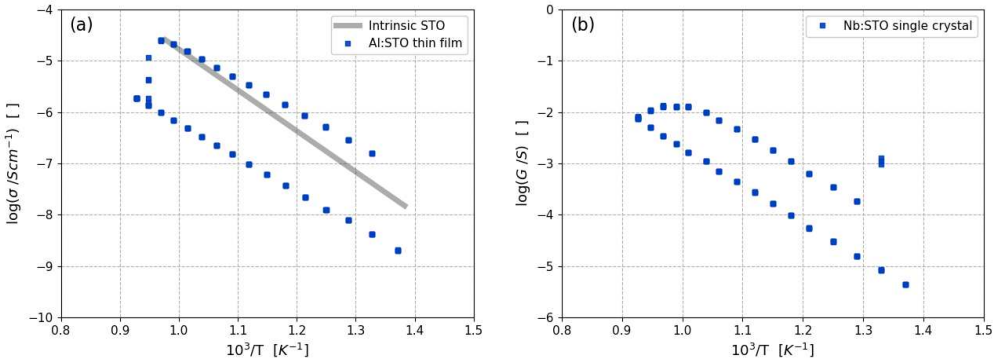

Figure 4.25: Depiction of the conductivity drop at higher temperatures: (a) Arrhenius plot of an Al-doped STO thin film on a Nb:STO single crystals compared to the calculated conductivity of intrinsic STO. The thin film has a theoretical Sr/(Ti+Al) ratio of 1.05 and an Al-content of 0.3 %; (b) electrical conductance of a plain Nb:STO single crystal;

The results of the impedance spectroscopy measurements of all Al-doped STO thin films are shown in Figure 4.26 compared to each other. It is readily apparent that all of the thin films only reach conductivity values in the range of the calculated intrinsic conductivity of STO, as it was previously observed for Fe-doped STO thin films [27, 44]. While for the understiochiometric and stiochiometric thin film samples intrinsic conductivities are determined, only the sample with a Sr/(Ti+Al) ratio of 1.05 and an Al-content of 0.3 % exceeds the intrinsic conductivity at lower temperatures. Interestingly, the thin film with the same theoretical Sr/(Ti+Al) ratio but a higher Al-content shows again a lower conductivity.

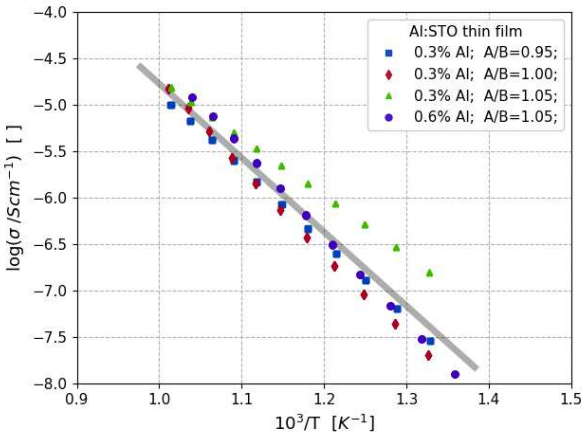

Figure 4.26: Arrhenius plot of Al-doped STO thin films on Nb:STO single crystals with varying cation nonstoichiometry and doping content; The gray line depicts the calculated intrinsic conductivity of STO

In the case of the Nb-doped STO thin films, a similar picture appears like for the Al:STO thin films. For most of the thin films only conductivities in the range of the intrinsic conductivity of STO could be determined (Figure 4.27). Only the sample with an A/B site ratio of 1.05 and a Nb-content of 0.3 % shows a higher conductivity. Here, the difference of this sample to the others is even more pronounced. Interestingly, of all Nb:STO thin films, this was the only thin film for which only one (200) reflection peak was found in the reciprocal space mapping. Furthermore, an additional conductivity drop is visible, appearing at about 550 to 600 °C. The cause of this conductivity drop is unknown. For the sample with the highest doping content of 0.6 % Nb and a Sr/(Ti+Nb) ratio of 1.05 the lowest conductivity values could be determined.

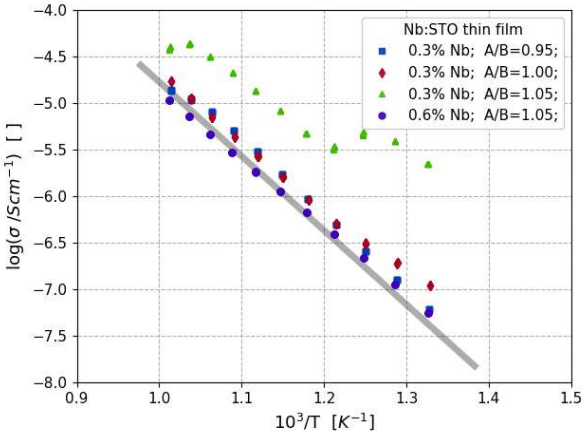

Figure 4.27: Arrhenius plot of Nb-doped STO thin films on Nb:STO single crystals with varying cation nonstoichiometry and doping content; The gray line depicts the calculated intrinsic conductivity of STO

The Fe-doped thin films with different Sr/(Ti+Fe) ratios are the only thin film samples, which show a severe change in the conductivity due to varying A/B ratios. In Figure 4.28 these results are summarized in comparison to the calculated intrinsic conductivity of STO. Additionally, also the conductivity of a Fe:STO pellet with 2 % Fe is shown, which was previously prepared and measured within the working group. While the thin film with an understiochiometric Sr-content shows a similar conductivity to intrinsic STO, the stoichiometric thin film already exceeds this by about one order of magnitude. The measurement of the thin film with an A/B ratio of 1.05 was already started at 250 $°C_{set}$, since at higher temperatures the extremely high conductivity could no longer be determined. Hence, the conductivity of this thin film is more comparable to the Fe:STO pellet and exceeds the other thin films in several orders of magnitude.

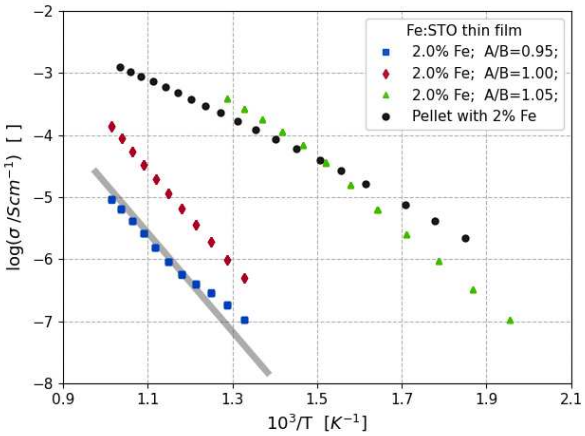

Figure 4.28: Arrhenius plot of Fe-doped STO thin films on Nb:STO single crystals with varying cation nonstoichiometry compared to the grain conductivity of a Fe:STO pellet with 2 % Fe; The gray line depicts the calculated intrinsic conductivity of STO

While the Sr/(Ti+Fe) ratio seems to strongly influence the conductivity of the Fe:STO thin films, the impact of the laser energy used during the sample preparation is rather small (Figure 4.29). Here, for all thin films only conductivities close to the intrinsic value could be determined. While the thin film prepared with 400 mJ laser energy demonstrates the lowest conductivity, the thin films with 300 and 270 mJ hardly show any difference in conductivity. Since all previously discussed thin films were always prepared with 400 mJ laser energy, the here discussed thin film prepared with 400 mJ only differs in a slightly longer ablation time from the aforementioned Fe:STO thin film with a Sr/(Ti+Fe) ratio of 1.00. However, these two sample differ strongly in their determined conductivities (Figure 4.30). This result originates probably due to the sample inhomogeneity, since different micro-electrodes at different positions on the sample were measured, making small deviations in the stoichiometry very likely. In Figure 4.30, an older Fe:STO thin film sample is also depicted, which was prepared by the working group when the PLD was still slightly differently set up. This thin film also shows conductivities very similar to the intrinsic value, like the sample with a slightly longer ablation time.

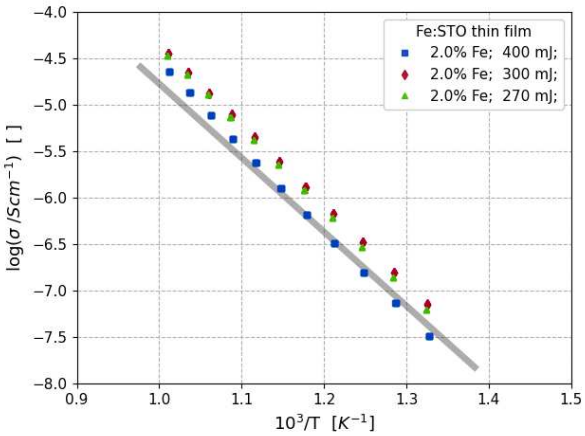

Figure 4.29: Arrhenius plot of Fe-doped STO thin films with A/B ratios of 1.00 on Nb:STO single crystals, which were prepared with varying laser energy; The gray line depicts the calculated intrinsic conductivity of STO

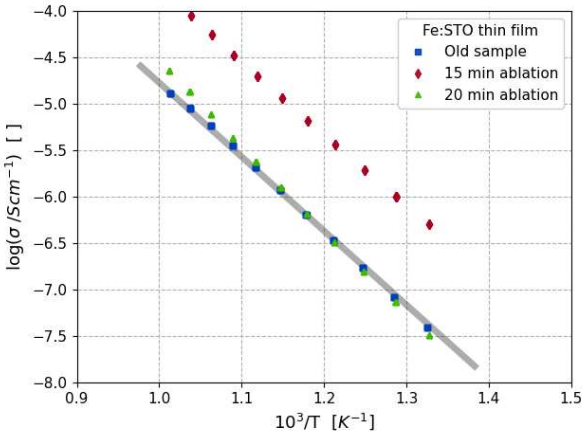

Figure 4.30: Arrhenius plot of 2 % Fe-doped STO thin films with A/B ratios of 1.00 on Nb:STO single crystals with equal laser energy during sample preparation; The gray line depicts the calculated intrinsic conductivity of STO

4.5 Voltage measurements under UV light irradiation

In addition to the aforementioned impedance measurements, the evaluation of the effect of UV irradiation on the samples is a major focus of this thesis. Since the results of the conducted voltage measurements differed strongly between the samples with a polycrystalline and a single crystalline STO phase, it is reasonable to split this chapter into two subsections. In addition, the effect of the current collector design is discussed in a third subsection.

Most samples for light illumination measurements consisted of a STO polycrystal with photolithographically prepared grid-like current collectors on top and brushed Pt counter electrodes. To investigate the impact of different decoration layers, four different sample designs were prepared, which are depicted in Figure 4.31. In addition to these different sample designs, the individual samples differed in the sintering atmosphere and Sr/Ti ratios of the STO polycrystals used. Hence, STO pellets sintered either in oxidizing and reducing atmosphere with Sr/Ti ratios of 0.95, 1.00, and 1.05 were investigated. The results of these samples are discussed in subsection 4.5.1.

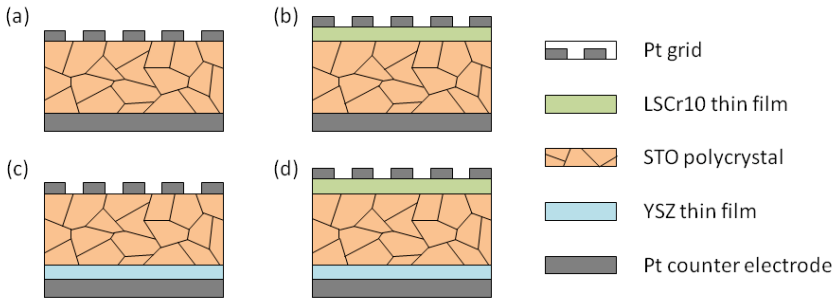

Figure 4.31: Scheme of the four sample designs used for polycrystalline STO samples: STO pellets (a) without decoration layers, (b) with a LSCr10 top decoration layer, (c) with a YSZ bottom decoration layer, and (d) with both types of decoration layers

For the samples with single crystalline STO, only the top decoration layer was varied. Hence, like depicted in Figure 4.32, all samples had YSZ thin films as bottom decoration layers and either LSCr0, LSCr10, or LSCr20 thin films as top decoration layer. The results of the voltage measurements upon UV light illumination of the single crystalline samples are discussed in subsection 4.5.2.

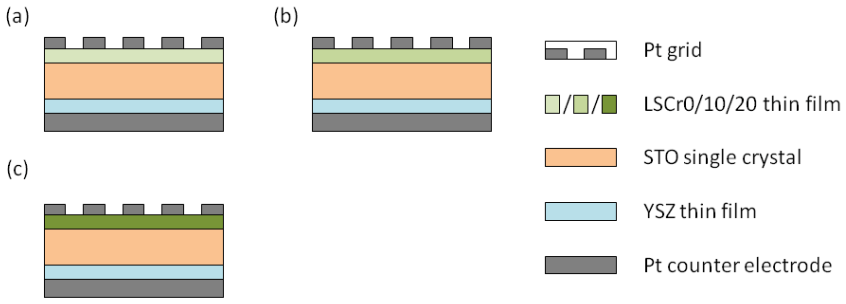

Figure 4.32: Scheme of the sample designs used for single crystalline STO samples: STO single crystals with YSZ bottom decoration layers and (a) LSCr0, (b) LSCr10, or (c) LSCr20 top decoration layers

While all previously shown sample designs hat Pt grid-like electrodes prepared via the photolithographic route as current collectors, also other current collector designs were prepared, as discussed in section 3.5. Hence, Pt and Au grid-like electrodes prepared via a shadow mask as well as 10 nm thick Au layers were also investigated as current collectors (Figure 4.33). The STO polycrystals used for these samples were prepared via a simplified preparation route (see section 3.4). The voltage measurements under light illumination of these samples are discussed in subsection 4.5.3.

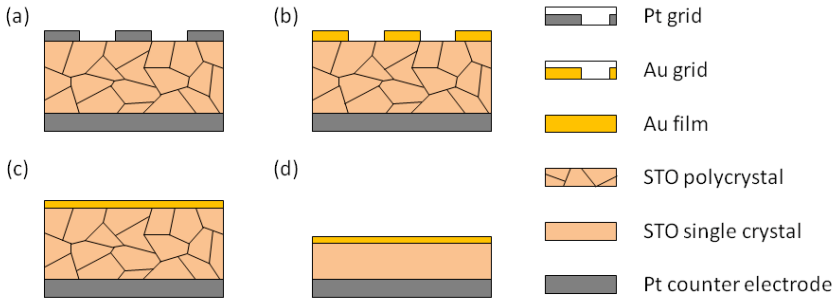

Figure 4.33: Scheme of the samples with deviating current collector designs: STO pellets with (a) Pt or (b) Au grid-like electrodes prepared via a shadow mask and (c) polycrystalline and (d) single crystalline STO with 10 nm thick Au layers

4.5.1 Polycrystalline samples

In Figure 4.34, the time-resolved voltage measurements of three different samples prepared from oxidizingly sintered STO pellets are outlined. These samples had the sample design depicted in Figure 4.31 (a), and thus, did not have any decoration layers. The general shape of this curves created by the UV irradiation resembles the model explained in subsection 2.2.2, according to Walch et al. Before the illumination of the samples started, a small voltage offset is visible. This voltage difference between both sides of the samples reaches a relatively stable value during equilibration and reflects the dark voltage U_{Dark} from Walch et al., even though the values are much smaller here. When turning on the UV light, a clearly visible jump of the measured voltage to more negative values evokes due to the UV illumination. This negative peak is followed by a steep voltage increase, which slowly starts to level off during the UV irradiation. After turning off the UV light, a positive voltage peak appears, after which the measured voltages slowly return to the dark voltage values. The first negative peak and the positive peak after turning the UV light off indicate a negative photovoltage and a positive battery voltage. This behavior matches with the results of Walch et al. [5], even though no ionic conducting YSZ layer was used here at the bottom side. Walch et al. explained the battery voltage by a chemical change due to oxygen incorporation upon light (see subsection 2.2.2). Possibly this oxygen incorporation does not affect the entire polycrystal in the short time scale used here (15 min) due to grain boundaries, see below. Thus, the still unaffected STO part may act as the ion conductor required to measure a battery voltage.

The overall characteristic of this curve remains the same for all samples with STO pellets, independent of their layer design. Only the corresponding battery voltages $U_{Batt,Max}$ after 15 min, photovoltages $U_{PV,Max}$, as well as the flattening behavior of the voltage curve during UV illumination differ depending on the sample characteristics. These differences in the battery voltages and photovoltages are discussed below.

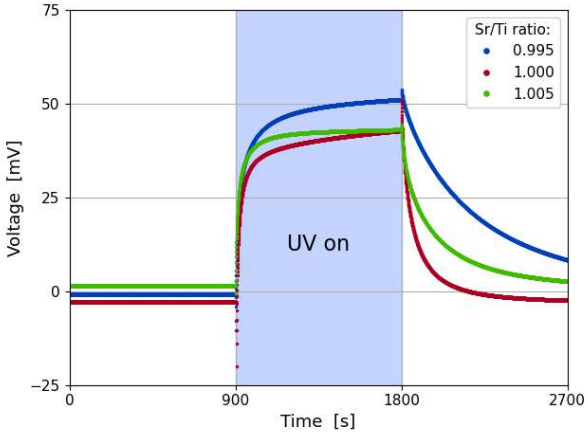

Figure 4.34: Voltage measurement of three polycrystalline STO samples with varying cation nonstoichiometry with and without UV irradiation at 345 °C in air

The previously shown measurements all had an illumination time of exactly 15 min to ensure the comparability between the individual samples. For achieving a better understanding of the battery voltage and how it changes over time, an additional long time experiment with varying illumination times was conducted. The sample investigated was a STO polycrystal with a Sr/Ti ratio of 0.995 and with a LSCr10 top decoration layer (i.e. the sample design shown in Figure 4.31 (b)). The whole measured voltage curve of this experiment is shown in Figure 4.35 (a). The normalized battery voltages, which emerged after each illumination step, could be determined by calculating the difference between the voltage right before turning the UV light on and the maximum voltage, which was reached after turning the UV light off. Since a small drift to a more negative dark voltage seems to appear, slightly too small battery voltages were probably obtained for the longest illumination times. The calculated $U_{Batt,Max}$ values are plotted in Figure 4.35 (b) against the individual irradiation time. It is readily apparent that the battery voltage increases with longer UV irradiation. The flattening of the slope appearing between the last two data points (3 h and 8 h illumination time) could be explained by the system slowly reaching its equilibrium state. Overall, a similar relationship between the battery voltage and the illumination time was found with STO single crystals by Walch et al. [5]. Nonetheless, the maximum irradiation times applied by Walch et al. were less than 30 min long, with relative constant $U_{Batt,Max}$ values after about less than 5 min. This results indicate a faster charging process in the single crystalline STO compared to the polycrystalline material used here. According to Walch et al. the UV light leads to a change of the oxygen stoichiometry in the crystal, and thus, oxygen diffusion in the STO strongly affects the time dependency. This diffusion is strongly retarded by grain boundaries in STO [108]. Furthermore, the LSCr10 layer of the measured sample most likely also shows an effect on the charging duration.

Please note: In most measurements with LSCr layers on STO single crystals, the battery voltage was negative (see also below in subsection 4.5.2). This sign change indicates a difference in terms of oxygen vacancy change upon light. Either oxygen vacancies are annihilated (positive voltage) or their concentration is increased (negative voltage). The different behavior of single crystal and polycrystal might be a consequence of the different cation defect concentrations, see first part of this thesis.

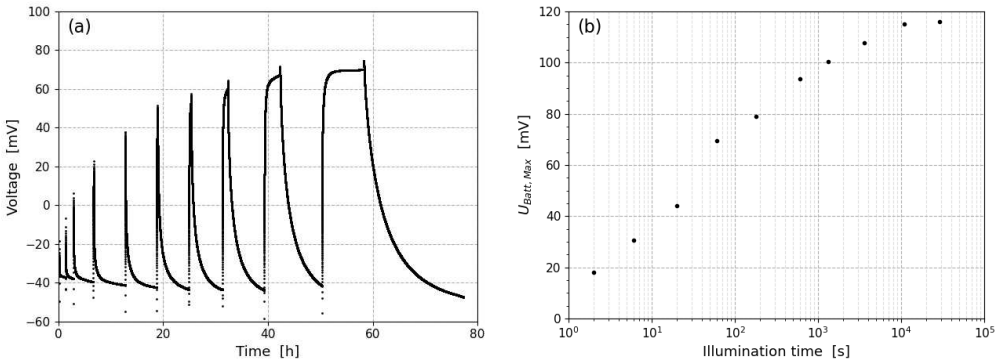

Figure 4.35: Long time voltage measurement with different UV irradiation times at 345 °C in air: (a) Overview over the whole voltage measurement; (b) Determined $U_{Batt,Max}$ values plotted against the UV illumination time; The analyzed sample consisted of a LSCr10 layer and an oxidizingly sintered STO pellet with Sr-deficiency

To simplify the comparison of the effect of light illumination on different samples, the battery voltages after 15 min and photovoltages compared in the following were normalized to the respective dark voltage measured before. Thus, the battery voltages after 15 min UV illumination of all samples with oxidizingly sintered STO pellets are outlined in Figure 4.36 (a). While it is harder to identify a correlation between the battery voltage and the Sr/Ti ratio, it is recognizable that the samples with LSCr10 layers show generally higher battery voltages. Thus, the top decoration layer seems to increase $U_{Batt,Max}$. The YSZ layers added on the bottom of the samples should function as an electrolyte, which is theoretically necessary for the existence of a battery voltage. Therefore, a big effect on the battery voltage through the addition of YSZ layers is expected. However, the addition of YSZ layers seems to hardly have any effect on the battery voltage, which could be explained by the STO itself functioning as an electrolyte.

The measured photovoltages $U_{PV,Max}$ are shown in Figure 4.36 (b). Here, it is visible that the LSCr10 layers also show a positive effect on the photovoltages. Furthermore, the sample with YSZ layers and LSCr10 layers show higher $U_{PV,Max}$ values than the samples with only LSCr10 layers. This is not fully understood yet, since the photovoltage was expected to only be affected by changes close to the material-current-collector-interface. However, since the LSCr10 layer was prepared before the YSZ layer, it was exposed a larger heat during the ablation of the YSZ layer due to it being directly on the heated sample holder. This could have affected the thin film. Hence, this behavior was also not measured for the samples without LSCr10 layers.

In contrast to the battery voltage, the measured photovoltages seem to also depend on the Sr/Ti ratio of the bulk phase, whereas a stoichiometric sample composition leads to the highest measured photovoltages. Overall, all measured values lay in a comparable range to the battery and photovoltages of the single crystalline samples with a YSZ layer of Walch et al. measured at 360 °C in air [5].

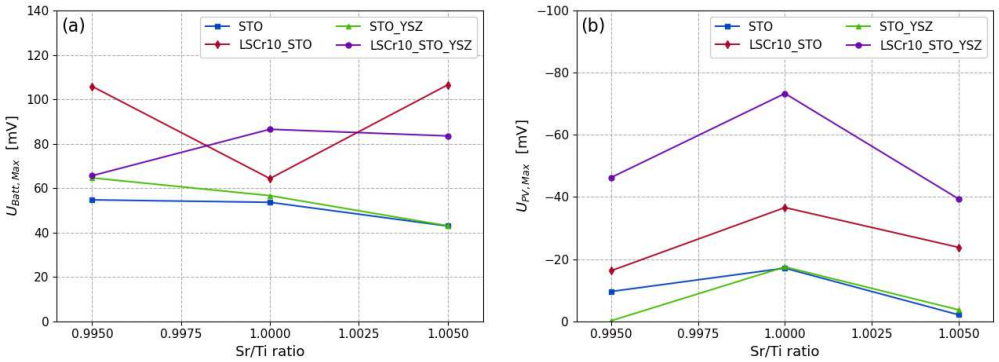

Figure 4.36: Comparison of the voltage measurements under UV light of the oxidizingly sintered STO pellets: (a) Determined $U_{Batt,Max}$ values after 15 min UV irradiation; (b) Measured $U_{PV,Max}$ peaks at the start of the UV irradiation

To investigate the effect of the sintering conditions of the STO pellet on the behavior under UV illumination, the measured battery voltages and photovoltages of the respective samples are compared in Figure 4.37. Next to the decoration layer-free STO pellets also samples with a LSCr10 top decoration layer were examined (i.e. the sample designs in Figure 4.31 (a) and (b)). The reducingly sintered samples show significantly smaller battery voltages than the oxidizingly sintered samples after the 15 min UV irradiation. According to Merkle et al. an increased oxygen incorporation in STO under UV light can be traced back to the fact that the UV induced electron-hole generation has a bigger effect on the lower electron concentration than the hole concentration [10]. The lower conductivity of reducingly sintered STO pellets discussed in section 4.2 could result from a lower hole concentration, which could further on explain the lower battery voltages measured for these samples. Furthermore, neither a clear effect of the LSCr10 layer nor of the Sr/Ti ratio on the battery voltage of these samples was detectable. Interestingly, the measured photovoltages do not only tend to be slightly smaller compared to the respective sample with an oxidizingly sintered pellet, they also show a different correlation to the cation nonstoichiometry than the oxidizingly sintered samples. Lastly, the LSCr10 layer seems to improve the photovoltage of the samples with reducingly sintered STO pellets similarly to the samples with oxidizingly sintered pellets.

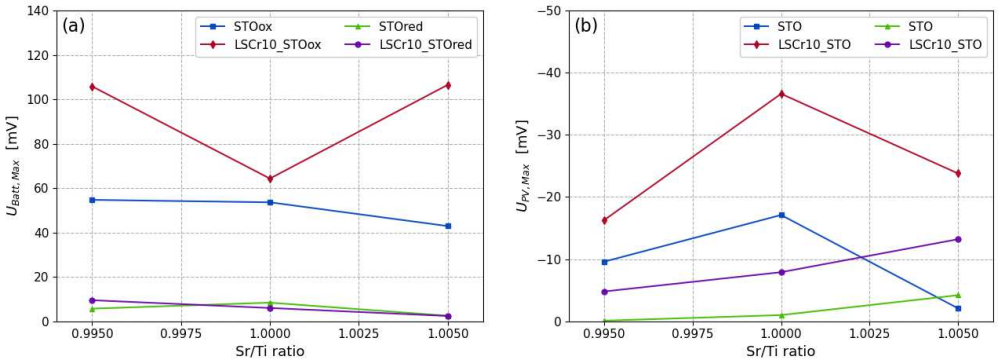

Figure 4.37: Comparison of the voltage measurements under UV light of samples with different sintering history: (a) Determined $U_{Batt,Max}$ values after 15 min UV irradiation; (b) Measured $U_{PV,Max}$ peaks at the start of the UV irradiation

To investigate the possible effect of the STO itself functioning as an electrolyte further, the samples consisting of oxidizingly sintered STO pellets and LSCr10 layers (i.e. the sample design illustrated in Figure 4.31 (b)) were thinned down to about half their thickness. After adding new porous counter electrodes, these samples were measured again and were compared to their thicker counterparts. The determined battery voltages and photovoltages of these samples are depicted in Figure 4.38. Interestingly, both voltages increase for all samples when the corresponding STO pellets are thinner. While according to Merkle et al. only the first 100 nm of the STO are illuminated [10], no UV absorption should take place in the lower part of the sample. Still, the thickness could affect the measured voltages, for instance, by changing the resistance for different charge carriers to reach the bottom electrode and therefore the electrolyte effect, or changing the volume which gets charged and with this also the charging rate.

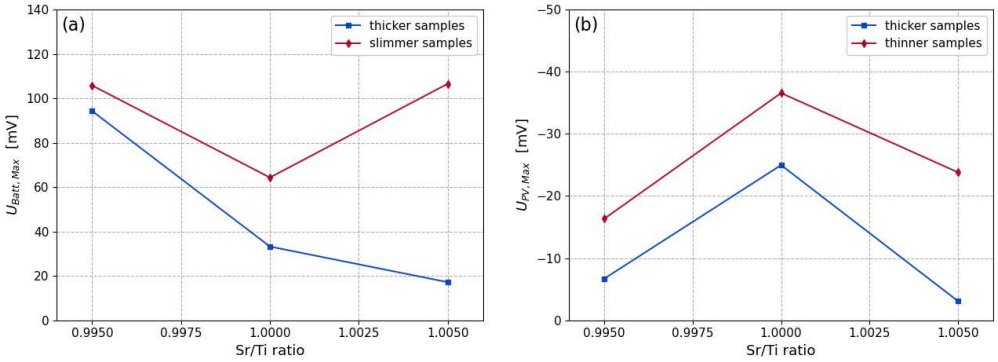

Figure 4.38: Comparison of the voltage measurements under UV light of samples with equal layer structure (STO pellet with LSCr10 top decoration layer) but different thickness of the STO pellets: (a) Determined $U_{Batt,Max}$ values after 15 min UV irradiation; (b) Measured $U_{PV,Max}$ peaks at the start of the UV irradiation

4.5.2 Single crystal samples

In Figure 4.39, voltage measurements under UV light irradiation of different single crystal samples are outlined. All three samples had a YSZ bottom decoration layer but varying LSCr top decoration layers (like previously shown in Figure 4.32). The general characteristics of these voltage curves already differ from the ones obtained with polycrystalline samples. Hence, measurements conducted at single crystalline samples were the only light illumination measurements for which negative battery voltages could be measured. Only the sample with a LSCr10 layer on top still shows a positive battery voltage. Despite this different behavior of their battery voltages, all these sample have huge photovoltages, being in the range of 800 mV. Thus, these photovoltages are even comparable to the 920 mV measured by Brunauer et al. at 400 °C with a LSCr20 / STO junction [4]. The highest photovoltages measured with a Pt current collector by Walch et al. lay only at about 150 mV, but these samples also had no top decoration layers [5]. Therefore, the combination of a STO single crystal and a LSCr top decoration layer seems to be the decisive factor for these high photovoltages. The crystallinity of the STO phase might affect this due to a possible negative effect of grain boundaries or through changes in the surface morphologies. Meanwhile, no real correlation between the Sr-content in the LSCr layer and the measured voltages could be detected. The voltage curve during illumination diverged for the sample with LSCr0 layer and, as mentioned before, only the sample with a LSCr10 layer shows a positive battery voltage.

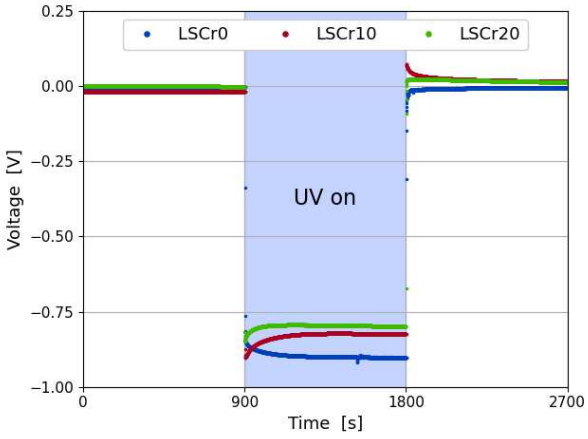

Figure 4.39: Voltage measurement of STO single crystals with LSCr0, LSCr10 and LSCr20 top decoration layers and YSZ bottom decoration layers with and without UV irradiation at 345 °C in air

Since only the single crystal sample with a LSCr10 top decoration layer shows a positive battery voltage, it is only reasonable to compare this sample to polycrystalline samples with an equal layer structure (i.e. the samples with the sample design shown in Figure 4.31 (d)). Thus, the battery voltages and the photovoltages of different samples with LSCr10 top decoration layers and YSZ bottom decoration layers are depicted in Figure 4.40. By comparing the $U_{PV,Max}$ values (Figure 4.40 (b)) it is readily apparent that switching to a single crystalline STO phase has an immense effect on the photovoltages. Interestingly, even though their big difference in the photovoltages, all these samples show relatively comparable battery voltages, with the $U_{Batt,Max}$ value of the single crystal sample being slightly higher than for the polycrystalline samples.

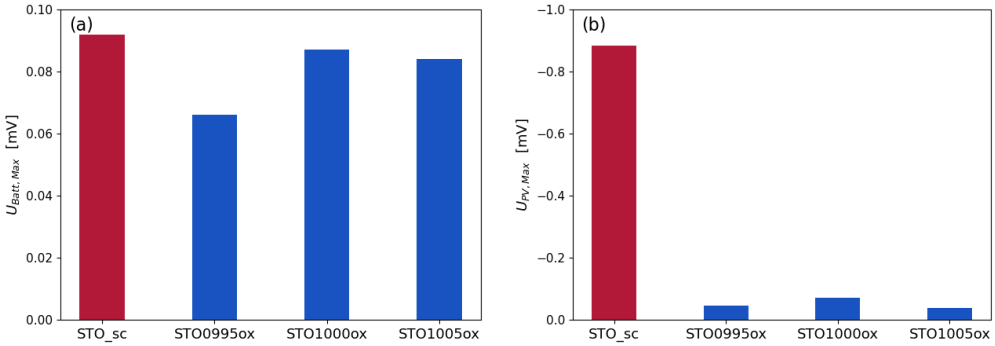

Figure 4.40: Comparison of the voltage measurements under UV light of STO single crystals and STO pellets with LSCr10 top decoration layers and YSZ bottom decoration layers: (a) Determined $U_{Batt,Max}$ values after 15 min UV irradiation; (b) Measured $U_{PV,Max}$ peaks at the start of the UV irradiation

4.5.3 Variations of the current collectors

Like discussed in subsection 4.1.3, the lithographic preparation of Pt grids proved to be a long many-step-process, which often did not result in a satisfactory outcome. This was even worse for the samples prepared with STO powder as starting material. Therefore, grid-like electrodes prepared via a shadow mask were used for these samples. While current collectors made of different materials were prepared with this route, at first, a comparison between these grid-like electrodes and those prepared via photolithography shall be made. Figure 4.41 depicts the battery voltages and photovoltages of samples prepared from STO powder with Pt current collectors prepared via the shadow mask and samples prepared from $SrCO_3$ and TiO_2 powders with lithographically prepared Pt current collectors in comparison to each other. While the simplified preparation route does not change the overall behavior of the samples under UV light, smaller battery voltages and higher photovoltages were gained.

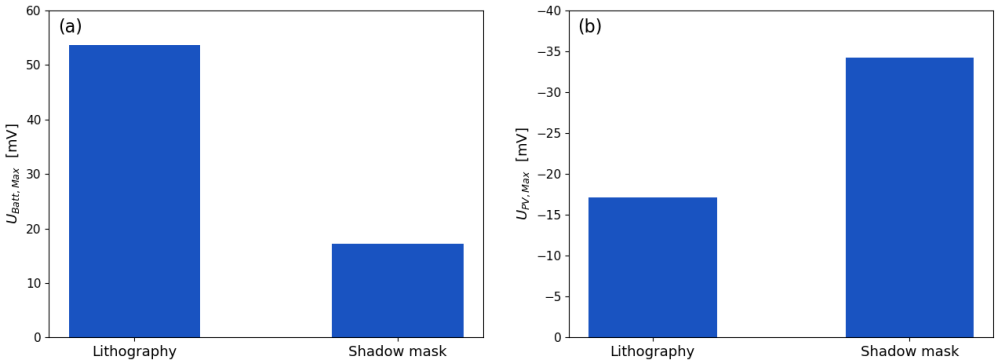

Figure 4.41: Comparison of the Pt grid-like current collector structures added via photolithography and shadow mask: (a) Determined $U_{Batt,Max}$ and (b) measured $U_{PV,Max}$ of STO samples with differently added current collectors

To determine the effect further variations of the current collectors have on the battery voltage and the photovoltage of the STO pellets, additional light illumination measurements were conducted. The samples used for this were again STO pellets prepared from STO powder. Next to the platinum grids prepared via the shadow mask also similarly prepared gold grids and dense Au layer of 10 nm thickness were investigated. The dense Au layers were added by sputtering Au for 10 s onto the samples. This layers should be thin enough to allow a sufficient part of the light getting through but still provide a good conductivity. Additionally, this film serves as a barrier for the incorporation or release of oxygen. The conducted measurements are summarized in Figure 4.42. Au grids seem to increase the battery voltage as well as photovoltage compared to the Pt grids. As comparison, Walch et al. found only an increase in the photovoltage with a switch to Au current collectors, but no change in the battery voltages [5]. Meanwhile, the dense Au films yield higher $U_{Batt,Max}$ but lower $U_{PV,Max}$ than the Au grids.

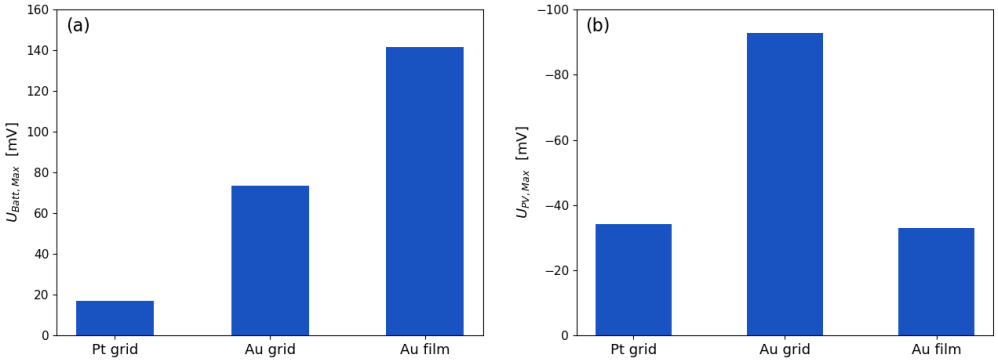

Figure 4.42: Effect of different current collector structures on $U_{Batt,Max}$ and $U_{PV,Max}$: (a) Determined $U_{Batt,Max}$ of STO pellets with different current collectors; (b) Measured $U_{PV,Max}$ of STO pellets with different current collectors

For further comparison also a STO single crystal was prepared with a dense Au layer as current collector. Like depicted in Figure 4.43, the measurements of these two samples are hardly comparable, since the polycrystal has a small photovoltage and a positive battery voltage, while the single crystal shows a huge photovoltage and a negative battery voltage. Hence, the single crystal sample with a dense Au layer shows a more similar voltage curve to the single crystal samples with LSCr layers and Pt grids, proving further the big difference between samples with a polycrystal and a single crystal STO phase. Interestingly, with a photovoltage of about 1 V this rather simply build up sample provided the largest photovoltage measured in the course of this thesis.

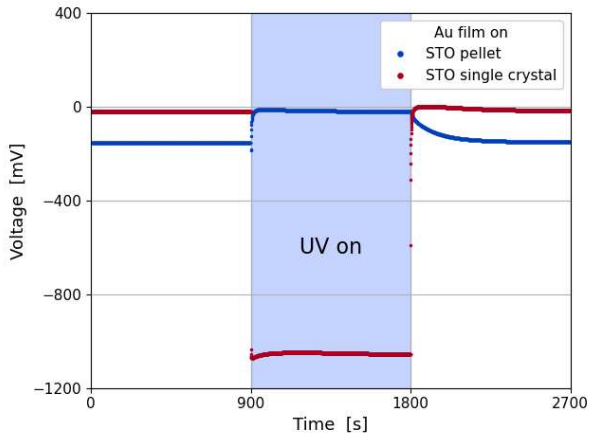

Figure 4.43: Voltage measurement of a polycrystalline and a single crystalline STO sample with 10 nm Au films on top with and without UV irradiation at 345 °C in air

5 Conclusion

Over the course of this thesis, several types of STO based samples were prepared and studied via different experiments. With the aim of achieving a better understanding of the defect chemistry of STO as well as its behavior under light illumination, electrochemical impedance spectroscopy (EIS) and time-resolved voltage measurements with and without UV irradiation were conducted.

In the temperature range from 180 to 360 °C, oxidizingly sintered polycrystalline STO showed a relative high grain conductivity compared to STO single crystals. This originates probably from a larger number of Sr vacancies in the polycrystals. Hence, more Sr-depleted polycrystals also obtained slightly higher grain conductivities regardless of whether the Sr-deficiency was intentionally prepared or caused during the sintering via the partial Schottky reaction. The determined activation energies indicated either a p-type conductivity or an ionic charge transport via oxygen vacancies. In addition to these results, the impact of atmosphere during sintering on the final grain conductivity has been shown. After the equilibration process, STO sintered under reducing conditions showed significantly lower grain conductivities than the same material sintered under oxidizing atmosphere. Furthermore, a change of the predominant conduction mechanism to a still unidentified mechanism at lower temperatures could be detected.

Among the Fe-doped STO samples, the highest grain conductivity in the temperature range from 180 to 360 °C was measured for stoichiometric Fe:STO. All Sr-deficient samples showed very similar grain conductivities. Very little difference was found between understoichiometric Fe:STO and undoped polycrystalline STO. The difference was more pronounced for the materials being equilibrated with their surroundings at 700 °C. Lastly, the effect of the sintering atmosphere proved to be similar to undoped STO. Sintering in reducing atmosphere leads to generally lower conductivities after equilibration, while no pronounced change in the conduction mechanism was found.

For the EIS measurements of the single crystals, a more distinct difference between undoped and Fe-doped STO could be detected. Hence, the determined conductivities increased with increasing Fe-content. A lower amount of Sr vacancies in the undoped STO single crystal resulted in a lower conductivity compared to the polycrystals. An additional heat treatment in accordance to the sintering of the oxidizingly sintered samples did not increase the conductivity. This is most probably due to less Sr vacancy formation caused by a lower cation diffusion coefficient in the STO grain compared to the grain boundary [107].

Independent of their doping content, most of the analyzed thin films showed conductivities in the range of the calculated intrinsic conductivity of undoped STO. Higher conductivities were mostly determined for thin films with a higher theoretical Sr/(Ti+doping) ratio. Of all Nb:STO thin films, the thin film with a theoretical Sr-excess was also the only one not indicating the presence of cationic defects due to an enlarged lattice constant. Thus, the presence of a cationic defect seems to decrease the conductivity of most doped thin films to the intrinsic value. Apparently, an increased Sr-content in the target seems to counteract this behavior.

By analyzing the time-resolved voltage measurements with and without UV irradiation, two different types of voltages were found to emerge in the samples upon UV illumination. These voltages were the photovoltage U_{PV} and the battery voltage U_{Batt}, which were previously described by Walch et al. Furthermore, the time depended increase of the battery voltage could be measured and different parameters changing both voltages were determined. Here, the largest impact on the behavior upon UV light seemed to be caused by the crystallinity of the STO phase in the samples. Hence, in the case of single crystalline STO, huge photovoltages, comparable to the 920 mV measured by Brunauer et al., and mostly negative battery voltages could be measured. In comparison, for all specimen with polycrystalline STO, significantly smaller photovoltages, but also positive battery voltages could be determined. The voltages measured with these samples were rather comparable to the photovoltages and battery voltages measured by Walch et al. The difference between these two sample types might originate from different surface morphologies or because of the grain boundaries of the polycrystalline STO. While the addition of LSCr layers onto polycrystalline STO pellets seemed to mostly increase both voltages, no significant effect was found when using YSZ as bottom decoration layer. Finally, no dependency of the battery voltage on the Sr/Ti ratio was found, while the photovoltage seemed to be affected by it.

Bibliography

[1] BP. *bp Statistical Review of World Energy 2020*. 2020.

[2] Q. M. Nguyen. "Solid oxide fuel cell technology - features and applications". In: *Solid State Ionics* 174.1-4 (2004), pp. 271–277. DOI: 10.1016/j.ssi.2004.07.042.

[3] J. Pirkandi, M. Ghassemi, M. H. Hamedi, and R. Mohammadi. "Electrochemical and thermodynamic modeling of a CHP system using tubular solid oxide fuel cell (SOFC-CHP)". In: *Journal of Cleaner Production* 29-30 (2012), pp. 151–162. DOI: 10.1016/j.jclepro.2012.01.038.

[4] G. C. Brunauer, B. Rotter, G. Walch, E. Esmaeili, A. K. Opitz, K. Ponweiser, J. Summhammer, and J. Fleig. "UV-Light-Driven Oxygen Pumping in a High-Temperature Solid Oxide Photoelectrochemical Cell". In: *Advanced Functional Materials* 26.1 (2015), pp. 120–128. DOI: 10.1002/adfm.201503597.

[5] G. Walch, B. Rotter, G. C. Brunauer, E. Esmaeili, A. K. Opitz, M. Kubicek, J. Summhammer, K. Ponweiser, and J. Fleig. "A solid oxide photoelectrochemical cell with UV light-driven oxygen storage in mixed conducting electrodes". In: *Journal of Materials Chemistry A* 5.4 (2017), pp. 1637–1649. DOI: 10.1039/c6ta08110j.

[6] A. S. Bhalla, R. Guo, and R. Roy. "The perovskite structure - a review of its role in ceramic science and technology". In: *Materials Research Innovations* 4.1 (2000), pp. 3–26. DOI: 10.1007/s100190000062.

[7] H. Anderson. "Review of p-type doped perovskite materials for SOFC and other applications". In: *Solid State Ionics* 52.1-3 (1992), pp. 33–41. DOI: 10.1016/0167-2738(92)90089-8.

[8] R. A. D. Souza, J. Fleig, R. Merkle, and J. Maier. "$SrTiO_3$: A Model Electroceramic". In: *Zeitschrift für Metallkunde* 94.3 (2003), pp. 218–225. DOI: 10.3139/146.030218.

[9] R. A. D. Souza, V. Metlenko, D. Park, and T. E. Weirich. "Behavior of oxygen vacancies in single-crystal $SrTiO_3$: Equilibrium distribution and diffusion kinetics". In: *Physical Review B* 85.17 (2012), p. 174109. DOI: 10.1103/physrevb.85.174109.

[10] R. Merkle, R. A. D. Souza, and J. Maier. "Optically Tuning the Rate of Stoichiometry Changes: Surface-Controlled Oxygen Incorporation into Oxides under UV Irradiation". In: *Angewandte Chemie International Edition* 40.11 (2001), pp. 2126–2129. DOI: 10.1002/1521-3773(20010601)40:11<2126::aid-anie2126>3.0.co;2-k.

[11] F. V. E. Hensling, D. J. Keeble, J. Zhu, S. Brose, C. Xu, F. Gunkel, S. Danylyuk, S. S. Nonnenmann, W. Egger, and R. Dittmann. "UV radiation enhanced oxygen vacancy formation caused by the PLD plasma plume". In: *Scientific Reports* 8.1 (2018), p. 8846. DOI: 10.1038/s41598-018-27207-5.

[12] F. Horikiri, T. Ichikawa, L. Q. Han, A. Kaimai, K. Yashiro, H. Matsumoto, T. Kawada, and J. Mizusaki. "Nb-Doped $SrTiO_3$-Based High-Temperature Schottky Solar Cells". In: *Japanese Journal of Applied Physics* 44.11 (2005), pp. 8023–8026. DOI: 10.1143/jjap.44.8023.

[13] P. R. Shearing, D. J. L. Brett, and N. P. Brandon. "Towards intelligent engineering of SOFC electrodes: a review of advanced microstructural characterisation techniques". In: *International Materials Reviews* 55.6 (2010), pp. 347–363. DOI: 10.1179/095066010x12777205875679.

[14] M. J. Montenegro and T. Lippert. "Films for Electrochemical Applications". In: *Pulsed Laser Deposition of Thin Films*. John Wiley & Sons, Inc., 2006, pp. 563–584. DOI: 10.1002/9780470052129.ch22.

[15] C. Xu, S. Wicklein, A. Sambri, S. Amoruso, M. Moors, and R. Dittmann. "Impact of the interplay between nonstoichiometry and kinetic energy of the plume species on the growth mode of $SrTiO_3$ thin films". In: *Journal of Physics D: Applied Physics* 47.3 (2013), p. 034009. DOI: 10.1088/0022-3727/47/3/034009.

[16] N. H. Chan. "Nonstoichiometry in $SrTiO_3$". In: *Journal of The Electrochemical Society* 128.8 (1981), p. 1762. DOI: 10.1149/1.2127727.

[17] N. G. Eror and U. Balachandran. "Electrical conductivity in strontium titanate with nonideal cationic ratio". In: *Journal of Solid State Chemistry* 42.3 (1982), pp. 227–241. DOI: 10.1016/0022-4596(82)90002-0.

[18] Q. Ma, F. Tietz, and D. Stöver. "Nonstoichiometric Y-substituted $SrTiO_3$ materials as anodes for solid oxide fuel cells". In: *Solid State Ion.* 192.1 (2011), pp. 535–539. DOI: 10.1016/j.ssi.2010.03.027.

[19] Z. Wang, M. Cao, Z. Yao, G. Li, Z. Song, W. Hu, H. Hao, H. Liu, and Z. Yu. "Effects of Sr/Ti ratio on the microstructure and energy storage properties of nonstoichiometric $SrTiO_3$ ceramics". In: *Ceramics International* 40.1 (2014), pp. 929–933. DOI: 10.1016/j.ceramint.2013.06.088.

[20] X. Wang, Q. Hu, G. Zang, C. Zhang, and L. Li. "Structural and electrical characteristics of Sr/Ti nonstoichiometric $SrTiO_3$ ceramics". In: *Solid State Communications* 266 (2017), pp. 1–5. DOI: 10.1016/j.ssc.2017.08.009.

[21] L. Amaral, A. Tkach, P. M. Vilarinho, and A. M. R. Senos. "New Insights into the Effect of Nonstoichiometry on the Electric Response of Strontium Titanate Ceramics". In: *The Journal of Physical Chemistry C* 123.1 (2018), pp. 710–718. DOI: 10.1021/acs.jpcc.8b10438.

[22] M. Bäurer, H. Kungl, and M. J. Hoffmann. "Influence of Sr/Ti Stoichiometry on the Densification Behavior of Strontium Titanate". In: *Journal of the American Ceramic Society* 92.3 (2009), pp. 601–606. DOI: 10.1111/j.1551-2916.2008.02920.x.

[23] S. Witek, D. M. Smyth, and H. Piclup. "Variability of the Sr/Ti Ratio in $SrTiO_3$". In: *Journal of the American Ceramic Society* 67.5 (1984), pp. 372–375. DOI: 10.1111/j.1151-2916.1984.tb19540.x.

[24] R. Merkle and J. Maier. "How Is Oxygen Incorporated into Oxides? A Comprehensive Kinetic Study of a Simple Solid-State Reaction with $SrTiO_3$ as a Model Material". In: *Angewandte Chemie International Edition* 47.21 (2008), pp. 3874–3894. DOI: 10.1002/anie.200700987.

[25] A. Viernstein, M. Kubicek, M. Morgenbesser, G. Walch, G. C. Brunauer, and J. Fleig. "High-Temperature Photochromism of Fe-Doped $SrTiO_3$ Caused by UV-Induced Bulk Stoichiometry Changes". In: *Advanced Functional Materials* 29.23 (2019), p. 1900196. DOI: 10.1002/adfm.201900196.

[26] J.-J. Wang, H.-B. Huang, T. J. M. Bayer, A. Moballegh, Y. Cao, A. Klein, E. C. Dickey, D. L. Irving, C. A. Randall, and L.-Q. Chen. "Defect chemistry and resistance degradation in Fe-doped $SrTiO_3$ single crystal". In: *Acta Materialia* 108 (2016), pp. 229–240. DOI: 10.1016/j.actamat.2016.02.022.

[27] S. Taibl, G. Fafilek, and J. Fleig. "Impedance spectra of Fe-doped $SrTiO_3$ thin films upon bias voltage: inductive loops as a trace of ion motion". In: *Nanoscale* 8.29 (2016), pp. 13954–13966. DOI: 10.1039/c6nr00814c.

[28] M. J. Akhtar, Z.-U.-N. Akhtar, R. A. Jackson, and C. R. A. Catlow. "Computer Simulation Studies of Strontium Titanate". In: *Journal of the American Ceramic Society* 78.2 (1995), pp. 421–428. DOI: 10.1111/j.1151-2916.1995.tb08818.x.

[29] R. A. Maier, A. C. Johnston-Peck, and M. P. Donohue. "(Magic Dopant) Amphoteric Behavior of a Redox-Active Transition Metal Ion in a Perovskite Lattice: New Insights on the Lattice Site Occupation of Manganese in $SrTiO_3$". In: *Advanced Functional Materials* 26.45 (2016), pp. 8325–8333. DOI: 10.1002/adfm.201602156.

[30] V. Pecharsky and P. Zavalij. *Fundamentals of Powder Diffraction and Structural Characterization of Materials*. Springer US, 2009. DOI: 10.1007/978-0-387-09579-0.

[31] W. Borchardt-Ott. "Der Kristallzustand". In: *Kristallographie*. Springer Berlin Heidelberg, 2009, pp. 3–8. DOI: 10.1007/978-3-540-78271-1_2.

[32] R. J. D. Tilley. "Point Defects". In: *Defects in Solids*. John Wiley & Sons, Inc., 2008, pp. 1–44. DOI: 10.1002/9780470380758.ch1.

[33] R. J. D. Tilley. "Extended Defects". In: *Defects in Solids*. John Wiley & Sons, Inc., 2008, pp. 83–133. DOI: 10.1002/9780470380758.ch3.

[34] J. J. Boland. "The importance of structure and bonding in semiconductor surface chemistry: hydrogen on the Si(111)-7 x 7 surface". In: *Surface Science* 244.1-2 (1991), pp. 1–14. DOI: 10.1016/0039-6028(91)90164-n.

[35] J. Fleig. "Microelectrodes in Solid State Ionics". In: *Advances in Electrochemical Science and Engineering, Volume 8*. Wiley-VCH Verlag GmbH & Co. KGaA, 2002, pp. 1–87. DOI: 10.1002/3527600787.ch1.

[36] J. Maier. "Equilibrium Thermodynamics of the Real Solid". In: *Physical Chemistry of Ionic Materials*. John Wiley & Sons, Ltd, 2005, pp. 108–267. DOI: 10.1002/0470020229.ch5.

[37] J. Maier. "Introduction". In: *Physical Chemistry of Ionic Materials*. John Wiley & Sons, Ltd, 2005, pp. 11–22. DOI: 10.1002/0470020229.ch1.

[38] R. J. D. Tilley. "Nonstoichiometry and Intrinsic Electronic Conductivity". In: *Defects in Solids*. John Wiley & Sons, Inc., 2008, pp. 297–350. DOI: 10.1002/9780470380758.ch7.

[39] J. Maier. "Kinetics and Irreversible Thermodynamics". In: *Physical Chemistry of Ionic Materials*. John Wiley & Sons, Ltd, 2005, pp. 268–398. DOI: 10.1002/0470020229.ch6.

[40] J. Sunarso, S. Baumann, J. M. Serra, W. A. Meulenberg, S. Liu, Y. S. Lin, and J. C. D. da Costa. "Mixed ionic-electronic conducting (MIEC) ceramic-based membranes for oxygen separation". In: *Journal of Membrane Science* 320.1-2 (2008), pp. 13–41. DOI: 10.1016/j.memsci.2008.03.074.

[41] R. J. D. Tilley. "Intrinsic and Extrinsic Defects in Insulators: Ionic Conductivity". In: *Defects in Solids*. John Wiley & Sons, Inc., 2008, pp. 251–295. DOI: 10.1002/9780470380758.ch6.

[42] S. Lany. "Semiconducting transition metal oxides". In: *Journal of Physics: Condensed Matter* 27.28 (2015), p. 283203. DOI: 10.1088/0953-8984/27/28/283203.

[43] S. J. F. Byrnes. "Basic theory and phenomenology of polarons". In: *Citeseer* (2008).

[44] M. Kubicek, S. Taibl, E. Navickas, H. Hutter, G. Fafilek, and J. Fleig. "Resistive states in strontium titanate thin films: Bias effects and mechanisms at high and low temperature". In: *Journal of Electroceramics* 39.1-4 (2017), pp. 197–209. DOI: 10.1007/s10832-017-0081-2.

[45] H. Trabelsi, M. Bejar, E. Dhahri, M. Sajieddine, K. Khirouni, P. R. Prezas, B. M. G. Melo, M. A. Valente, and M. P. F. Graca. "Effect of oxygen vacancies on $SrTiO_3$ electrical properties". In: *Journal of Alloys and Compounds* 723 (2017), pp. 894–903. DOI: 10.1016/j.jallcom.2017.06.313.

[46] J. Jurado. "Impedance spectroscopy of $Sr_{0.97}Ti_{1-x}Fe_xO_3$ materials with moderate Fe-contents". In: *Solid State Ion.* 143.2 (2001), pp. 251–257. DOI: 10.1016/s0167-2738(01)00823-2.

[47] M. Vollmann, R. Hagenbeck, and R. Waser. "Grain-Boundary Defect Chemistry of Acceptor-Doped Titanates: Inversion Layer and Low-Field Conduction". In: *Journal of the American Ceramic Society* 80.9 (1997), pp. 2301–2314. DOI: 10.1111/j.1151-2916.1997.tb03121.x.

[48] J. P. Buban, H. Iddir, and S. Ögüt. "Structural and electronic properties of oxygen vacancies in cubic and antiferrodistortive phases of $SrTiO_3$". In: *Physical Review B* 69.18 (2004), p. 180102. DOI: 10.1103/physrevb.69.180102.

[49] E. McCalla, J. Walter, and C. Leighton. "A Unified View of the Substitution-Dependent Antiferrodistortive Phase Transition in $SrTiO_3$". In: *Chemistry of Materials* 28.21 (2016), pp. 7973–7981. DOI: 10.1021/acs.chemmater.6b03667.

[50] S. A. Hayward and E. K. H. Salje. "Cubic-tetragonal phase transition in $SrTiO_3$ revisited: Landau theory and transition mechanism". In: *Phase Transitions* 68.3 (1999), pp. 501–522. DOI: 10.1080/01411599908224530.

[51] U. Aschauer and N. A. Spaldin. "Competition and cooperation between antiferrodistortive and ferroelectric instabilities in the model perovskite $SrTiO_3$". In: *Journal of Physics: Condensed Matter* 26.12 (2014), p. 122203. DOI: 10.1088/0953-8984/26/12/122203.

[52] O. E. Kvyatkovskii. "Quantum effects in incipient and low-temperature ferroelectrics (a review)". In: *Physics of the Solid State* 43.8 (2001), pp. 1401–1419. DOI: 10.1134/1.1395075.

[53] P. A. Fleury, J. F. Scott, and J. M. Worlock. "Soft Phonon Modes and the 110 K Phase Transition in $SrTiO_3$". In: *Physical Review Letters* 21.1 (1968), pp. 16–19. DOI: 10.1103/physrevlett.21.16.

[54] K. A. Müller and H. Burkard. "$SrTiO_3$: An intrinsic quantum paraelectric below 4 K". In: *Physical Review B* 19.7 (1979), pp. 3593–3602. DOI: 10.1103/physrevb.19.3593.

[55] O.-M. Nes, K. A. Müller, T. Suzuki, and F. Fossheim. "Elastic Anomalies in the Quantum Paraelectric Regime of $SrTiO_3$". In: *Europhysics Letters (EPL)* 19.5 (1992), pp. 397–402. DOI: 10.1209/0295-5075/19/5/009.

[56] H. Uwe and T. Sakudo. "Stress-induced ferroelectricity and soft phonon modes in $SrTiO_3$". In: *Physical Review B* 13.1 (1976), pp. 271–286. DOI: 10.1103/physrevb.13.271.

[57] M. Itoh, R. Wang, Y. Inaguma, T. Yamaguchi, Y.-J. Shan, and T. Nakamura. "Ferroelectricity Induced by Oxygen Isotope Exchange in Strontium Titanate Perovskite". In: *Physical Review Letters* 82.17 (1999), pp. 3540–3543. DOI: 10.1103/physrevlett.82.3540.

[58] J. G. Bednorz and K. A. Müller. "$Sr_{1-x}Ca_xTiO_3$: An XY Quantum Ferroelectric with Transition to Randomness". In: *Physical Review Letters* 52.25 (1984), pp. 2289–2292. DOI: 10.1103/physrevlett.52.2289.

[59] F. M. Pontes, E. J. H. Lee, E. R. Leite, E. Longo, and J. A. Varela. "High dielectric constant of $SrTiO_3$ thin films prepared by chemical process". In: *Journal of Materials Science* 35.19 (2000), pp. 4783–4787. DOI: 10.1023/a:1004816611050.

[60] R. C. Neville, B. Hoeneisen, and C. A. Mead. "Permittivity of Strontium Titanate". In: *Journal of Applied Physics* 43.5 (1972), pp. 2124–2131. DOI: 10.1063/1.1661463.

[61] H. E. Weaver. "Dielectric properties of single crystals of $SrTiO_3$ at low temperatures". In: *Journal of Physics and Chemistry of Solids* 11.3-4 (1959), pp. 274–277. DOI: 10.1016/0022-3697(59)90226-4.

[62] D. E. Grupp. "Giant Piezoelectric Effect in Strontium Titanate at Cryogenic Temperatures". In: *Science* 276.5311 (1997), pp. 392–394. DOI: 10.1126/science.276.5311.392.

[63] W. D. Rice, P. Ambwani, J. D. Thompson, C. Leighton, and S. A. Crooker. "Revealing optically induced magnetization in $SrTiO_3$ using optically coupled SQUID magnetometry and magnetic circular dichroism". In: *Journal of Vacuum Science & Technology B, Nanotechnology and Microelectronics: Materials, Processing, Measurement, and Phenomena* 32.4 (2014), p. 102. DOI: 10.1116/1.4871691.

[64] C. S. Koonce, M. L. Cohen, J. F. Schooley, W. R. Hosler, and E. R. Pfeiffer. "Superconducting Transition Temperatures of Semiconducting $SrTiO_3$". In: *Physical Review* 163.2 (1967), pp. 380–390. DOI: 10.1103/physrev.163.380.

[65] A. Janotti, J. B. Varley, M. Choi, and C. G. V. de Walle. "Vacancies and small polarons in $SrTiO_3$". In: *Physical Review B* 90.8 (2014), p. 085202. DOI: 10.1103/physrevb.90.085202.

[66] Y. Yamada, H. Yasuda, T. Tayagaki, and Y. Kanemitsu. "Temperature Dependence of Photoluminescence Spectra of Nondoped and Electron-Doped $SrTiO_3$: Crossover from Auger Recombination to Single-Carrier Trapping". In: *Physical Review Letters* 102.24 (2009), p. 247401. DOI: 10.1103/physrevlett.102.247401.

[67] R. Moos and K. H. Hardtl. "Defect Chemistry of Donor-Doped and Undoped Strontium Titanate Ceramics between 1000 and 1400 °C". In: *Journal of the American Ceramic Society* 80.10 (1997), pp. 2549–2562. DOI: 10.1111/j.1151-2916.1997.tb03157.x.

[68] K. H. Lee, S. W. Kim, H. Ohta, and K. Koumoto. "Ruddlesden-Popper phases as thermoelectric oxides: Nb-doped $SrO(SrTiO_3)_n$ (n=1,2)". In: *Journal of Applied Physics* 100.6 (2006), p. 063717. DOI: 10.1063/1.2349559.

[69] U. Balachandran and N. G. Eror. "Electrical Conductivity in Lanthanum-Doped Strontium Titanate". In: *Journal of The Electrochemical Society* 129.5 (1982), p. 1021. DOI: 10.1149/1.2124008.

[70] U. Balachandran and N. G. Eror. "On the defect structure of strontium titanate with excess SrO". In: *Journal of Materials Science* 17.7 (1982), pp. 2133–2140. DOI: 10.1007/bf00540432.

[71] S. N. Ruddlesden and P. Popper. "The compound $Sr_3Ti_2O_7$ and its structure". In: *Acta Crystallographica* 11.1 (1958), pp. 54–55. DOI: 10.1107/s0365110x58000128.

[72] B. Liu, V. R. Cooper, H. Xu, H. Xiao, Y. Zhang, and W. J. Weber. "Composition dependent intrinsic defect structures in $SrTiO_3$". In: *Physical Chemistry Chemical Physics* 16.29 (2014), pp. 15590–15596. DOI: 10.1039/c4cp01510j.

[73] D. J. Keeble, S. Wicklein, L. Jin, C. L. Jia, W. Egger, and R. Dittmann. "Nonstoichiometry accommodation in $SrTiO_3$ thin films studied by positron annihilation and electron microscopy". In: *Physical Review B* 87.19 (2013), p. 195409. DOI: 10.1103/physrevb.87.195409.

[74] K. Morito, T. Suzuki, and M. Fujimoto. "Microstructure and Electrical Properties of Nonstoichiometric Strontium Titanate Thin Films Grown on Platinum Electrodes". In: *Japanese Journal of Applied Physics* 40.Part 1, No. 3A (2001), pp. 1310–1314. DOI: 10.1143/jjap.40.1310.

[75] E. Breckenfeld, R. Wilson, J. Karthik, A. R. Damodaran, D. G. Cahill, and L. W. Martin. "Effect of Growth Induced (Non)Stoichiometry on the Structure, Dielectric Response, and Thermal Conductivity of $SrTiO_3$ Thin Films". In: *Chemistry of Materials* 24.2 (2012), pp. 331–337. DOI: 10.1021/cm203042q.

[76] Y. Y. Guo, H. M. Liu, D. P. Yu, and J.-M. Liu. "Ferroelectricity and superparamagnetism in Sr/Ti nonstoichiometric $SrTiO_3$". In: *Physical Review B* 85.10 (2012), p. 104108. DOI: 10.1103/physrevb.85.104108.

[77] R. Moos, W. Menesklou, and K. H. Haerdtl. "Hall mobility of undoped n-type conducting strontium titanate single crystals between 19 K and 1373 K". In: *Applied Physics A Materials Science & Processing* 61.4 (1995), pp. 389–395. DOI: 10.1007/bf01540113.

[78] K. Sasaki and J. Maier. "Low-temperature defect chemistry of oxides. I. General aspects and numerical calculations". In: *Journal of Applied Physics* 86.10 (1999), pp. 5422–5433. DOI: 10.1063/1.371541.

[79] K. Sasaki and J. Maier. "Low-temperature defect chemistry of oxides. II. Analytical relations". In: *Journal of Applied Physics* 86.10 (1999), pp. 5434–5443. DOI: 10.1063/1.371542.

[80] N. Shanthi and D. D. Sarma. "Electronic structure of electron doped $SrTiO_3$: $SrTiO_3$ and $SrLaTiO_3$". In: *Physical Review B* 57.4 (1998), pp. 2153–2158. DOI: 10.1103/physrevb.57.2153.

[81] D. D. Cuong, B. Lee, K. M. Choi, H.-S. Ahn, S. Han, and J. Lee. "Oxygen Vacancy Clustering and Electron Localization in Oxygen-Deficient $SrTiO_3$: LDA U Study". In: *Physical Review Letters* 98.11 (2007), p. 115503. DOI: 10.1103/physrevlett.98.115503.

[82] F. Cordero. "Hopping and clustering of oxygen vacancies in $SrTiO_3$". In: *Materials Science and Engineering: A* 521-522 (2009), pp. 77–79. DOI: 10.1016/j.msea.2008.07.079.

[83] U. Balachandran and N. G. Eror. "Electrical conductivity in strontium titanate". In: *Journal of Solid State Chemistry* 39.3 (1981), pp. 351–359. DOI: 10.1016/0022-4596(81)90270-x.

[84] R. A. Maier and C. A. Randall. "Low-Temperature Ionic Conductivity of an Acceptor-Doped Perovskite: I. Impedance of Single-Crystal $SrTiO_3$". In: *Journal of the American Ceramic Society* 99.10 (2016), pp. 3350–3359. DOI: 10.1111/jace.14348.

[85] P. Blennow, A. Hagen, K. Hansen, L. Wallenberg, and M. Morgensen. "Defect and electrical transport properties of Nb-doped $SrTiO_3$". In: *Solid State Ion.* 179.35-36 (2008), pp. 2047–2058. DOI: 10.1016/j.ssi.2008.06.023.

[86] R. Moos and K. H. Härdtl. "Electronic transport properties of $Sr_{1-x}La_xTiO_3$ ceramics". In: *Journal of Applied Physics* 80.1 (1996), pp. 393–400. DOI: 10.1063/1.362796.

[87] T. Bieger, J. Maier, and R. Waser. "Optical investigation of oxygen incorporation in $SrTiO_3$". In: *Solid State Ion.* 53-56.1 (1992), pp. 578–582. DOI: 10.1016/0167-2738(92)90432-o.

[88] J. Bouwma, K. J. de Vries, and A. J. Burggraaf. "Non-stoichiometry, defect structure, and dielectric relaxation in lanthana-substituted $SrTiO_3$". In: *Physica Status Solidi (a)* 35.1 (1976), pp. 281–290. DOI: 10.1002/pssa.2210350130.

[89] R. Merkle and J. Maier. "Defect association in acceptor-doped $SrTiO_3$: case study for Fe_{Ti}-V_O and Mn_{Ti}-V_O". In: *Physical Chemistry Chemical Physics* 5.11 (2003), pp. 2297–2303. DOI: 10.1039/b300205p.

[90] J. N. Baker, P. C. Bowes, D. M. Long, A. Moballegh, J. S. Harris, E. C. Dickey, and D. L. Irving. "Defect mechanisms of coloration in Fe-doped $SrTiO_3$ from first principles". In: *Applied Physics Letters* 110.12 (2017), p. 122903. DOI: 10.1063/1.4978861.

[91] C. J. Yu, H. U. Anderson, and D. M. Sparlin. "High-temperature defect structure of Nb-doped $LaCrO_3$". In: *Journal of Solid State Chemistry* 78.2 (1989), pp. 242–249. DOI: 10.1016/0022-4596(89)90104-7.

[92] T. Wei, L. Jia, J.-L. Luo, B. Chi, J. Pu, and J. Li. "CO_2 dry reforming of CH_4 with Sr and Ni co-doped $LaCrO_3$ perovskite catalysts". In: *Applied Surface Science* 506 (2020), p. 144699. DOI: 10.1016/j.apsusc.2019.144699.

[93] D. B. Meadowcroft. "Some properties of strontium-doped lanthanum chromite". In: *Journal of Physics D: Applied Physics* 2.9 (1969), pp. 1225–1233. DOI: 10.1088/0022-3727/2/9/304.

[94] J. W. Fergus. "Lanthanum chromite-based materials for solid oxide fuel cell interconnects". In: *Solid State Ion.* 171.1-2 (2004), pp. 1–15. DOI: 10.1016/j.ssi.2004.04.010.

[95] M. E. Orazem and B. Tribollet. "Electrical Circuits". In: *Electrochemical Impedance Spectroscopy*. John Wiley & Sons, Inc., 2017, pp. 75–88. DOI: 10.1002/9781119363682.ch4.

[96] M. E. Orazem and B. Tribollet. "Constant-Phase Elements". In: *Electrochemical Impedance Spectroscopy*. John Wiley & Sons, Inc., 2017, pp. 395–419. DOI: 10.1002/9781119363682.ch14.

[97] M. E. Orazem and B. Tribollet. "Methods for Representing Impedance". In: *Electrochemical Impedance Spectroscopy*. John Wiley & Sons, Inc., 2017, pp. 465–492. DOI: 10.1002/9781119363682.ch17.

[98] J. Fleig and J. Maier. "The impedance of ceramics with highly resistive grain boundaries: validity and limits of the brick layer model". In: *Journal of the European Ceramic Society* 19.6-7 (1999), pp. 693–696. DOI: 10.1016/s0955-2219(98)00298-2.

[99] J. C. C. Abrantes, J. A. Labrincha, and J. R. Frade. "Applicability of the brick layer model to describe the grain boundary properties of strontium titanate ceramics". In: *Journal of the European Ceramic Society* 20.10 (2000), pp. 1603–1609. DOI: 10.1016/s0955-2219(00)00022-4.

[100] D. M. Mattox. "Introduction". In: *Handbook of Physical Vapor Deposition (PVD) Processing*. Elsevier, 2010, pp. 1–24. DOI: 10.1016/b978-0-8155-2037-5.00001-0.

[101] D. P. Norton. "Pulsed Laser Deposition of Complex Materials: Progress Toward Applications". In: *Pulsed Laser Deposition of Thin Films*. John Wiley & Sons, Inc., 2006, pp. 1–31. DOI: 10.1002/9780470052129.ch1.

[102] S. Gerhold, M. Riva, B. Yildiz, M. Schmid, and U. Diebold. "Adjusting island density and morphology of the $SrTiO_3$(110)-(4 x 1) surface: Pulsed laser deposition combined with scanning tunneling microscopy". In: *Surface Science* 651 (2016), pp. 76–83. DOI: 10.1016/j.susc.2016.03.010.

[103] R. Wurm, O. Dernovsek, and P. Greil. "Sol-Gel derived $SrTiO_3$ and $SrZrO_3$ coatings on SiC and C-fibers". In: *Journal of Materials Science* 34.16 (1999), pp. 4031–4037. DOI: 10.1023/a:1004668016453.

[104] Y. Gao, Z. Lu, T. L. You, J. Wang, L. Xie, J. He, and F. Ciucci. "Energetics of Nanoparticle Exsolution from Perovskite Oxides". In: *The Journal of Physical Chemistry Letters* 9.13 (2018), pp. 3772–3778. DOI: 10.1021/acs.jpclett.8b01380.

[105] S. Rodewald, J. Fleig, and J. Maier. "Microcontact Impedance Spectroscopy at Single Grain Boundaries in Fe-Doped $SrTiO_3$ Polycrystals". In: *Journal of the American Ceramic Society* 84.3 (2001), pp. 521–530. DOI: 10.1111/j.1151-2916.2001.tb00693.x.

[106] I. Denk, W. Münch, and J. Maier. "Partial Conductivities in $SrTiO_3$: Bulk Polarization Experiments, Oxygen Concentration Cell Measurements, and Defect-Chemical Modeling". In: *Journal of the American Ceramic Society* 78.12 (1995), pp. 3265–3272. DOI: 10.1111/j.1151-2916.1995.tb07963.x.

[107] M. Kubicek, G. M. Rupp, S. Huber, A. Penn, A. K. Opitz, J. Bernardi, M. Stöger-Pollach, H. Hutter, and J. Fleig. "Cation diffusion in $La_{0.6}Sr_{0.4}CoO_3$ below 800 °C and its relevance for Sr segregation". In: *Physical Chemistry Chemical Physics* 16.6 (2014), p. 2715. DOI: 10.1039/c3cp51906f.

[108] I. Denk, F. Noll, and J. Maier. "In situ Profiles of Oxygen Diffusion in $SrTiO_3$: Bulk Behavior and Boundary Effects". In: *Journal of the American Ceramic Society* 80.2 (1997), pp. 279–285. DOI: 10.1111/j.1151-2916.1997.tb02827.x.